THz Plasma Waves in Field-Effect-Transistors: A Monte Carlo Study

Dissertation zur Erlangung des akademischen Grades

Doktor der Ingenieurwissenschaften (Dr.-Ing.)

Vorgelegt im Fachbereich Elektrotechnik/Informatik
der Universität Kassel

Von Dipl.-Ing. (FH) Steffen Schumann

Prüfungskommission: Prof. Dr. rer. nat. Hartmut Hillmer (1. Gutachter)
Prof. Dr.-Ing. Ubbo Ricklefs (2. Gutachter)
Prof. Dr. rer. nat. Bernd Witzigmann
Prof. Dr. rer. nat. Martin Koch

Tag der Disputation: 5.11.2015

Marburg, August 2015

Erklärung

Hiermit versichere ich, dass ich die vorliegende Dissertation selbstständig, ohne unerlaubte Hilfe Dritter angefertigt und andere als die in der Dissertation angegebenen Hilfsmittel nicht benutzt habe. Alle Stellen, die wörtlich oder sinngemäß aus veröffentlichten oder unveröffentlichten Schriften entnommen sind, habe ich als solche kenntlich gemacht. Dritte waren an der inhaltlich-materiellen Erstellung der Dissertation nicht beteiligt; insbesondere habe ich hierfür nicht die Hilfe eines Promotionsberaters in Anspruch genommen. Kein Teil dieser Arbeit ist in einem anderen Promotions- oder Habilitationsverfahren verwendet worden.

Steffen Schumann

Summary

Sensing with electromagnetic waves having frequencies in the Terahertz-range is a very attractive investigative method with applications in fundamental research and industrial settings. Up to now, a lot of sources and detectors are available. However, most of these systems are bulky and have to be used in controllable environments such as laboratories. In 1993 Dyakonov and Shur suggested that plasma waves developing in field-effect-transistors can be used to emit and detect THz-radiation. Later on, it was shown that these plasma waves lead to rectification and allows for building efficient detectors. In contrast to the prediction that these plasma waves lead to new promising solid-state sources, only a few weak sources are known up to now. This work studies THz plasma waves in semiconductor devices using the Monte Carlo method in order to resolve this issue. A fast Monte Carlo solver was developed implementing a nonparabolic band-structure representation of the used semiconductors. By investigating simplified field-effect-transistors it was found that the plasma frequency follows under equilibrium conditions the analytical predictions. However, no current oscillations were found at room temperature or with a current flowing in the channel. For more complex structures, consisting of ungated and gated regions, it was found that the plasma frequency does not follow the value predicted by the dispersion relation of the gated nor the ungated device.

Keywords: Monte Carlo method, plasma oscillations, field-effect-transistors, Terahertz

Zusammenfassung

Der messtechnische Einsatz elektromagnetischer Strahlung im Terahertzfrequenzbereich erfreut sich, sowohl in der Grundlagenforschung als auch in der industriellen Anwendungen, in jüngerer Zeit immer größerer Nutzung. Heutzutage existiert eine Vielzahl von Quellen und Detektoren für diesen erst in den letzten zwei Jahrzehnten erschlossenen Spektralbereich. Trotz des rasanten technologischen Fortschritts sind die Meisten dieser Systeme jedoch auf kontrollierbare Laborumgebungen beschränkt. Dyakonov und Shur schlugen 1993 einen neuartigen Mechanismus vor, der auf der Instabilität von Plasmawellen in einem Feldeffekttransistorkanal beruht, welcher sich sowohl zur Detektion als auch Emission von THz-Strahlung eignet. Auf dieser Grundlage wurden sehr erfolgreich gleichrichtende, bei Raumtemperatur arbeitende, Detektoren entwickelt. Gegenüber der durch die Detektorentwicklung geschriebenen Erfolgsgeschichte stehen nur wenige auf dieser Grundlage arbeitende Emitter. Um diesen Missstand zu ergründen, wurde in dieser Arbeit ein Simulationsprogramm, basierend auf der Monte Carlo Methode, entwickelt. Durch numerische Simulation von vereinfachten Feldeffekttransistoren soll ein tieferes Verständnis über THz Plasmawellen erlangt werden. Aufgrund des hohen Rechenaufwandes wurde auf eine stark parallelisierte Implementierung und ein einfaches nichtparabolisches Halbleiterbandstrukturmodell gesetzt. Für einfache Strukturen ohne stattfindende Anregung folgt die Plasmafrequenz den analytischen Vorhersagen. Allerdings konnte bei zunehmender Temperatur oder fließendem Drainstrom eine starke Dämpfung der Plasmaoszillationen beobachtet werden. Für komplexere Strukturen, welche aus Bereichen mit und ohne Gate bestehen, kann die beobachtete Plasmafrequenz nicht aus der einfachen analytischen Beschreibung abgeleitet werden.

Stichwörter: Monte Carlo Methode, Plasmaoszillationen, Feldeffekttransistoren, Terahertz

Contents

1. Introduction & Motivation

The Terahertz (THz) frequency range is often stated as the region of the electromagnetic spectrum between 300 GHz and 10 THz. It was referred to as the THz gap, since it could not be accessed by using conventional electronic (diodes, mixers and amplifiers) nor optical sources (LEDs, lasers, photodiodes). Today a lot of different technologies accessing this frequency range are available and the gap can be considered closed. Especially detectors are well developed and real-time cameras are commercially available. However, the first commercially available system making use of THz radiation was first-time available in the year 2000 [1].

Promising advantages of the THz frequency range opened the window to interesting new applications. When compared to microwaves, the achieved resolution in imaging applications is much better, due to the smaller wavelength. Additionally, the radiation is still able to penetrate most materials which are opaque in the optical range. Mm-waves impose no risk to its users since it is non-ionizing. In the scientific field THz waves produced by ultrashort pulses have helped researchers to investigate carrier dynamics in semiconductors on an fast timescale [2]. On polymers, a morphological study allows for distinguishing structural changes [3]. In molecules the low-energetic THz waves excite intramolecular, vibrational and rotational transitions, which make it ideally suited as a spectroscopic tool [4–7]. However, the use of mm-waves is not only limited to scientific research and has widely deployed in various real-world scenarios: in medical studies THz waves have been used to perform in vivo burn diagnosis [8]. Human skin affected by cancer and demineralized teeth reflect THz waves different compared to healthy cells/teeth [9]. Many liquids or gaseous substances have unique fingerprints formed by absorption peaks in the lower far-infrared region. These fingerprints can be used as a detection mechanism in security motivated research fields [10, 11]. Even cameras have been developed, revealing concealed perils [12]. THz waves are highly absorbed by water, which makes it an ideally sensor for water content detection in plants and allows for an effective investigation of drought stress [13]. Additionally, proteins and polysaccharides show absorption bands in this frequency range, allowing a proper distinction of ingredients [14]. The transparency of polymers for THz waves has been extensively studied in non-destructive testing scenarios where welding joints, inclusions and material composition has been evaluated [15].

Up to now a wide range of sources and detectors are available: emerging tech-

nologies from both sides of the electromagnetic spectrum have closed the THz gap. Sources relying on optical techniques mostly make use of femtosecond lasers or amplifier systems. A quite prominent approach is the excitation of photoconductive antennas acting as ultrafast switches and detectors. Commonly referred to as THz time-domain spectroscopy (THz-TDS) [16]. Similar approaches using ultrafast lasers with pulses in the lower femtosecond-range use the photo-Dember effect where the excited electrons and holes diffuse in the material and produce an ultrashort current [17]. Optical rectification in nonlinear crystals like lithium-niobate driven by amplifier systems have proven to emit strong pulses reaching several $100\,\mathrm{kV\,cm^{-1}}$ [18]. Pulsed THz generation and detection from amplifier-generated air plasma has significantly improved the available bandwidth of modern spectrometers far beyond 10 THz [19]. Additionally, continuous-wave (cw) sources are mostly based on difference frequency generation (DFG) in a nonlinear crystal [20] or photoconductive antennas [21], reaching more than 2 THz. Since most of these systems are rather bulky and sensitive to environmental influences due to the involved laser systems, they are mostly used in laboratories.

In contrast to optical sources, electronic sources rely often on frequency upconversion: frequency multiplier chains are available at cryogenic temperatures up to a frequency of 2.5 THz delivering an output power of 1 µW [22, 23]. As direct sources diodes make use of a negative-differential resistance, realized in GUNN-, IMPATT- or RT-diodes [24–26]. These two-terminal devices cover mostly the lower THz frequency range up to several hundred GHz. Today, MMIC-technology deploying HEMTs reach record-breaking maximum oscillation frequencies beyond 1 THz. A comprehensive review is given by Samoska [27].

With the pioneering work of Tsui [28] in the year 1980, it was demonstrated that emission of far-infrared radiation can be observed by exciting plasma waves. These longitudinal waves can be coupled via a grating to an electromagnetic wave and measured. In the 1990s, Dyakonov [29] suggested in a theoretical study that plasma waves can exist in a field-effect-transistor with a submicrometer-size gate length. Based on his predictions that an incoming THz wave will be rectified due to the plasma wave behaviour, effective detectors have been developed. However, up to now no efficient solid-state sources are available relying on plasma waves. The goal of this thesis is to provide a comprehensive view on device physics. Furthermore, the question should be answered why there are up to now no sources available and what can be done to overcome these circumstances.

This work studies plasma oscillations in semiconductor devices using the Monte Carlo (MC) method for carrier transport, providing a solution of the Boltzmann transport equation (BTE). In contrast to macroscopic models like drift-diffusion or hydrodynamic transport models, the MC method provides an accurate solution down to the deep submicrometer region. Furthermore, the MC method is able to naturally include fluctuation phenomena and is therefore ideally suited as an investigative tool. Its ability to include real scattering processes, rather

than relying on unmotivated or arbitrarily chosen relaxation constants, will be used to give an estimation of the involved current densities and electric fields.

Most readers of this thesis may originally come from the frontiers of THz science, rather than semiconductor device physics. Thus, chapter 2 introduces promising new concepts of generating THz radiation. Afterwards, a historical review of the plasmonic approach based on Field-Effect-Transistor- (FET) emitters and detectors is given. The chapter ends with a brief overview describing the basics of the Monte Carlo method as a transport model describing carrier transport in semiconductor devices.

During this study a device simulator for the MC method solving the Boltzmann transport equation has been implemented using the Fortran programming language. Chapter 3 summarizes the developed solver and the incorporated models. The treatment of particles in a device simulation, the implemented materials and scattering rates are described.

The correct implementation of the developed solver has been validated against experimental and theoretical data, describing the mobility as a function of the electric field and doping level. The results of these simulations are given in chapter 4.

Chapter 5 finally discusses the presence of plasma wave in FET-like structures and presents the dispersion of these waves. The most important properties such as the mode profiles, the influence of the lattice temperature and a current flow in the channel are investigated.

Chapter 6 shows simulations performed for combinated devices consisting of ungated and gated regions demonstrating properties of plasma modes in more complex devices.

Chapter 7 summarizes the key achievements of this work.

2. Background Information

This work deals with the mechanism of generating THz radiation by using plasma waves in field-effect-transistors (FETs). Therefore a short overview of different concepts in generating and detecting THz waves was given in the introductory chapter. The first part of this chapter presents two novel different approaches for THz sources. Followed by the presentation of the plasmonic approach which will be studied later. The chapter ends with an introduction of the Boltzmann transport equation and its numerical solution by the Monte Carlo method for charge carrier transport in semiconductors.

2.1. Sources for THz Radiation

For practical or industrial use most of the already introduced technologies are bulky and expensive. In the last years new concepts from both sides of the electromagnetic spectrum have evolved, namely planar GUNN diodes and THz quantum cascade lasers (THz QCLs). At room temperature they can deliver high output power over a wide frequency range by maintaining a small device size. The following section will discuss the working principle of these devices. Afterwards the plasmonic approach will be introduced.

2.1.1. THz Quantum Cascade Lasers

Quantum cascade lasers (QCLs) are unipolar devices exploiting intersubband transitions to deliver gain. The energetic distance between subbands is in the order of a few tens of meV. Thus the emitted radiation is in the long wavelength region and covers the infrared and THz range. While QCLs in the mid-infrared range (approximately 4-25 µm) work at room temperature and deliver several watt of output power [30], difficulties arise moving to lower THz frequencies [31]:

- Closely spaced subbands make it difficult to inject or remove carriers in or from their destined band.
- The waveguide needs to confine the mode as far as possible to the active region since the surrounding layers lead to high losses by free carrier absorption.
- At lower frequencies high temperature gets more difficult because the lower radiative state will be filled by thermally excited electrons. A higher

phonon population results in an increased optical phonon rate depopulating the upper state.

Empirically it was found that the maximum operating temperature scales with the emission frequency as $T = \hbar\omega/k_B$ [31]. Today, most devices can be effectively reduced to a 3-level system [32], shown in figure 2.1. Resonant tunneling (RT) is injecting carriers to the highest subband 3. The THz photon is emitted by the transition $3 \rightarrow 2$. Finally a population inversion is obtained by the RT process and a fast depopulation of subband 2 via optical phonon scattering. A record

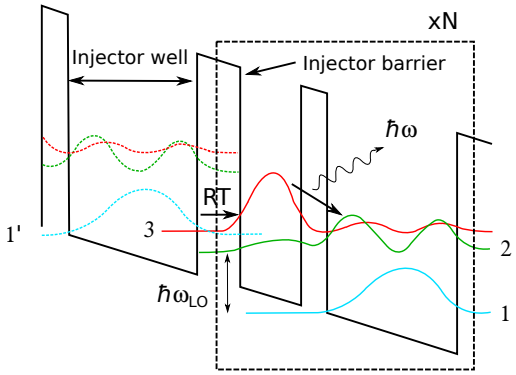

Figure 2.1.: Schematic of the 3-level system processes

temperature of 186 K was demonstrated at a frequency of 3.9 THz with 63 mW output power [33].

The further development of THz QCLs at room temperature is problematic and a new design using difference frequency generation (DFG) was demonstrated [34]. The QCL is lasing at two different wavelengths in the infrared. While they share the same cavity a high second order susceptibility allows for generation of the difference frequency, lying in the THz region. The first demonstration reached only a weak output power of 300 nW at room temperature with a frequency of 4 THz. Using a new design this was later pushed to 8.5 µW. One of the main problems is that THz radiation is nearly completely absorbed in the active region by free carrier absorption and only photons generated near the laser's facets can exit the device. A Cherenkov DFG technique was introduced allowing for an effective extraction of the THz photons throughout the whole device. The photons exit the device via the semi-insulating substrate [35]. A 10 times higher conversion efficiency has been obtained compared to conventional design with an output power of 500 nW. By an optimized heat transport and pump design 1.4 mW at 3.6 THz has been demonstrated [36] at room temperature.

2.1.2. Planar GUNN Diodes

GUNN diodes are often used as sources in the GHz range and can be pushed into the lower THz frequency range. An experimentally found lower bound for vertical devices seems to be a transit region of 1.5 µm with a corresponding frequency of the fundamental mode of 60 GHz. Simulations and measurements suggest that this limit could be overcome by a planar design of the diode [37, 38].

The device structure is similar to a HEMT without a gate, shown in figure 2.2(a). The conducting channel is formed by a material with a lower conduction band energy than the surrounding layers. One or several delta-doping layers provide free carriers which diffuse into the channel. Depending on the applied

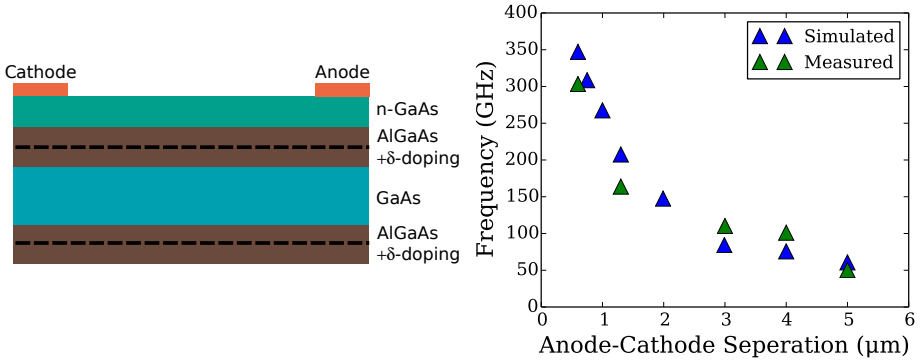

(a) Device structure (b) Frequency behaviour (data from [24])

Figure 2.2.: Schematic of the planar GUNN diode and maximum oscillation frequency as a function of the cathode-anode distance

voltage electrons move from the source contact to the channel and are accelerated. A high enough electric field can push these fast carriers to the L-valley in the semiconductor's band structure, slowing them down as the effective mass is higher compared to the Γ-valley. This leads to the formation of charge domains near the drain contact and exit the device.

A few conditions have to be met allowing the charge domains to form. The surface charge needs to deplete the surface and non-channel layer to form a flat potential profile along the vertical direction. There should be no competing conduction paths. However, a too strong depletion pushes the electrons towards the bottom of the channel and the travelling domains form ineffectively.

First experiments have been carried out in [38, 39], reaching already oscillation frequencies of 83 and 108 GHz. The latter reports an output power of 50 nW. Large improvements were found by switching to a different material system, AlGaAs/GaAs was replaced with the faster InGaAs/InP system [24]. 100 µW have been measured at a fundamental frequency of 164 GHz. Reducing the source-

drain distance to 600 nm has led to an oscillation frequency of 307 GHz with a slightly lower output power of 28 µW [40]. The measured values match quite well to performed Monte Carlo simulations [24, 37].

A different mechanism achieve GUNN-like oscillations has been supposed by Mateos and his group in [41, 42]. Induced by the high electric field peak through the recess-drain edge electrons gain enough energy to scatter into the L-valley. Degeneracy in the channel suppresses most scattering processes and pushes the carrier even faster to high velocities. The GUNN domain travel between the recess and drain contact. Higher oscillation frequencies are expected but up to now no experimental proof is available.

2.2. Plasmonic Approach

The term plasmonics relates to techniques and phenomena involving the presence of plasma waves in structures. The most prominent example is maybe the surface plasmon polariton where a electromagnetic wave is excited at an metal- or semiconductor-air interface. It involves the coupled propagation of the electromagnetic wave at the interface and the longitudinal oscillation of charges inside the metal or semiconductor.

Under certain conditions plasma waves can develop in the conducting channel in a FET. In short channels in the submicrometer range and due to the fact that the plasma wave velocity is higher than the electron drift velocity these oscillations have frequencies in the THz range. This chapter gives a review of the established theoretical models and shows later on the results of detection and emission experiments.

2.2.1. Prior Results

The existence of plasma waves, or plasmons, in FETs has been shown far before the hydrodynamic model of Dyakonov and Shur was established. The first experiments have been carried out in [43]. They used a grating to couple far-infrared radiation to the inversion layer of a n-channel MOSFET, kept at cryogenic temperatures, and measured the absorption spectrum. The appearing absorption peak was denoted to the excitation of plasma waves in the channel. The plasma frequency is given by the theory in [44]

$$\omega_p^2 = \frac{ne^2}{m^*} k \left(\epsilon_{\mathrm{Si}} + \epsilon_{\mathrm{Ox}} \coth(kd)\right)^{-1} \tag{2.1}$$

$$k = 2\pi/l \tag{2.2}$$

where ω_p is the plasma frequency, n the electron concentration, m^* the semiconductors effective mass, e the elementary charge, the dielectric constant of

the different material ϵ and the gate to channel distance d. The wave vector k is given by the length l of the grating deposited on the device. A shift in the plasma peak is induced by tuning the electron concentration with changing the gate voltage. Following the same theory [28] demonstrated the emission of far-infrared radiation with a similar device.

2.2.2. Dyakonov-Shur Model

Beginning in 1993 the topic gets a revival. Dyakonov and Shur established a new formalism based on hydrodynamic equations. They suggested that a FET channel serves as a cavity for plasma waves with frequencies in the THz range [29]. The proposed model treats the electron gas like a electron fluid, where the following assumptions have to been made:

- Many electron-electron collisions
- Non-degenerated materials: Pauli principle can be neglected
- Ballistic transport: no scattering with impurities and phonons
- Linear regime: all quantities in the device are constant

The proposed equations are the Euler equation, known from fluid dynamics, and the continuity equation:

$$\frac{\partial v}{\partial t} + v\frac{\partial v}{\partial x} + \frac{e}{m^*}\frac{\partial U}{\partial x} + \frac{v}{\tau} = 0 \tag{2.3}$$

$$\frac{\partial n}{\partial t} + \frac{\partial (nv)}{\partial x} = 0 \tag{2.4}$$

With the average drift velocity v, the electric potential U, the momentum relaxation time τ and the gate to channel capacitance C. The quantities n, v and U are a function of time and position. Furthermore the gradual channel approximation is applied, meaning that the transverse electric field is much larger than the longitudinal field along the channel. The electron concentration can then be expressed by:

$$n = CU/e \tag{2.5}$$

$$C = \epsilon/d \tag{2.6}$$

The device structure is a simplified FET, shown in figure 2.3. The gate covers the whole device and the channel is surrounded by a non-conducting dielectric layer. By applying a source-drain voltage a current flows, where the current density can be controlled by the gate.

Dyakonov and Shur solve the system with the premise of asymmetric boundary conditions. The voltage potential is fixed at the source and a constant current at

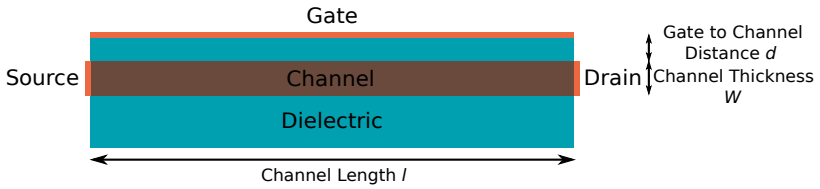

Figure 2.3.: The simplified gated FET structure

the drain contact is assumed. These boundary conditions can be compared with the transmission line model, a zero impedance (short circuited) at the source and an infinite impedance at the drain (open). It was shown that the velocity difference between waves moving towards the source and drain is different and leads to an instability in the steady state current flow. The growth of plasma waves is damped by scattering with phonons or impurities and the viscosity of the electron fluid.

Later on the model was extended to include the viscosity [45] and for transient simulations showing the plasma wave growth [46]. The hydrodynamic transport model was used to show that in analogy to the choking of sound waves in a pipe, the choking of electron flow can be a current saturation mechanism at cryogenic temperatures [47].

In [48] Dyakonov has made the same considerations for an ungated structure. Deploying asymmetric boundary conditions leads to an instability and plasma waves develop, having a higher frequency compared to the gated structure. The dispersion relations given by [29, 48] can be written as:

$$f_{\text{ungated}} = \frac{1}{2\pi}\sqrt{\frac{e^2 n k}{2\epsilon m^*}} \tag{2.7}$$

$$f_{\text{gated}} = \frac{1}{2\pi}\sqrt{\frac{e^2 n d}{\epsilon m^*}}k \tag{2.8}$$

With the assumed boundary conditions the device length corresponds to a $\lambda/4$ distance and the wave vector can be written as $k = \pi/2L$. Figure 2.4 plots the dispersion relations for the gated and ungated cases, a dielectric surrounding with $\epsilon_r = 1$ is assumed. Here, the term dispersion relations relates the resonant frequency to the concrete device geometry. A higher permittivity reduces the plasma frequency.

2.2.3. Application of the Dyakonov-Shur Instability

The publication of the proposed mechanism to generate plasma waves with frequencies in the THz range has been followed by a vast number of experimental observations. It has been used for detection as well as for emission experiments. In the next two sections a review of the major achievements is given.

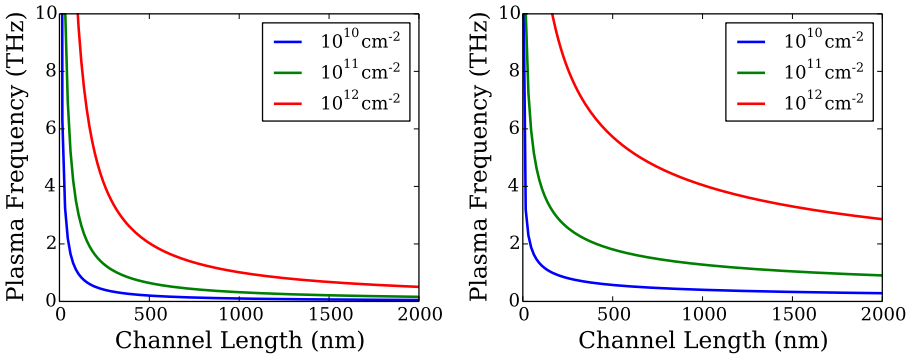

(a) Gated (b) Ungated

Figure 2.4.: Dispersion relations for the gated and ungated structures

2.2.3.1. Detection of THz Radiation

The detection process of THz radiation using the Dyakonov-Shur approach was first suggested in [49]. An incoming THz signal is fed to the structure as a gate-source voltage and due to the nonlinear plasma wave properties of the channel a constant source-drain voltage is generated through a rectification process. The most important part of the rectifying properties can be understood by the product nv in the continuity equation. Both quantities depend on the gate voltage, hence these oscillations generate a time-independent electric field [50]. Depending on the responsivity as a function of the frequency the theory distinguishes between a resonant and a nonresonant detection process. In the case of resonant detection the responsivity function exhibits sharp peaks at the plasma frequency and its multiples. The nonresonant case shows a nearly flat responsivity curve. A stronger damping of the plasma waves in the channel leads to nonresonant response.

Experimentally, a nonresonant detection at cryogenic temperatures was first shown in [51], followed by the observation of resonant detection in [52, 53] at cryogenic temperatures and later on at room temperature [54]. The measured responsivity functions and the plasma frequency coincided well with the Dyakonov-Shur theory. The theory gets supported by the fact that the responsivity increases when the asymmetry of the boundary conditions increase in terms of a higher drain current [55].

Today THz real-time cameras fabricated in a CMOS process are available including 1000 pixel and a noise equivalent power (NEP) in the range of tens of pW $\sqrt{\text{Hz}}^{-1}$. A nonresonant detection scheme readily allows for room temperature operation [56, 57].

2.2.3.2. Emission of THz Radiation

The hydrodynamic theory already states that the generated plasma waves can lead to the emission of electromagnetic radiation. Since the plasma waves are longitudinal waves they can not couple to the transversal electromagnetic waves. Nevertheless there is a vast number of emission experiments, proving the existence of such a mechanism. The emission process is explained by the assumption that the gate contact acts as an antenna.

Millimeter-wave emission by a GaN HEMT was measured in [58] at 8 K. The emission peak was centered at 75 GHz and took place when the transistor worked in the linear regime. However the emission frequency was far lower than the calculated one. In [59] the authors observe emission between 400 GHz and 1.4 THz at cryogenic temperatures. The emission was tunable with the drain voltage and appeared after reaching a threshold current. Boundary conditions were achieved by short-circuiting the gate and source and driving the transistor into saturation. Overall the measured power was in the nW range. Dyakonova characterized AlGaN/GaN and InGaAs/InAlAs HEMTs [60]. Devices on the basis of the GaN material system even sustained emission at room temperature. Like reported earlier the emission was threshold-like and the plasma frequencies were matching with the ungated/gated theory. Nevertheless no gate dependency was observed. The output was estimated to be 100 nW. Similar observations have been made in [61]. Additionally a decrease in the linewidth was observed with increasing drain current. It was argued that a larger drain current supports the growth of plasma waves and decreases their damping. The first observation of the plasma frequency tunability by changing the gate voltage and thus depleting the electron gas has been made in [62]. A significant shift from 750 GHz to 2.1 THz was observed. The authors claim that in previous publications no shift was observed because the gate voltage window was too small.

A japanese group fabricated a HEMT-like device structure with a grating gate deposited on top [63]. The emission was stimulated by cw or pulsed laser light illumination and electrical excitation. The emission spectrum was claimed to be due to excited plasmons in the gated region. Still the output power was 100 nW. The device was improved by substituting the metal gate contacts with regions of a doped semiconductor [64, 65]. Using the new gate contacts the emission was pushed to 1 µW. In all experiments no gate tuning was observed.

Strong THz emission with an output power of 1.8 µW was detected using a HEMT-like device in [66]. There was no gate tuning possible and neither were emission peaks observed.

2.3. Monte Carlo Method

This thesis investigates transport properties and noise phenomena in submicrometer sized FET-like structures. As the tool of choice the numerical investigations are performed using the Monte Carlo (MC) method. It is a stochastic approach for solving the Boltzmann transport equation (BTE) and relies on the generation of random numbers. The MC method naturally includes fluctuations and is valid at high energies under strong nonequilibrium conditions, as it includes the band structure or simplified band models. Furthermore it models nonlocal effects like the velocity overshoot correctly which drift-diffusion or hydrodynamic transport models under- or overestimate. The following section introduces the BTE and the MC algorithm derived from a path integral formulation.

Usually complex conduction phenomena need to be treated by an exact quantum mechanical description, involving the solution of many-body problems. Fortunately the conduction properties, the motion of electrons or holes, can be described by the kinetic theory of gases when the mean free path is larger than the de Broglie wavelength. In contrast to gases the main scattering mechanism is not scattering of particles of the same type, but rather scattering with other quasi particles like phonons or with impurities [67].

At thermal equilibrium the distribution function is given by the Fermi-Dirac distribution. In nonequilibrium the carriers are pushed to higher energies and the distribution can be described with the BTE f, which is given by [68]:

$$\left(\frac{\partial}{\partial t} + \frac{\mathbf{F}(\mathbf{r},\mathbf{k},t)}{\hbar}\nabla_{\mathbf{k}} + \mathbf{v}(\mathbf{r},\mathbf{k})\nabla_{\mathbf{r}}\right) f(\mathbf{r},\mathbf{k},t) = S \tag{2.9}$$

The force acting on charges is given by $\mathbf{F}$ and $\mathbf{v}$ denotes the group velocity of electrons given by the gradient of the band structure. On the right hand side of the BTE a scattering term S occurs which describes the in- and outscattering in the volume element. The term $S(\mathbf{k},\mathbf{k}')$ gives the scattering rate from a state $\mathbf{k}$ in the state $\mathbf{k}'$ which is weighted by the distribution itself and a factor $1-f$ covering the Pauli exclusion principle.

$$\mathbf{F} = -q\left(\mathbf{E}\cdot\mathbf{v}\times\mathbf{B}\right) \tag{2.10}$$

$$\mathbf{v} = \frac{\nabla_k E_c(\mathbf{k},\mathbf{r})}{\hbar} \tag{2.11}$$

$$S = \int \frac{\mathrm{d}\mathbf{k}'}{(2\pi)^3}\left(S(\mathbf{k}',\mathbf{k})f(\mathbf{r},\mathbf{k}',t)[1-f(\mathbf{r},\mathbf{k},t)] - S(\mathbf{k},\mathbf{k}')f(\mathbf{r},\mathbf{k},t)[1-f(\mathbf{r},\mathbf{k}',t]\right) \tag{2.12}$$

f is not known from the start which makes the BTE nonlinear in three ways:

- Right hand side contains the Pauli exclusion factor $(1-f)$

- Scattering rates depend on f, especially the carrier-carrier scattering
- The force $\mathbf{F}$ acting on particles depends on the distribution function

The MC method is applicable to the linear BTE and the above listed cases have to be included using a self-consistent simulation scheme. Using a path integral formulation [68], the linear BTE can be expressed as a conditional probability density

$$p(\zeta, t|\zeta_0, t_0) = p_0(\zeta, t|\zeta_0, t_0) \tag{2.13}$$

$$+ \int_{t_0}^{t} \int\int p(\zeta, t|\zeta_1', t_1) S(\zeta_1'|\zeta_1) p_0(\zeta_1, t_1|\zeta_0, t_0) \mathrm{d}\zeta_1' \mathrm{d}\zeta_1 \mathrm{d}t_1 \tag{2.14}$$

where $\zeta = (\mathbf{r}, \mathbf{k})$ gives the particle state. $p_0(\zeta, t|\zeta_0, t_0)$ describes the conditional probability density that a particle at time t_0 in state ζ_0 shows up in state ζ at time t without being scattered. The second term depicts a particle propagation without scattering from state ζ_0 at time t_0 to (ζ_1, t_1), followed by a scattering to state ζ_1' and finishes drifting to state (ζ, t). p_0 is given by

$$p_0(\zeta, t|\zeta_0, t_0) = \delta(\zeta - \zeta_{\mathrm{drift}}(t|\zeta_0, t_0)) \exp\left(- \int_{t_0}^{t} S(\zeta_{\mathrm{drift}}(\tau|\zeta_0, t_0)) \mathrm{d}\tau \right) \tag{2.15}$$

where ζ_{drift} denotes the new state after applying Newton's equation of motion.

In equation 2.14 the conditional probability density appears on the right hand side in the integral. Thus it can be inserted an infinite time into itself and the Neumann series results:

$$\begin{aligned} p(\zeta, t|\zeta_0, t_0) = {} & p_0(\zeta, t|\zeta_0, t_0) \\ & + \int_{t_0}^{t} \int\int p_0(\zeta, t|\zeta_1', t_1) S(\zeta_1'|\zeta_1) p_0(\zeta_1, t_1|\zeta_0, t_0) \\ & \qquad \times \mathrm{d}\zeta_1' \mathrm{d}\zeta_1 \mathrm{d}t_1 \\ & + \int_{t_0}^{t} \int\int \int_{t_1}^{t} \int\int p_0(\zeta, t|\zeta_2', t_2) S(\zeta_2'|\zeta_2) p_0(\zeta_2, t_2|\zeta_1', t_1) \\ & \qquad \times S(\zeta_1'|\zeta_1) p_0(\zeta_1, t_1|\zeta_0, t_0) \mathrm{d}\zeta_2' \mathrm{d}\zeta_2 \mathrm{d}t_2 \mathrm{d}\zeta_1' \mathrm{d}\zeta_1 \mathrm{d}t_1 \\ & + \dots \end{aligned} \tag{2.16}$$

The first term gives the probability density for a carrier drift from time t_0 to t without being scattered. The second term describes a particle propagation from time t_0 to t_1, followed by a scattering process from state ζ_1 to ζ_1' and a drift phase from t_1 to t. An additional drift and scattering event is added for every higher term. Equation 2.16 can be interpreted as an infinite number of trajectories. Consequently a MC simulator performs a series of drift processes which are interrupted by scattering events.

The MC algorithm needs as input the probability, or the drift time, for the first scattering event. However, the direct evaluation of the integral in equation 2.15 is time consuming as the scattering rate depends on the particle state. A fictitious scattering mechanism called self-scattering is introduced which is not changing the particle state. The scattering gets now a constant Γ independent with respect to the current state. The self-scattering rate can be expressed as:

$$S_{\text{self}}(\zeta'|\zeta) = (\Gamma - S_{\text{real}})\delta(\zeta' - \zeta) \tag{2.17}$$

Evaluating the integral, utilising a constant scattering rate, is now an easy task and with the use of a random number r the time t_{scat} until the first scattering event gets:

$$t_{\text{scat}} = -\frac{1}{\Gamma(\zeta)} \ln(r) \tag{2.18}$$

When a scattering event occurs one of the various scattering processes has to be chosen. The ith scattering mechanism is selected by using a new random number r fulfilling:

$$\sum_{j=1}^{i-1} \frac{S_j(\zeta)}{\Gamma} < r <= \sum_{j=1}^{i} \frac{S_j(\zeta)}{\Gamma} \tag{2.19}$$

The implementation of the MC solver developed in this thesis is shown in the next chapter.

3. Monte Carlo Solver Implementation

In the last chapter the physical advantages of the MC method and its algorithm have already been introduced. The MC algorithm is implemented as a particle based simulation method where a vast number of electrons is represented by fewer superparticles. Holes will be neglected in this work since they are only present as thermally excited carriers in the investigated devices. Thus the hole current will be many orders of magnitude lower than the electron current. The particle propagation can be recorded over time and the transient behaviour can be analyzed afterwards.

This chapter provides an overview over the main software components and physical models incorporated into the solver and used for further investigations. First, the main sequence of the program is presented, followed by the laws of particle motion. This work deploys a nonparabolic three-valley model for the semiconductor's bandstructure which is explained, together with other material parameters needed for the calculation of the scattering rates, in section 3.3.1. The computation of the scattering rates, including phonon, alloy and impurity scattering is given in section 3.4. Section 3.5 summarizes what is happening to particles hitting a heterointerface. When simulating submicrometer-sized devices, it is necessary to correctly model the injection of carriers at ohmic contacts, described in 3.6. As already mentioned in the introduction of the BTE every process leading to a nonlinearity of the distribution function has to be included in a self-consistent fashion. The solution of the Poisson equation using the finite difference method (FDM) and the consideration of the Pauli exclusion principle is shown in section 3.7 and 3.8, respectively.

3.1. Simulator Overview

The flow chart 3.1 shows the program's main sequence. The program starts with initialization functions, setting up the material parameters, constructing the mesh and sets up, if selected, the environment for the tunneling and the Pauli principle module. The device structure, including the geometry, used materials, doping concentrations and simulation temperature is written to a configuration file and read during the initialization phase. An initial carrier distribution is created according to the doping concentration.

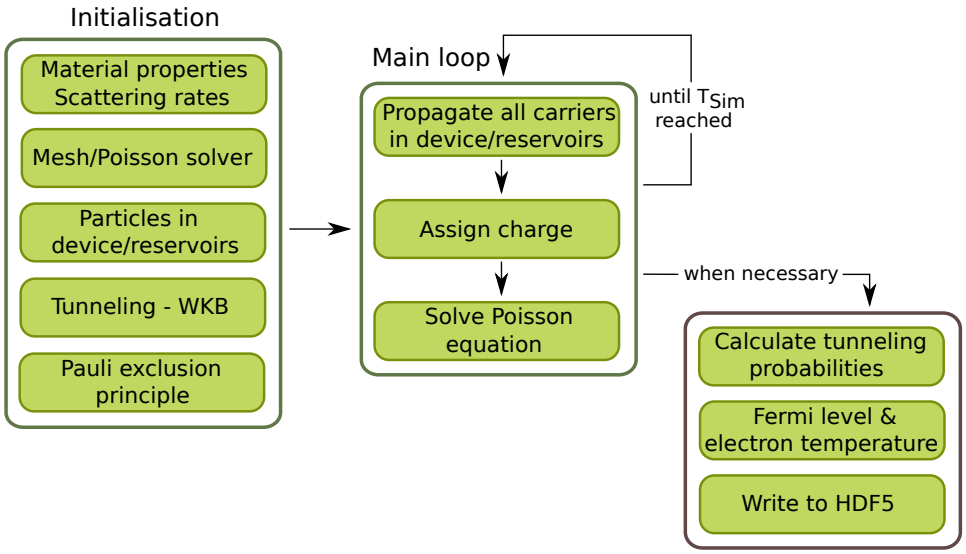

Figure 3.1.: Flowchart of the main sequence of the MC solver. The solver consists of three main parts: initilization functions, the main loop and optional functions involving more models and a saving function.

The main loop covers most of the simulation time and iterates through all particles and propagates them to the end of the current time step. The particles are then assigned to the mesh cells and the Poisson equation, considering the new charge distribution, is calculated giving the force for the next time step. The entire particle propagation ends when the total simulation time is reached which is usually given by the user. Furthermore, the Fermi level and the electron temperature can be computed to include the Pauli exclusion principle, if selected. The simulation data is written to a file using the HDF5 format for a subsequent post-processing.

3.1.1. Technical Data

All models, excluding the Pauli principle model, are available in the solver for a computation in a one-, two- or three-dimensional device domain. The computation time depends critically on the number of time steps and the number of involved scattering processes. Primarily given by the electric field strength in the device. Two-dimensional simulations performed for this thesis last typically up to one hour for the simplified FET structures and up to one day for HEMT simulations.

The solver is written in the Fortran programming language compiled with the gfortran compiler (gcc version 4.8.2). Since the particles are indepedent from

each other the propagation part can be easily parallelized with the OpenMP framework. The solution of the Poisson equation can be a tedious task since a large (depending on the number of mesh cells) system of linear equations has to be solved. This is performed with the help of the Hierarchical Iterative Parallel Solver (HIPS) package [69] using OpenMPI as a MPI (Message Passing Interface) implementation. Numerical integration and root finding problems are solved using the GNU Scientific Library (GSL). The post-processing is done using Python.

3.2. Particle Propagation

The particles move in the six-dimensional phase space. However, for most problems in this work the real space dimensions are reduced to two dimensions. Assuming small time steps the contribution of the acceleration term can be neglected and the real and reciprocal space vectors are given by [70]:

$$\mathbf{r} = \mathbf{r}_0 + \mathbf{v}\Delta t \tag{3.1}$$

$$\mathbf{k} = \mathbf{k}_0 + \frac{q\mathbf{E}\Delta t}{\hbar} \tag{3.2}$$

$\mathbf{r}_0$ and $\mathbf{k}_0$ denote the initial real space and wave vector at the start of the free flight. During the free flight time Δt, the electric field $\mathbf{E}$ acts as a force on the particles. The drift velocity

$$\mathbf{v} = \frac{\hbar\mathbf{k}}{m^*(1+2\alpha E)} \tag{3.3}$$

can be derived using the wave vector and the nonparabolicity α of the band structure. E denotes the particle's kinetic energy.

Simulator variables like the calculated electric field, material properties and the self-scattering upper bound are assigned to mesh cells in the device or reciprocal space. Thus the particle propagations has to end when one of the following events occur and the indexing variables of the particles have to be updated:

- Scattering with one of the included mechanisms
- Reaching a real space boundary
- Reaching a reciprocal space boundary
- The asynchronous phase of carrier propagation ends

The length of one time step is limited by the instability criterion for the self-consistent solution of the Poisson equation (refer to section 3.5). One time step consists of repeated phases of free flight, interrupted by the above mentioned cases [71]. The flowchart 3.2 visualises this propagation scheme: carriers start

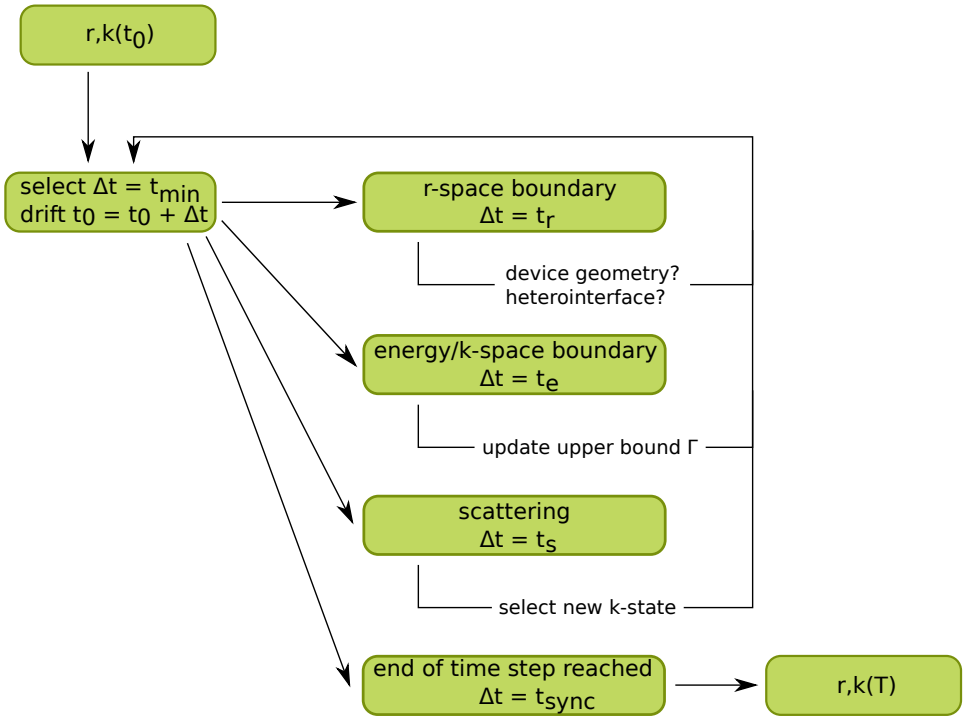

Figure 3.2.: Carrier propagation flowchart for one time step: carriers drift as long as they do not hit a boundary, which can be in real or reciprocal space, a scattering event or the end of the actual time step.

with the state $\mathbf{r}, \mathbf{k}$ at time t_0 and are propagated Δt, which is the smallest time until a boundary is reached or a scattering process takes place. This is repeated until the end of the current time step $T = t_0 + t_{\text{sync}}$. In this work the same particle propagation model as in [71] is used. The mathematical background is given in [72] proofing that the interruption of a free flight phase by an event excepting a real scattering process is not changing the overall behaviour.

The computation of the propagation time to a **r**- and **k**-space boundary in this solver is shown in the next two sections.

3.2.1. Time to Reach a Real Space Boundary

The device is discretized in equidistant steps, m_{dx} and m_{dy}, for the x- and y-direction, respectively. At the same time this mesh discretization is used for the solution of the Poisson equation. The particle's trajectory can be represented as a line given by the velocity vector. Computing the time until the particle crosses the boundary of the next mesh cell reduces then to cutting a line with a point, another line or a plane. This corresponds to a one-, two- or a three-dimensional computation, shown for the two-dimensional case in figure 3.3. From

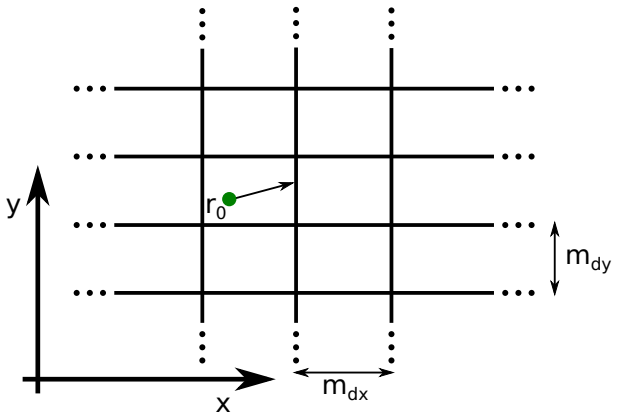

Figure 3.3.: Schematic showing the mesh discretisation in real space. The simulation domain is cut along the different directions in equidistant slices.

the resulting equations the minimum positive time has to be selected. For the two-dimensional case four equations result:

$$t_{\text{top,bottom}} = \frac{r_{\text{m,x}} \pm m_{\text{dx}}/2 - r_{0,\text{x}}}{v_x} \tag{3.4}$$

$$t_{\text{left,right}} = \frac{r_{\text{m,y}} \pm m_{\text{dy}}/2 - r_{0,\text{y}}}{v_y} \tag{3.5}$$

where $r_{\mathrm{m,x}}$ denotes the x coordinate at the center of the mesh cell and v the particle drift velocity.

3.2.2. Time to Reach a Boundary in k-Space

The k-space is represented in a three-dimensional Cartesian coordinate system. The employed bandstructure model includes three valley with spherical or ellipsoidal symmetry, for the sake of simplification the full band structure is neglected. The ellipsoidal valleys can be mapped with the Herring-Vogt transformations to spherical symmetry (compare chapter 3.3.1) and the equi-energy surfaces are spheres. Consequently, meshing in reciprocal space is done using these spheres spaced by a constant dE, shown in figure 3.4, for a cut through the k_{xy} plane.

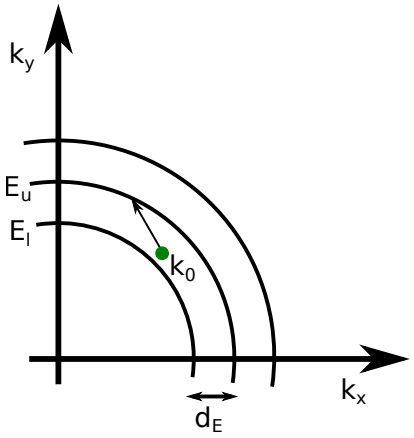

Figure 3.4.: Mesh discretisation in k-space: the equi-energy surfaces are spheres.

The time t_{e} can be derived by cutting the propagation vector Δk with the equidistantly spaced spheres. The sphere-radius r^2 has to be calculated for the lower E_{l} and upper E_{u} energy boundary using the nonparabolic bandstructure dispersion. Inserting r^2 and equation (3.7) into (3.8) and choosing the minimal positive drift time results in t_{e}.

$$r^2 = \frac{2m^*}{\hbar}(E_{\mathrm{lu}} + \alpha E_{\mathrm{lu}}^2) \tag{3.6}$$

$$A = -\frac{\mathbf{kE}\hbar}{\mathbf{E}^2} \tag{3.7}$$

$$t_{\mathrm{e}} = A^2 \pm \sqrt{(A^2 - \left(\frac{\hbar^2}{\mathbf{E}^2}(\mathbf{k}^2 - r^2)\right)} \tag{3.8}$$

3.3. Material Parameter Selection

In this work semiconductor device simulations are performed on the basis of Indium-Aluminium-Arsenide (InAlAs) and Indium-Gallium-Arsenide (InGaAs). The InGaAs/InAlAs material system is quite popular for high-frequency devices like HEMTs. Therefore, many emission experiments have been performed with this system. In most MC studies the effective masses and other parameters are used to fit the experimental findings, which can result in mismatched datasets concerning different mole fractions or temperatures. To avoid such configuration we employ a set of models to describe consistently the material properties of the two alloys, derived from the binary properties (InAs, AlAs and GaAs). Furthermore, only bulk values of the effective mass are considered and no quantization effects affecting the bandstructure are included.

3.3.1. Bandstructure Representation

This work employs a three-valley bandstructure model. The Γ-valley is modelled with spherical symmetry and the higher L- and X-valleys have ellipsoidal equi-energy surfaces. We are aware of the fact that at very high carrier energies the bandstructure differs significantly from the real dispersion relation. However this is expected not to influence the results of this thesis since high electric field domains are found rarely in the structures. This chapter presents first the employed bandstructure models and concludes with the material properties.

3.3.1.1. Dispersion Relation

The relation between the wave vector $\mathbf{k}$ and the electron energy for the spherical Γ-valley is given by

$$E(1+\alpha E) = \gamma(E) = \frac{\hbar^2 \mathbf{k}^2}{2m^*} \tag{3.9}$$

and the ellipsoidal valleys follow [70]:

$$E(1+\alpha E) = \gamma(E) = \frac{\hbar^2}{2}\left(\frac{k_\mathrm{x}^2}{m_\mathrm{x}} + \frac{k_\mathrm{y}^2}{m_\mathrm{y}} + \frac{k_\mathrm{z}^2}{m_\mathrm{z}}\right) \tag{3.10}$$

Where $m^*, m_\mathrm{x}, m_\mathrm{y}, m_\mathrm{z}$ denote the effective masses with the subscripts x,y,z describing the different orientation of the Cartesian coordinate system. At the valley bottom ($\mathbf{k} = \mathbf{0}$) particles have no kinetic energy ($E = 0$).

3.3.1.2. Density of States

The density of states is frequently used in the calculation of the scattering rates and can easily be expressed as [70]:

$$D(E) = \frac{(2m^*)^{\frac{3}{2}}}{2\pi^2\hbar^3}\sqrt{\gamma(E)}(1+2\alpha E) \tag{3.11}$$

A factor of 2 accounts for spin-degeneracy. In the case of ellipsoidal valleys the effective mass has to be replaced with the density of states effective mass

$$m_{\mathrm{DOS}} = (m_{\mathrm{l}} m_{\mathrm{t}}^2)^{\frac{1}{3}}\,, \tag{3.12}$$

representing a geometric of the longitudinal m_{l} and transversal m_{t} effective mass. The density of states effective mass can be derived using the Herring-Vogt transformation [73].

3.3.1.3. Herring-Vogt Transformations

Dealing with ellipsoidal valleys complicates things like the calculation of t_{e} in equation (3.8) or selecting a new state $\mathbf{k}'$ after a scattering process. The Herring-Vogt transformation maps the ellipsoidal equi-energy surfaces to spherical ones, simplifying the implementation [74].

In a zinc-blende crystal there are six X-valleys present and due to symmetry reasons they group pairwise along the [100], [010] and [001]-direction. The transformation matrices for the new spherical sytem $\mathbf{k}^* = T\mathbf{k}$ are [70]:

$$T_{[100]} = \begin{pmatrix} \sqrt{\frac{m_0}{m_{\mathrm{l}}}} & 0 & 0 \\ 0 & \sqrt{\frac{m_0}{m_{\mathrm{t}}}} & 0 \\ 0 & 0 & \sqrt{\frac{m_0}{m_{\mathrm{t}}}} \end{pmatrix} \quad T_{[010]} = \begin{pmatrix} \sqrt{\frac{m_0}{m_{\mathrm{t}}}} & 0 & 0 \\ 0 & \sqrt{\frac{m_0}{m_{\mathrm{l}}}} & 0 \\ 0 & 0 & \sqrt{\frac{m_0}{m_{\mathrm{t}}}} \end{pmatrix} \tag{3.13}$$

$$T_{[001]} = \begin{pmatrix} \sqrt{\frac{m_0}{m_{\mathrm{l}}}} & 0 & 0 \\ 0 & \sqrt{\frac{m_0}{m_{\mathrm{l}}}} & 0 \\ 0 & 0 & \sqrt{\frac{m_0}{m_{\mathrm{l}}}} \end{pmatrix}$$

For the L-valley the symmetry axis of the ellipsoid is not located along the main axes of the coordinate system and thus the transformation matrices include an additional rotational transformation [75]:

$$R_{[111]} = \begin{pmatrix} \frac{1}{\sqrt{3}} & \frac{1}{\sqrt{3}} & \frac{1}{\sqrt{3}} \\ -\frac{1}{\sqrt{2}} & \frac{1}{\sqrt{2}} & 0 \\ -\frac{1}{\sqrt{6}} & -\frac{1}{\sqrt{6}} & \sqrt{\frac{2}{3}} \end{pmatrix} \quad R_r[\bar{1}11] = \begin{pmatrix} -\frac{1}{\sqrt{3}} & \frac{1}{\sqrt{3}} & \frac{1}{\sqrt{3}} \\ -\frac{1}{\sqrt{2}} & -\frac{1}{\sqrt{2}} & 0 \\ \frac{1}{\sqrt{6}} & -\frac{1}{\sqrt{6}} & \sqrt{\frac{2}{3}} \end{pmatrix} \tag{3.14}$$

$$R_{[11\bar{1}]} = \begin{pmatrix} -\frac{1}{\sqrt{3}} & -\frac{1}{\sqrt{3}} & \frac{1}{\sqrt{3}} \\ \frac{1}{\sqrt{2}} & -\frac{1}{\sqrt{2}} & 0 \\ \frac{1}{\sqrt{6}} & \frac{1}{\sqrt{6}} & \sqrt{\frac{2}{3}} \end{pmatrix} \qquad R_r[1\bar{1}1] = \begin{pmatrix} \frac{1}{\sqrt{3}} & -\frac{1}{\sqrt{3}} & \frac{1}{\sqrt{3}} \\ \frac{1}{\sqrt{2}} & \frac{1}{\sqrt{2}} & 0 \\ -\frac{1}{\sqrt{6}} & \frac{1}{\sqrt{6}} & \sqrt{\frac{2}{3}} \end{pmatrix}$$

Depending on the valley, the transformation matrices for the L-valley get now RT_{100}, with R according to the valley direction.

3.3.2. Bandstructure Parameters

To keep the MC transport module as close to actual physics as possible, this thesis employs bandstructure models for the bandgaps, the effective masses and the L- and X-valley offsets in the conduction band. The solver covers the binary materials GaAs, InAs and AlAs. Additionally the parameters for their ternary alloys $In_xGa_{1-x}As$ and $In_xAl_{1-x}As$ can be derived from the binaries. Mole fraction and temperature dependency is considered. In most cases the recommended values given in the review of III-IV semiconductor parameters [76] are used. The review includes theoretical and experimental values and tries to give an overall parameter estimation.

3.3.2.1. Bandgap and Valley Offsets

The Varshni expression (3.15) describes the temperature dependency of the bandgap and the valley offsets with a simple equation [76]:

$$E_g(T) = E_g(T=0) - \frac{\alpha T^2}{T+\beta} \tag{3.15}$$

$E_g(T=0)$ gives the bandgap at a temperature T of 0 K and α and β are the adjustable Varshni parameters. For ternary alloys the energy gaps can be interpolated by applying an additional bowing parameter, accounting for the difference to a linear interpolation scheme.

$$E_{\mathrm{g}}(A_{1-x}B_x) = (1-x)E_{\mathrm{g}}(A) + xE_{\mathrm{g}}(B) - x(1-x)C \tag{3.16}$$

The nonlinearity is induced by disorder effects of the different cat- and anions [76].

Figure 3.5 and 3.6 show the calculated energy gaps for InGaAs and InAlAs. The plots show on the left y-axis the total energy (straight line), where 0 eV is defined as the top of the valence band. A second y-axis denotes only the energy distance between the Γ- and the higher valleys (dashed line).

The subfigures 3.5(a) and 3.6(a) give the band gap and valley offsets for the mole fractions of 53 % and 52 %, respectively. These mole fractions have the important property that they have an equal lattice constant and are lattice matched to an InP substrate. With increasing thermal energy the band gap decreases due to the stronger interatomic motion. The crystal expands and the potential seen by electrons decreases. Most authors of MC programs employ constant valley

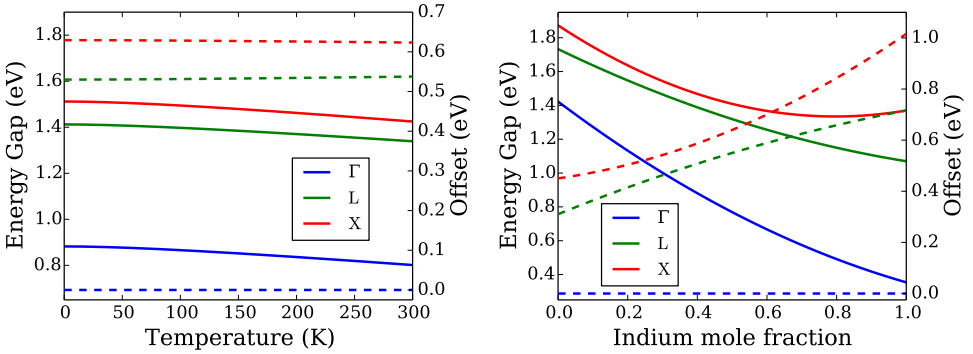

(a) Energy gaps for the three different valleys as a function of temperature for an indium mole fraction of $x = 0.53$

(b) Composition dependency at 300 K as a function of the mole fraction for the three valleys

Figure 3.5.: Computed valley offsets of $In_xGa_{1-x}As$. The left axis gives the energy gap with respect to the top of the valence band. The right y-axis give the gaps relative to the bottom of the conduction band.

offsets for the complete temperature range, justified by the results in 3.5(a) and 3.6(a).

However, the ternary material bandstructures exhibit a strong dependency on the mole fraction. InGaAs, shown in figure 3.5(b), stays a direct semiconductor while the bandgap decreases with increasing indium content. The energy offsets of the higher valleys in InGaAs are quite unclear in the literature (e.g. [76]). Thus, the bowing parameters are found by numerical experiments and comparison to experimental values for different bowing parameters. This will be shown in detail in section 4.1.1.1 covering the calibration results. For InAlAs the situation is more complicated since adding aluminium has a great impact on the bandstructure. At an aluminium concentration of 42 % InAlAs changes its properties to an indirect semiconductor. InAlAs is used as a barrier material for InGaAs based devices since its bandgap is in most cases much larger and allows for an efficient electron confinement.

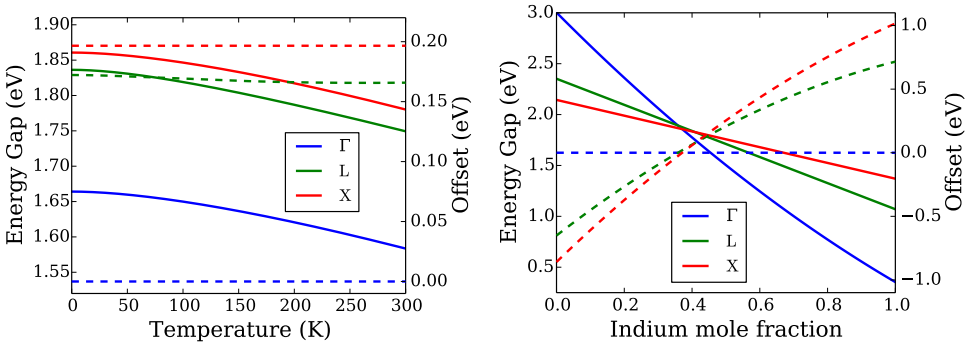

(a) Energy gaps for the three different valleys as a function of temperature for an indium mole fraction of $x = 0.52$

(b) Composition dependency at 300 K as a function of the mole fraction for the three valleys

Figure 3.6.: Computed valley offsets of $In_xAl_{1-x}As$. The left axis gives the energy gap with respect to the top of the valence band. The right y-axis give the gaps relative to the bottom of the conduction band.

3.3.2.2. Effective Masses

The spherical Γ-valley is characterized by one effective mass. For the ellipsoidal valleys a longitudinal and transversal mass needs to be defined. The effective masses can be derived using the expression with basic band parameters given in [76]:

$$\frac{m_0}{m^*} = (1 + 2F) + \frac{E_P(E_g + 2\Delta_{so}/3)}{E_g(E_g + \Delta_{so})} \tag{3.17}$$

where the factor F denotes higher band contributions to the conduction band, E_P describes the matrix element between s-like conduction and p-like valence bands and the split-off energy of the valence bands is given by Δ_{so}. All given parameters in [76] are constant over the entire temperature range and temperature dependency of the effective masses is only included indirectly using the bandgap expression (3.15). The temperature dependent effective masses for the binary materials are given in figure 3.7. The trend of the effective mass curves follows the bandgap temperature behaviour meaning that the effective masses decrease with temperature. Expression (3.16) is used for the interpolation of the Γ-valley effective mass for the ternaries, using the bowing paramters given in [76]. Due to the lack of sophisticated theoretical and experimental data the longitudinal and transversal masses are interpolated linearly and temperature dependency has to be neglected.

Figure 3.8 and 3.9 show the effective masses for the Γ-, X- and L-valley, respectively. In general the InGaAs alloys have smaller effective masses compared

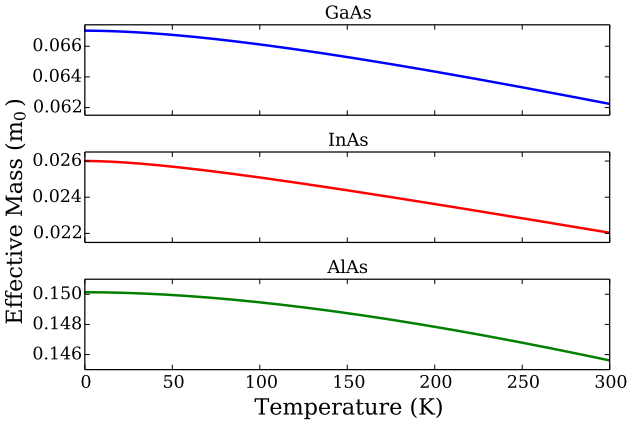

Figure 3.7.: Calculated Γ-valley effective masses for the three binary materials forming the base for the ternary materials

to other semiconductors making them an excellent choice for high frequency components. Additionally, the material can reach higher drift velocities as indium is added.

3.3.3. Other Parameters

While the bandstructure parameters are fixed, the unknown parameters for the computation of the scattering rates need to be found. The lattice constant, material density, sound velocity and the permittivity will be interpolated linearly. Additionally, the permittivity plays an important role in the calculation of the electric field as it enters the Poisson equation. The lattice constants are taken from [76], the density and sound velocities from [77]. The static and high frequency permittivities can be found in [78] and the permittivity for AlAs was extrapolated using the permittivity of $In_{0.52}Al_{0.48}As$ found in [79].

Missing parameters like the deformation potentials and phonon energies are taken from other Monte Carlo publications [80, 81], due to the lack of experimental data. The dependency on composition and temperature is neglected.

The alloy scattering potential follows the values in [82] and the small dependence on mole fraction is omitted since the change is small. An average value for a mole fraction of 50 % is used. The chosen parameters are summarized in appendix A.

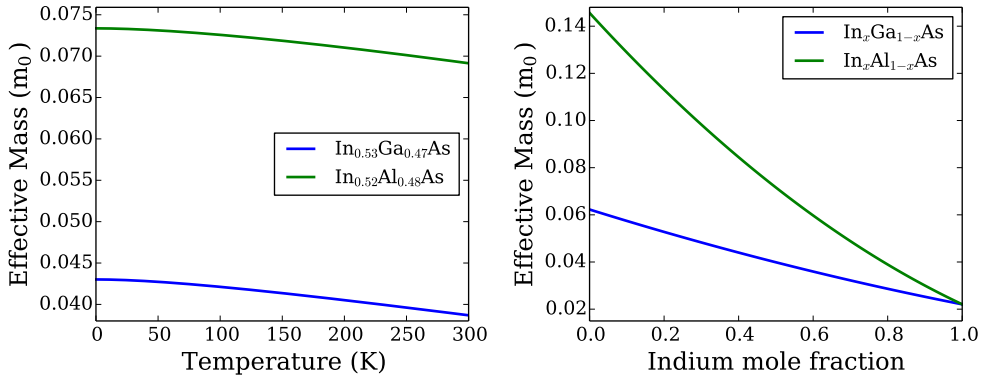

(a) Γ-valley effective mass of $In_{0.53}Ga_{0.47}As$ and $In_{0.52}Al_{0.48}As$ as a function of temperature

(b) Composition dependency at 300 K of the Γ-valley effective mass

Figure 3.8.: Calculated Γ-valley effective masses for $In_xGa_{1-x}As$ and $In_xAl_{1-x}As$

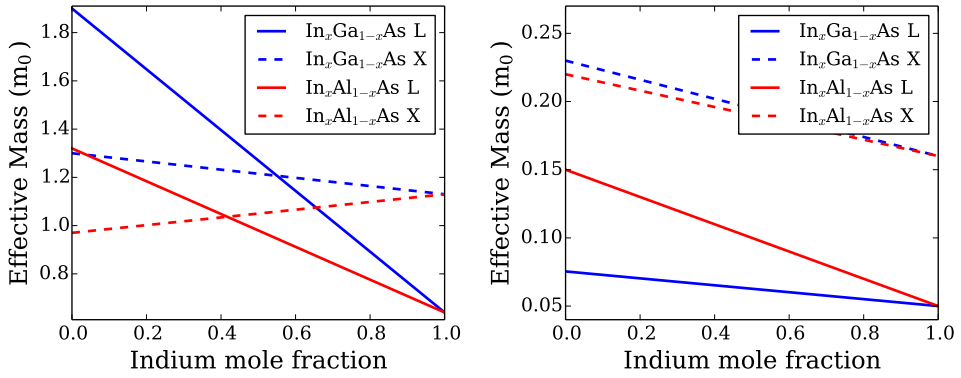

(a) Transveral effective masses

(b) Longitudinal effective masses

Figure 3.9.: The L- and X-valleys are modelled as ellipsoidal valleys and have to be described with a transversal and longitudinal mass. The effective masses are shown for 300 K as a function of the indium mole fraction.

3.4. Scattering Rates

This chapter reviews the scattering processes incorporated into the MC solver. Different types of phonon scattering, alloy scattering and ionized impurity scattering are computed using compact equations.

3.4.1. Phonon Scattering

Scattering with phonons is the main mechanism limiting the mobility in a semiconductor. The phonon scattering rate scales strongly with temperature since the number of phonons in a crystal is described by the phonon occupation number

$$N = \left(e^{\frac{\hbar\omega}{k_\mathrm{B}T}} - 1 \right)^{-1} . \tag{3.18}$$

The equations for the different scattering rates S are derived from Fermi's golden rule and are proportional to the density of states D and a fitting parameter, often a deformation potential.

3.4.1.1. Acoustic Phonon Scattering

Acoustic phonons are the quantized sound wave-like modes in a crystal. Scattering with acoustic phonons is a weak intravalley scattering process. Especially at the Brillouin zone center the energy of an acoustic phonon is very small and the process is often treated elastic, only changing particle momentum. However, at low temperatures or when an accurate energy distribution has to be obtained, the energy exchange has to be included.

Inelastic Acoustic Phonon Scattering

This work follows the analytic formulation for nonparabolic spherical or ellipsoidal bands and a linear approximated dispersion relation [83, 84]:

$$S_{\mathrm{ac,ine}}(E)\mathrm{d}x = \frac{\sqrt{m^*}(k_B T)^3 D_{\mathrm{ac}}^2}{2^{\frac{2}{5}}\pi\hbar^4 s_\mathrm{l}^4 \rho\sqrt{\gamma(E)}}(1 + 2\alpha E \mp 2\alpha k_B T x)x^2\mathrm{d}x \tag{3.19}$$

$$x = \frac{\hbar q s_\mathrm{l}}{k_B T} \tag{3.20}$$

Where $S_{\mathrm{ac,ine}}$ describes the scattering rate for absorption and emission processes, respectively. ρ denotes the material density and s_l the longitudinal sound velocity. After scattering equation (3.19) has to be used to select a final state after scattering with the help of the rejection method. After a value for x is found according to the probability function, the energy can be computed using the corresponding wave vector q calculated with equation (3.20).

From equation (3.19) the scattering rate as a function of the particle energy

E can be derived:

$$S_{\mathrm{ac,ine}}(E) = \frac{\sqrt{m^*}(k_B T)^3 D_{\mathrm{ac}}^2}{2^{\frac{2}{5}}\pi\hbar^4 s_{\mathrm{l}}^4 \rho\sqrt{\gamma(E)}} \begin{cases} ((1+2\alpha E)G_1 - 2\alpha k_B T G_2) \\ ((1+2\alpha E)F_1 + 2\alpha k_B T F_2 \end{cases} \tag{3.21}$$

$$G_1 = \int_{x1e}^{x2e} (N_{\mathrm{q}}(x)+1)x^2 \mathrm{d}x \tag{3.22}$$

$$F_1 = \int_{x1a}^{x2a} N_{\mathrm{q}}(x)x^2 \mathrm{d}x \tag{3.23}$$

$$G_2 = \int_{x1e}^{x2e} (N_{\mathrm{q}}(x)+1)x^3 \mathrm{d}x \tag{3.24}$$

$$F_2 = \int_{x1a}^{x2a} N_{\mathrm{q}}(x)x^3 \mathrm{d}x \tag{3.25}$$

$$\tag{3.26}$$

At low temperatures and high energies the values of the integrals diverge significantly from the given series expansion in [83, 84]. Thus the integration is performed numerically.

Elastic Acoustic Phonon Scattering

For the sake of completeness the MC solvers implements the elastic scattering case as well. If not stated otherwise, the inelastic formulation is used in this thesis. In the case of high electric or higher temperatues the process can be treated elastically since the thermal carrier energy will be large compared to energy lost or gained by the phonon scattering. The elastic phonon scattering rate is given by [85, 86]:

$$S_{\mathrm{ac,el}}(E) = \frac{\pi k_{\mathrm{B}} T D_{\mathrm{ac}}^2}{\hbar s_{\mathrm{l}}^2 \rho} D(E) \tag{3.27}$$

Following the latter publication we ignore the term F_α introduced by Fawcett [85]. Isotropic scattering is assumed, meaning that every state on the equi-energy sphere has an equal probability.

3.4.1.2. Optical Phonon Scattering

In contrast to the acoustic type optical phonons describe out of phase movements of atoms in the crystal. They have a much larger energy and are often treated with a constant energy throughout the Brillouin zone (Einstein approximation).

Nonpolar Optical Phonon Scattering

The scattering rate is given by [70]:

$$S_{\text{nonp}}(E) = \frac{\pi D_{\text{nonp}}^2}{2\rho\omega_{\text{op}}}\left(N_{\text{op}} + \frac{1}{2} \pm \frac{1}{2}\right) D(E \mp \hbar\omega_{\text{op}}) \tag{3.28}$$

ω_{op} denotes the angular optical phonon frequency and N_{op} its corresponding occupation number. The scattering rate S_{nonp} describes absorption and emission processes.

Polar Optical Phonon Scattering

The polar optical phonon scattering is the dominating scattering mechanism in a crystal where the basis consist of two different species. To be able to follow the DOS-ansatz we use the formulation of the direction-weighted density of states $D_{\text{q}^{-2}}$ used by Dolgos [71] which is similar to the formulation given in [85].

$$D_{\text{q}^{-2}} = \frac{\frac{e^2\sqrt{m^*}\omega_{\text{op}}}{\sqrt{2}\hbar}\left(\frac{1}{\epsilon_\infty} - \frac{1}{\epsilon_{\text{s}}}\right)\frac{1+2\alpha E'}{\sqrt{\gamma}}}{\frac{2\pi}{\hbar}e^2F^2} F_0(E, E') \tag{3.29}$$

$$F^2 = \frac{\hbar\omega_{\text{op}}}{4}\left(\frac{1}{\epsilon_\infty} - \frac{1}{\epsilon_{\text{s}}}\right) \tag{3.30}$$

$$F_0(E, E') = \frac{1}{C}\left(A \ln\left|\frac{\sqrt{\gamma} + \sqrt{\gamma'}}{\sqrt{\gamma} - \sqrt{\gamma'}}\right| + B\right) \tag{3.31}$$

$$A = (2(1+\alpha E)(1+\alpha E') + \alpha(\gamma + \gamma'))^2 \tag{3.32}$$

$$B = -2\alpha\sqrt{\gamma\gamma'}(4(1+\alpha E)(1+\alpha E') + \alpha(\gamma + \gamma')) \tag{3.33}$$

$$C = 4(1+\alpha E)(1+\alpha E')(1+2\alpha E)(1+2\alpha E') \tag{3.34}$$

The polar coupling constant is given by the Fröhlich expression [87] where ϵ_{s} and ϵ_∞ are the static and high frequency permittivities. $E' = E \pm \hbar\omega_{\text{op}}$ denotes the final electron energy after an absorption or emission process, respectively. Using the direction-weighted DOS the scattering rate can be expressed by:

$$S_{\text{pop}}(E) = \frac{1}{2\hbar}e^2F^2\left(N_{\text{op}} + \frac{1}{2} \pm \frac{1}{2}\right) D_{\text{q}^{-2}}(E) \tag{3.35}$$

The new wave vector can be found using the probability distribution given in [85]:

$$P(\beta)\mathrm{d}\beta \sim \frac{(\sqrt{\gamma}\sqrt{\gamma'} + \alpha E E' \cos\beta)^2}{\sqrt{\gamma} + \sqrt{\gamma'} - 2\sqrt{\gamma}\sqrt{\gamma'}\cos\beta}\sin\beta\mathrm{d}\beta \tag{3.36}$$

Scattering with polar optical phonons as described by S_{pop} is an intravalley scattering process and favours small scattering angles which can be found using

the rejection method. By integration by substitution of β with $\cos\beta$ it follows for equation (3.35):

$$P(\beta) = \frac{P(\cos\beta)}{\sin\beta} \tag{3.37}$$

Thus, the maximum value of the distribution can found analytically for $\cos\beta = 1$ serving as an upper bound for the rejection method.

3.4.1.3. Intervalley Scattering

Long wavelength scattering with acoustic or optical phonons can lead to equivalent ($L \leftrightarrow L$ or $X \leftrightarrow X$) and nonequivalent ($\Gamma \leftrightarrow L$, $\Gamma \leftrightarrow X$ or $L \leftrightarrow X$ intervalley scattering. The carrier momentum in the new valley is randomized and the intervalley separation ΔE and the phonon energy $\hbar\omega_{\mathrm{iv}}$ are subtracted or added to the particle's kinetic energy. The scattering rate can be expressed as [70]:

$$S_{\mathrm{iv}}(E) = \frac{\pi Z_{\mathrm{f}} D_{\mathrm{iv}}^2}{2\rho\omega_{\mathrm{iv}}} \left(N_{\mathrm{iv}} + \frac{1}{2} \pm \frac{1}{2} \right) D(E \mp \hbar\omega_{\mathrm{iv}} - \Delta E) \tag{3.38}$$

The scattering rate scales with the intervalley deformation potential D_{iv} and the number of equivalent final valleys Z_{f}.

3.4.2. Alloy Scattering

In this work the used semiconductor alloys like InAlAs or InGaAs are compounds of two binary semiconductor systems having the same group-V element. Due to the random fluctuation of the periodical crystal potential a momentum scattering is introduced. The new **k**-state will be chosen isotropically in the current valley. The alloy scattering rate follows [88, 89]. These scattering rates are slightly lower than given by Ridley in [86].

$$S_{\mathrm{alloy}}(E) = \frac{3\pi^3}{16\hbar} x(1-x)\Omega U_{\mathrm{alloy}}^2 D(E) S \tag{3.39}$$

$$\Omega = \frac{a^3}{4} \tag{3.40}$$

A complete randomization ($S = 1$) is assumed. The alloy scattering rate is proportional to the density of states and the interaction potential U. The unit cell volume Ω can be calculated using the lattice constant a. x denotes the mole fraction.

3.4.3. Ionized Impurity Scattering

Ionized impurity scattering describes the interaction with dopants incorporated into the crystal. Typically it can be neglected at high electric fields but plays a strong role at cryogenic temperatures when the number of phonons will be low. The scattering rate is computed using Ridley's statistical screening model [90] depending on the Brooks-Herring model [70]. Ridley's model includes scattering with the presence of a second impurity and avoids the strong increase of the scattering rate at lower temperatures. The scattering rate S_{imp} can be written as:

$$S_{\mathrm{imp}}(E) = \frac{|v(E)|}{R} 1 - \exp\left(-\frac{S_{\mathrm{BH}} R}{|v(E)|}\right) \tag{3.41}$$

$$R = (2\pi N_{\mathrm{dop}})^{\frac{1}{3}} \tag{3.42}$$

$$S_{\mathrm{BH}}(E) = \frac{\sqrt{2} N_{\mathrm{dop}} Z^2 e^4}{\epsilon_{\mathrm{s}}^2 E_\beta^2 \sqrt{m^*}} \sqrt{\gamma(E)} \frac{1 + 2\alpha E}{1 + 4\frac{\gamma(E)}{E_\beta}} \tag{3.43}$$

$$E_\beta = \frac{\hbar^2 \beta^2}{2m^*} \tag{3.44}$$

$$\beta = \sqrt{\frac{e^2 n_0}{\epsilon_{\mathrm{s}} k_B T_0}} \tag{3.45}$$

where S_{BH} is the original Brooks-Herring scattering rate, R the average distance between impurities, Z the number of charges per impurity and β denotes the inverse screening length. The assumption of non-degenerated statistics and an independence of the screening length of the carrier temperature is made. Scattering with ionized impurities is an elastic process and a new wave vector needs to be selected. The scattering angle is chosen following the Brooks-Herring formulation and the introduced error in the simulations is estimated to be small. The crossover to a Conwell-Weisskopf distribution [83] at low temperatures and relevant at small electric fields is neglected. Ionized impurity scattering is only implemented in the Γ-valley since in the higher valleys intervalley scattering dominates.

3.4.4. Self-Scattering

The simple expression of equation (2.18) for the free flight time before the next scattering event takes place relies on a constant scattering rate. A fictitious scattering mechanism called self-scattering is introduced not changing the particle's state. Instead of a constant upper bound throughout the full energy range, introducing a very high number of self-scatterings at low energies and thus computational intensive interruption of drift processes, a piecewise constant upper

bound is chosen. Figure 3.10 shows all implemented scattering rates, these can be summed up to the total physical scattering rate. Adding the self-scattering process gives a piecewise constant scattering rate.

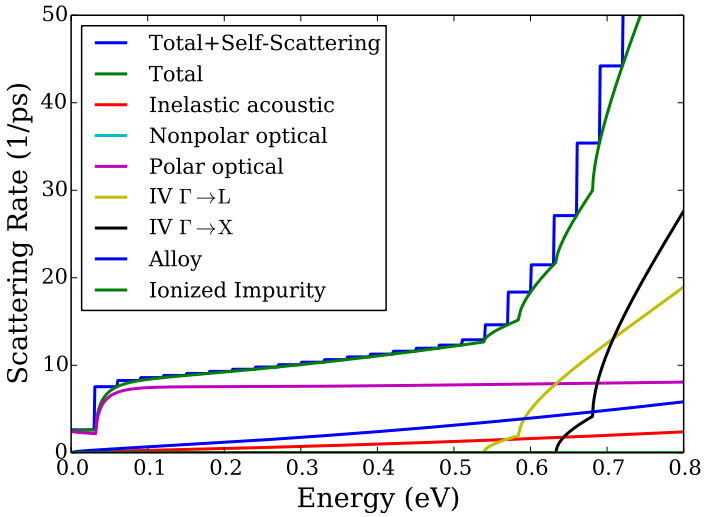

Figure 3.10.: Scattering rates including the self-scattering mechanism

3.4.5. Scattering Rate Results

This section gives the results for the computed scattering rates for the three different valleys for the $In_{0.53}Ga_{0.47}As$ and $In_{0.52}Al_{0.48}As$ alloys. The smaller effective masses for $In_{0.53}Ga_{0.47}As$ compared to $In_{0.52}Al_{0.48}As$ leads to a lower scattering rate and thus to a larger low field mobility, which will be shown in the calibration results chapter4.2. In the Γ-valley scattering with optical phonons is the main scattering process until the onset of intervalley transfer. Results for ionized impurity scattering are given for a doping concentration of $1 \times 10^{18}\,\mathrm{cm}^{-2}$. Since self-scattering is no real physical scattering mechanism it is omitted.

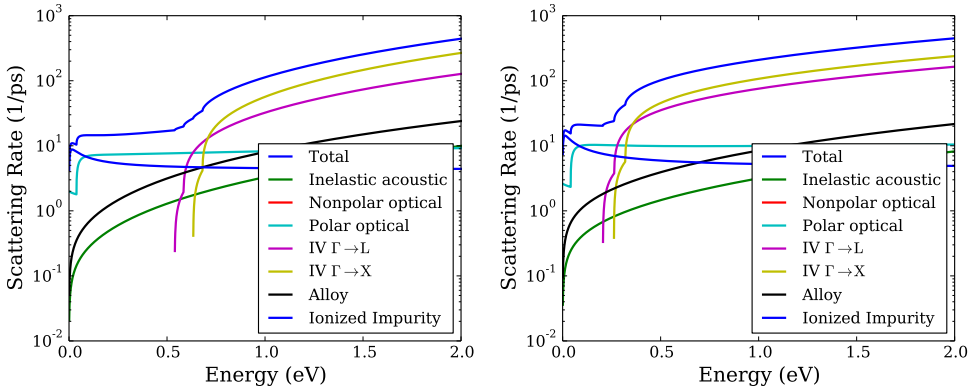

(a) Γ-valley InGaAs

(b) Γ-valley InAlAs

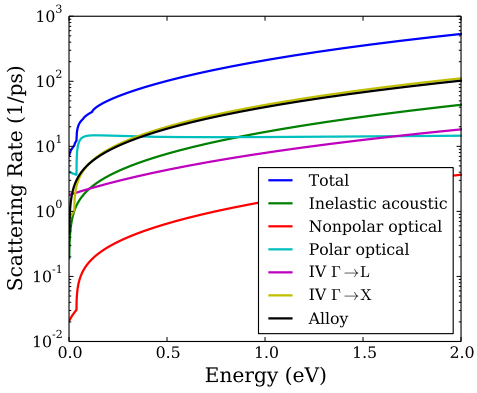

(c) *L*-valley InGaAs

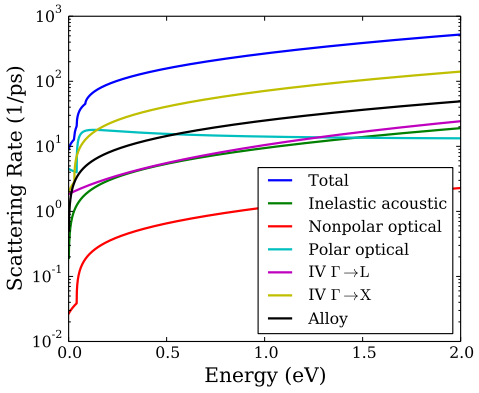

(d) *L*-valley InAlAs

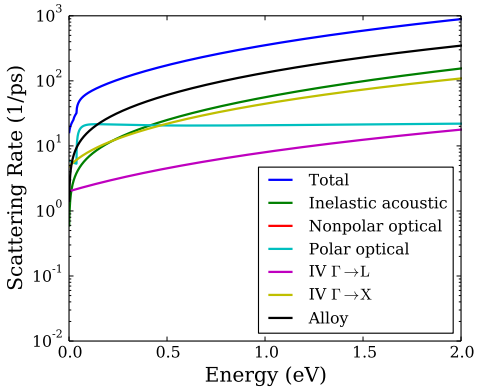

(e) *X*-valley InGaAs

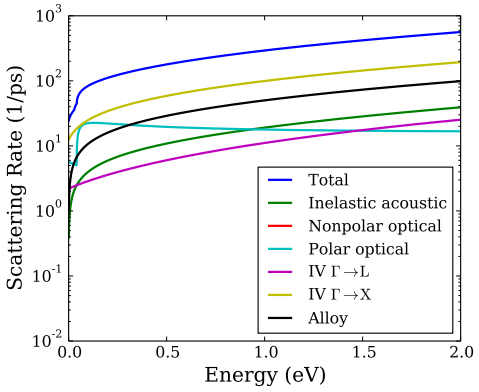

(f) *X*-valley InAlAs

Figure 3.11.: Calculated scatterings rates for $In_{0.53}Ga_{0.47}As$ and $In_{0.52}Al_{0.48}As$ at 300 K

3.5. Heterojunctions

Modern devices rely on vertical structures, forming heterostructures or superlattices. The solver treats carriers hitting a heterojunction classically meaning energy and parallel momentum have to be conserved [91, 92]. Figure 3.12 shows a channel surrounded by a layer with a higher bandgap resulting in this case in a conduction band offset ΔE_C. The band offsets for InGaAs/InAlAs are taken from [76]. When a particle hits the barrier and the kinetic energy is smaller than ΔE_C it will be reflected, otherwise it can transfer to the next material sometimes referred to real-space electron transfer. The heterojunction band offset has to be subtracted from the particle's kinetic energy. During the transfer carriers remain in their original valley. Additionally, carriers can quantum-mechanically tunnel through barriers. This has been implemented using the Wentzel-Kramers-Brillouin (WKB) approximation but is not used for results presented in this study.

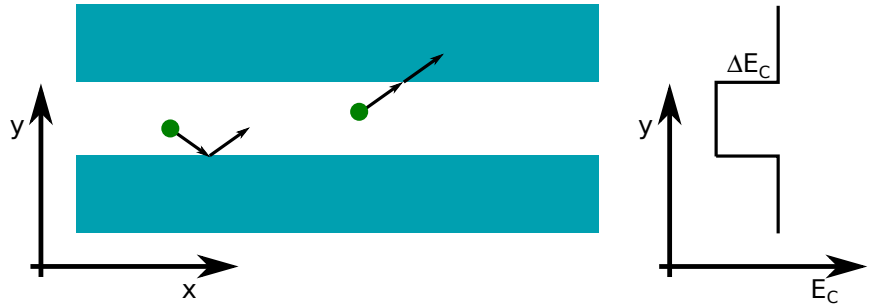

Figure 3.12.: Schematic of a surrounded channel and its corresponding band diagram

3.6. Ohmic Contacts

Boundary conditions are crucial for semiconductor device simulation. They are considered in the solution of the Poisson equation providing the internal electric field distribution and thus represent driving forces. Furthermore, from the carrier's point of view, they let particles enter and exit the device. While Schottky contacts absorb carriers, ohmic contacts allow a carrier injection. An ohmic contact is characterized by a small or disappearing Schottky barrier between the semiconductor and the contacting metal. The contact retains the equilibrium electron concentration and no voltage drop occurs over the contact. Especially for small devices an unphysical voltage drop would lead to a degraded device performance since the driving electric field would be lowered.

This work follows the model presented in [93] with modifications for an improved parallel computational performance. Carriers are injected with a velocity-weighted Maxwellian distribution function which is additionally displaced to conserve the current. A different velocity distribution function leads to a carrier injection having a too low velocity and leads to an accumulation near the contact:

$$f(v) \propto v \exp\left(-\frac{m^*(v - v_\mathrm{d}}{2k_\mathrm{B}T}\right) \tag{3.46}$$

Where the velocity $v_\mathrm{d} = \frac{J}{qN_\mathrm{D}}$ is given by the current J through the device and the doping concentration N_D. It has to be noted that only the velocity component perpendicular to the interface is chosen by the velocity-weighted distribution function. The missing velocity components parallel to the interface are given by an unmodified Maxwellian distribution. Having fixed the velocities, the particles wave-vector and energy can be calculated.

The solver requires as input how many particles have to be injected and at which simulation time they have to enter the device to ensure equilibrium conditions. In [93] the time particles spend in the contact's mesh cells are tabulated and particles with a random propagation drift time are injected until an equilibrium carrier concentration is reached. However, this approach is unpracticable for a heavily parallelized MC program since carriers have to be injected iteratively. It is not a priori known which path particles choose and if they cross other mesh cells. The next particle injection always depends on the previous injected carrier. This injection mechanism was exchanged by a small reservoir (half of a mesh cell) of particles naturally crossing the device boundary. The reservoir needs to be small enough to prevent unnatural induced charge oscillations. The influence on the transient behaviour was carefully checked. The number of particles is fluctuating according to the electron concentration present at the boundary. No particles are injected when the electron concentration is larger than the doping concentration.

3.7. Self-Consistent Electric Field

The following two sections introduce the self-consistent models employed in the solver namely the solution of the Poisson equation giving the force acting on particles and the inclusion of the Pauli exclusion principle.

The linear Poisson equation is the only field equation used in this study since the magnetic field is usually negligible in semiconductor device simulation:

$$\nabla\epsilon\nabla\phi = -\rho \tag{3.47}$$

$$\mathbf{E} = -\nabla\phi \tag{3.48}$$

Where ϕ and $\mathbf{E}$ denote the electric potential and field, respectively. The space charge distribution is given by $\rho = p - n + N_\mathrm{D} - N_\mathrm{A}$, where n and p describe the electron and hole concentration while the donor and acceptor density is given by N_D and N_A. In an intrinsic semiconductor or when the carrier densities equal the doping concentrations the space charge is zero and no electric fields arise.

The Poisson equation is solved using the finite-difference method (FDM) and the resulting system of linear equations solved with the MPI-parallelized solver HIPS [69].

Dirichlet and von Neumann boundary conditions (BC) are included, the Dirichlet BC fixes the electric potential and can be use for modelling Ohmic or Schottky contacts. Von Neumann boundary conditions set the electric field in most cases to zero (except when surface charges have to be modelled) and are the default BC at the semiconductor-air interface.

The charge assignment to the mesh nodes can be either done by the cloud-in-cell (CIC) or the nearest-grid-point (NGP) formula [68].

The solver can be coupled to the nonlinear Poisson transport equation keeping the quasi Fermi level constant instead of a fixed charge. Both equations deliver the same solution but have different advantages [94]: the nonlinear Poisson equation damps artificially potential fluctuations, thus underestimating effects like a velocity overshoot [95]. Because transient phenomena are under investigation the linear Poisson has to be used. The different types of the two equations have different constrains which will be discussed in the next section.

3.7.1. Stability of the Linear Poisson Equation

A self-consistent coupling scheme for the Monte Carlo kernel and the solution of the Poisson equation can lead to instability and thus to non-physical results: the particle's and the electric field energy are increasing over time and start to oscillate. This behaviour can be avoided when the time step between two successive solutions of the Poisson equation is sufficiently small. Furthermore the maximal mesh grid spacing depends on the doping concentration.

In early works [96] the time step was chosen in a way that the plasma frequency can be resolved, following the Nyquist theorem. However, this leads in most cases to unstable simulations. A systematic investigation connecting the time step and the scattering rate was performed in [97] and later extended in [94, 98]. Furthermore the authors added constraints for the mesh grid spacing. For the linear Poisson equation the mesh grid spacing Δx has to follow:

$$\Delta x / L_\mathrm{D} < \pi \tag{3.49}$$

$$L_\mathrm{D} = \sqrt{\frac{k_\mathrm{B} T \epsilon_\mathrm{s}}{q^2 n}} \tag{3.50}$$

where L_D describes the Debye wavelength. The largest time step Δt can be expressed in terms of the plasma frequency and a scattering rate $\nu_c = \frac{q}{\mu m^*}$ formulated by Rambo [97]:

$$\Delta t < \frac{2\nu_c}{\omega_p^2} \tag{3.51}$$

$$\tag{3.52}$$

As μ describes only the low field mobility, this expression is not applicable for heated electrons experiencing a stronger scattering rate. In [94] Palestri introduced an effective scattering rate $\overline{\nu_c}$ using the momentum relaxation rate:

$$\begin{aligned} \frac{1}{\overline{\nu_c}} &= \frac{\langle E\nu_c^{-1}(E)\rangle}{\langle E\rangle} \\ &= \frac{\int_0^{E_\mathrm{max}} E\sqrt{E}e^{-E/k_\mathrm{B}T}\nu_c^{-1}\mathrm{d}E}{\int_0^{E_\mathrm{max}} E\sqrt{E}e^{-E/k_\mathrm{B}T}} \end{aligned} \tag{3.53}$$

The maximal allowed time step for different doping concentration is shown in figure 3.13 for the different expression of the scattering rate. For electron concentrations below $1 \times 10^{18}\,\mathrm{cm}^{-3}$, the constraint for the time step is unproblematic because the transient sampling of the device quantities is usually done more precisely. However, for realistic electron concentrations in modern devices the time step needs to be smaller than 1 or even 0.1 fs imposing a difficult task concerning the computational cost.

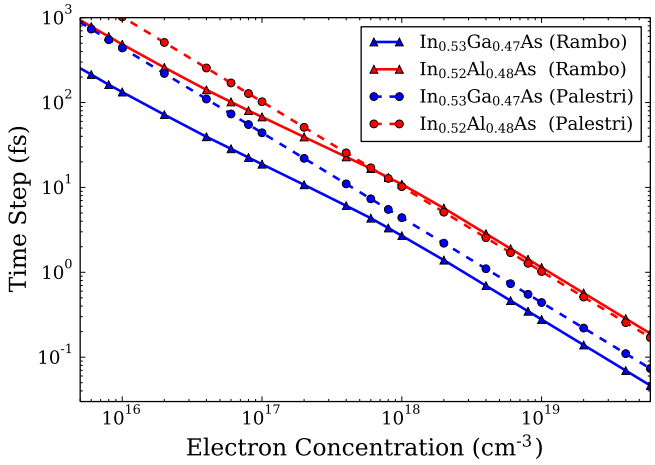

Figure 3.13.: Allowed time step for stable simulations as a function of the doping concentration for the two different material systems

The nonlinear Poisson equation provides lesser constraints but is not applicable for transient phenomena. It has to be added that simulations without a scattering mechanism are always unstable.

3.7.2. Damping of Plasma Oscillations

In [96] it is argued that the time step has to be chosen properly to damp unphysical oscillations evolving in the system. This has been discussed in [99] and this study follows [100] assuming that a particle based simulation coupled to the Poisson equation includes correctly Landau damping. No dependence for the time step or the mesh cell were observed in the outcarried simulations.

3.7.3. Short- and Long-Range Coulomb Force in MC Simulations

MC literature often refers to short- and long-range Coulomb force between carriers. In general the force between particles is given by their generated electric field and should be covered by the solution of the Poisson equation. The force experienced by a charge q_1 at position r_1 produced by a second charge q_2 at r_2 is given by the Coulomb law:

$$\mathbf{F} = \frac{q_1 q_2}{4\pi\epsilon} \frac{\mathbf{r}_1 - \mathbf{r}_2}{|\mathbf{r}_1 - \mathbf{r}_2|^3} \tag{3.54}$$

However, it has to be enforced that the field created by one particle is not acting on itself. The discretization of the simulation domain and the requirement of a zero self-force lead to the fact that particles in the same mesh cell do not experience a coulombic repulsion or attraction. After two or three mesh cells the physical behaviour is covered again by the numerical solution of the Poisson equation, termed the long-range force. To recover the short-range force in the adjacent mesh cells an additional algorithm has to be used. Typically an iteration over all carriers and the direct application of Coulomb's law is performed [100]. This process requires a large amount of simulation steps.

To minimize the computational burden we neglect the short range force and employ a small mesh spacing which should minimize the effect of an inaccurate force calculation. The influence of the mesh discretization is studied following [100]. A discretized volume (3D) inhabits two equally charged particles where one particle is kept at a constant position and the other is moving.

For different positions of the second charge the electric field is calculated for different mesh sizes. The results are shown in figure 3.14(a) for the case of point charges and a mesh spacing of 10 and 20 nm. The deviation to equation (3.54) is visible as the second charge crosses the mesh cell next to the fixed charge. The force decreases, as zero-self force is enforced. In the two-dimensional case Coulomb's law reduces to the force between to line charges, rather than point

charges. The force drops to zero when moving towards the constant charge and follows the 3D case. The effect of miscalculated short-range forces seems to be

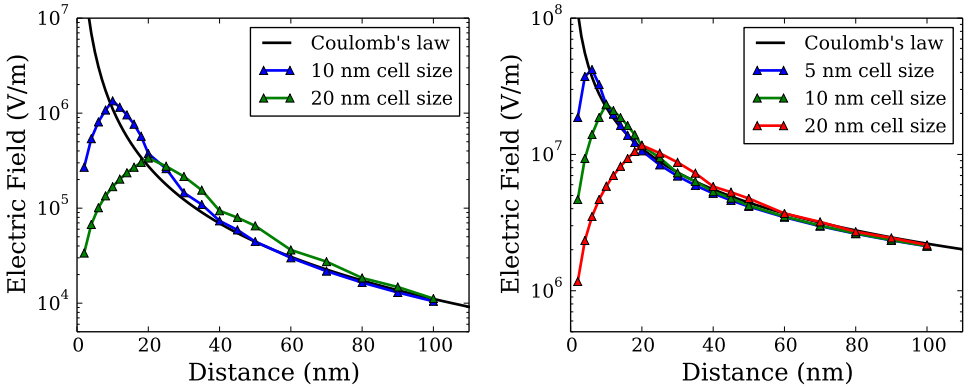

(a) 3D-case (b) 2D-case

Figure 3.14.: Electric field for the test scenario with two charges

negligible as the investigated plasma oscillations are long-range phenomena and covered by the conventional Poisson equation [96].

3.8. Pauli Exclusion Principle

As electrons are fermions they have to obey the Pauli exclusion principle (PEP) stating that only one electron can occupy a state, for each spin state, respectively. The PEP leads to the fact that even under equilibrium conditions and low temperatures high energies states are filled which would be empty in non-degenerated matter. Electrons can not lose energy under these conditions due to phonon scattering because there are no allowed transitions to lower energy states. The scattering process is suppressed, often termed Pauli blocking.

A common assumption is that for GaAs degenerated statistics have to be assumed at electron concentrations larger than $1 \times 10^{18}\,\mathrm{cm}^{-3}$. For faster materials like the used InGaAs/InAlAs material sytems it is quite unclear when the PEP has to be included. The systems have a much smaller effective mass and thus a decreased DOS (compare section 3.3.1). After a short historical review over the different methods this chapter describes the inclusion of PEP in MC simulation. Furthermore, the question when the Pauli exclusion principle gets important and what will happen to the electron distribution function is answered.

3.8.1. Historical Review

The Pauli exclusion principle was first introduced in [101] for GaAs by using a single electron MC method. The distribution function appears as a factor $1 - f$ at the right hand side of the BTE. In a single electron MC simulation, f is evaluated over the reciprocal space until a steady-state distribution is reached. It was found that degeneracy gets important at cryogenic temperatures for electron concentration of of at least 1×10^{17} and even more at $1 \times 10^{18}\,\mathrm{cm}^{-3}$. This was later extended to an ensemble MC method by Lugli and Ferry (LF) [102] simulating a vast number of particles. Unfortunately, the LF-method is not applicable to device simulations or transient simulations since at every grid point and temporal step the complete distribution needs to be evaluated imposing a computational burden which can not be solved. In [96] Fischetti and Laux suggest that the distribution function can be approximated by a Fermi-Dirac distribution where the electron temperature and the quasi Fermi level enters as arguments. Fischetti used a definition for the electron temperature $T_\mathrm{E} = \frac{2}{3k_\mathrm{B}}E$ only valid at thermodynamic equilibrium and for Maxwell-Boltzmann distribution functions. This was corrected in [103] defining the electron temperature as velocity fluctuations around a mean value. The work presented in [104] solved the system of equations in an analytical fashion neglecting second order terms due to a non-parabolicity factor $\alpha \ll 1$. For the used material this simplification is not valid. Furthermore their solution incorporates the solution of more Fermi-Dirac integrals than a direct numerical solution.

3.8.2. Model Results

This section presents the employed model in the solver, adapted from [103]. The electron temperature should approach the lattice temperature for zero applied force. Furthermore, temperature is defined as velocity fluctuations around the mean drift value:

$$T_\mathrm{E}(\mathbf{r}) = \frac{2}{3k_\mathrm{B}}\langle E\left(\mathbf{k} - \mathbf{k}_d(\mathbf{r})\right)\rangle \tag{3.55}$$

Where $\mathbf{k}_d$ is the local mean drift wave vector at position $\mathbf{r}$. The angular brackets denote the average over all particles present at that position. Following the above considerations the distribution function f is defined as:

$$f(E, \mu, T_\mathrm{E}) = \exp\left(\frac{E\left(\mathbf{k} - \mathbf{k}_d(\mathbf{r})\right) - \mu(\mathbf{r})}{k_\mathrm{B}T_\mathrm{E}(\mathbf{r})} + 1\right)^{-1} \tag{3.56}$$

Where μ is the local quasi Fermi level. The density of states relates the distribution function to the electron concentration n:

$$n(\mathbf{r}) = \int_0^\infty f(E, \mu, T_\mathrm{E})D(E)\mathrm{dE} \tag{3.57}$$

After several time steps, ensuring a good enough statistics, the average values for the position dependent electron temperature and concentration are determined by the solver and tabulated. Finally, equations (3.56) and (3.57) can be solved for the quasi Fermi level using a root finding function.

The model can answer the question when electron degeneracy becomes important and has to be considered for electrical transport phenomena. A homogeneous semiconductor was simulated at 300 K and after reaching a steady-state the quasi Fermi level was extracted. Figure 3.15 shows the location of the quasi Fermi level as a function of different electron concentrations and for different materials at thermodynamic equilibrium. Degeneracy is only considered in the Γ-valley since the density of states is much larger and the electron concentrations smaller in the higher valleys. For increasing electron concentration the quasi Fermi level

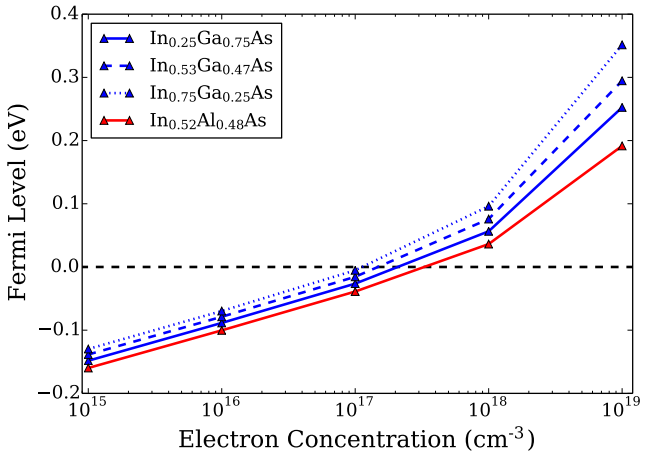

Figure 3.15.: Position of the quasi Fermi level for different materials

increases as well because more states are occupied and electrons are pushed to higher energies. The quasi Fermi level for electron concentrations slightly above $1 \times 10^{17}\,\mathrm{cm}^{-3}$ lies in the conduction band. An increased Indium mole fraction leads to faster materials as the effective mass is reduced. Consequently, a lower density of states is obtained and the available states are filled up at smaller concentrations.

The influence of Pauli blocking on the energy distribution function is visualized in figure 3.16. For $In_{0.53}Ga_{0.47}As$ a quasi Fermi level of approximately 0.08 eV results at a doping concentration of $1 \times 10^{18}\,\mathrm{cm}^{-3}$. The simulation was performed without an applied electric field which would shift the high energy tail of the distribution to higher energies [103]. The figure clearly shows that neglecting PEP would lead to completely different distribution and thus influencing transport properties. For comparison the analytical Fermi-Dirac function

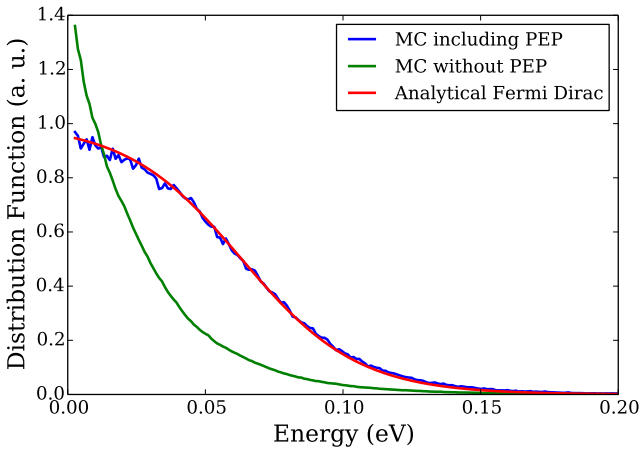

Figure 3.16.: Energy distribution function with and without degeneracy compared to the analytical Fermi-Dirac function

is plotted for a electron temperature of 300 K and the given quasi Fermi level. The results agree quite well and Pauli blocking is only considered after a scattering event, disagreeing with [105], where the authors suggest that even after every free-flight PEP has to be checked. This has led to an enormous increase in computational time in this solver without changing the results.

4. Calibration Results

The previous chapter has presented an overview of the developed MC solver. The material properties and the handling of semiconductor devices were described. In the following chapter the results of the MC program describing bulk steady-state and transient behaviour are outlined.

The most important quantity is the relationship between applied electric field and the mean electron drift velocity, namely the mobility. This will be compared to various experimental and theoretical values.

The simulation procedure is the same for all numerical experiments. An ensemble of 40000 carriers is simulated for a duration of 40 ps. After a settling time of 10 ps averages of the desired quantities are taken at an interval of 1 ps ensuring an independent statistic. The drift velocity is extracted as averages along the direction of the applied electric field. If not stated otherwise the field is applied in the [100]-direction.

4.1. Non-Degenerated Bulk Material

This section summarizes the results found for the bulk material characteristics for a doping concentration where degeneracy effects can be neglected (smaller than $1 \times 10^{16}\,\mathrm{cm}^{-3}$). The temperature and composition dependent field-velocity curves are given for InGaAs and InAlAs. In general, no quantization effects are considered in this work.

4.1.1. InGaAs

$In_xGa_{1-x}As$ is mostly used as a channel material in FETs due to its high mobility exceeding $10\,000\,\mathrm{cm}^2\,\mathrm{V}^{-1}\,\mathrm{s}$. Its low band gap makes it a suitable candidate for infrared photodiodes.

Most of the available experimental and theoretical data present in literature is for the case of an indium concentration of 53 %. The developed solver will be validated for this case. Using the simple band structure description an easy computation for different compositions or temperatures is performed.

4.1.1.1. $In_{0.53}Ga_{0.47}As$

The most common type of InGaAs is grown with an indium mole fraction of 53 % as it is lattice matched to an InP substrate and can be grown unstrained and without compensation.

Influence of the X-Valley Energy Gap

A value of approximately 0.55 eV is mostly accepted for the energetic distance of the L-valley measured from the bottom of the conduction band. However, the energy separation of the X-valley is quite unclear since large varying values are given in literature. The review of Vurgaftman [76] suggests a bowing parameter between 0.08 and 1.4 eV and recommends the latter. Since it turns out that the bowing parameter is quite strongly influencing high field transport characteristics, a systematic investigation is carried out. Figure 4.1 shows the drift-velocity vs. the applied electric field behaviour as a function of the valley offset. It is

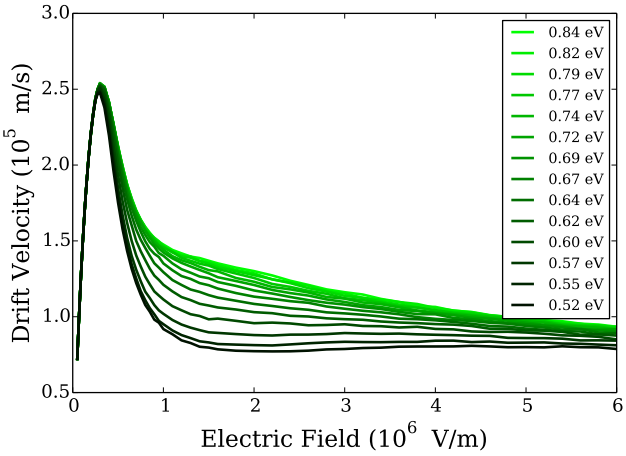

Figure 4.1.: Influence of the X-valley bowing parameter on the drift velocity vs. electric field characteristics: an increasing bowing parameter leads to a higher high field drift velocity

evident that for larger bowing parameters the high field drift velocity decreases since more electrons reside in the slower X-valley. The influence of the bowing parameter on the valley occupations is shown in figure 4.2(b) for a set of bowing parameters. It has to be noted that the bowing parameter has a much higher impact on the occupation of the higher valleys than the phonon energy and the deformation potential appearing in the scattering rates. The Γ-valley occupation seems to be nearly constant for a wide range of parameters. Additionally, carriers exhibit at smaller energies an increased intervalley scattering rate ran-

domizing momentum. This thesis uses a bowing parameter of 0.85 eV resulting in an energy offset of 0.64 eV which was from comparison with experimental values of various authors, shown in the next section. Figure 4.2(a) gives the valley

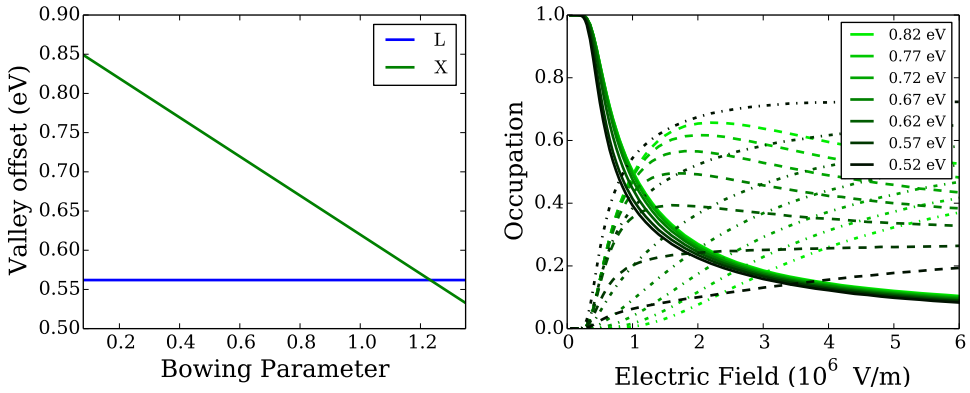

(a) Energy gap depending on the bowing parameter: for bowing parameters larger than 1.25 eV the X-valleys lies energetically below the L-valley

(b) Valley occupation for the three non-parabolic valleys (Γ: straight line, L: dashed line, X: dash-dotted line)

Figure 4.2.: Influence of the X-valley bowing parameter on the energetic distance to the bottom of the conduction band and on the valley occupation for different applied electric fields

offset, calculated using equation 3.16, as function of the bowing parameters. It is found that for bowing parameters larger than approximately 1.25 eV the X-valley lies energetically below the L-alley including the recommended value of 1.4 eV. A crossing of valleys like in InAlAs is unmotivated because the binary systems GaAs and InAs do not show such behaviour.

Drift Velocity for $x = 0.53$

Most of the present data in literature are available for an indium mole fraction of 53 %, thus the comparison with the developed solver is carried out for this mole fraction. Figure 4.3(a) shows the drift velocity as a function of the applied electric field computed using the developed solver. For comparison experimental data is taken from Haase [106] and Windhorn [107] for a low n-doping of 1×10^{15} and $1 \times 10^{14}\,\mathrm{cm}^{-3}$ which should not affect transport characteristics. In [108] time-of-flight measurements were performed with an optically excited InAlAs/InGaAs/InAlAs double heterostructure. Theoretical values derived by full band (FBMC) or nonparabolic analatical MC simulations are taken from Fischetti [87], Brennan [81] and [80]. The latter two employ a nonparabolic (analytical) band structure like used in this work.

The bulk drift velocity agrees quite well with various curves taken from literature. However, it is notable that in the low and high field region the drift velocity is slightly larger. The experimental values depend crucially on the pureness of the grown material and the measurement method. The computed velocity-field relationship should be located within the systemically made errors. However, it is noted that the MC results are mostly fitted to the few experimentally found curves and measurement errors are easily propagated. A better availability of experimental values would be favourable.

Additionally, the mean kinetic energy of carriers (figure 4.3(b)) in every valley and the valley occupation (figure 4.3(c)) in general can be determined. For electric fields below the threshold field for intervalley transfer the kinetic energy increases strongly and with the onset of intervalley scattering carriers gain less energy for an increased electric field. Figure 4.3(c) clearly shows that due to the small separation of the L- and X-valley high field transport is dominated by electrons in the X-valleys. At high fields most of the electrons are found in the X-valleys.

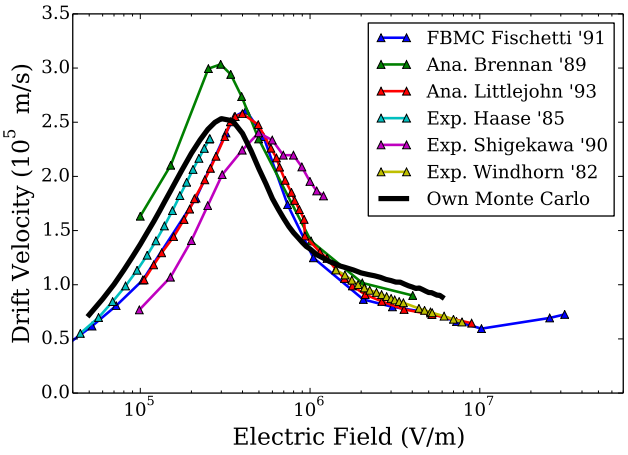

(a) Comparison of the calculated steady state drift velocity with different experimental measurements and MC simulations

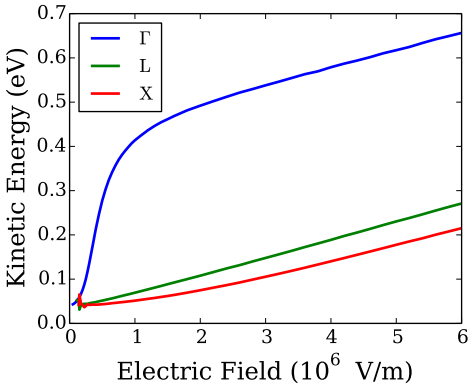

(b) Mean kinetic energy for carriers in different valleys

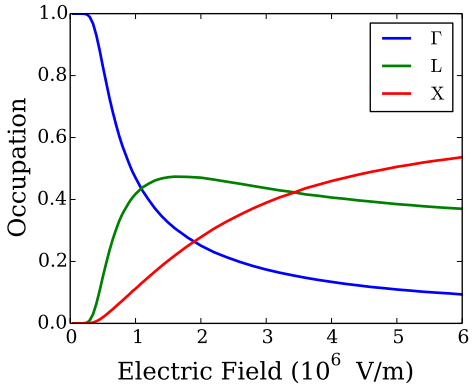

(c) Electron occupation for different valleys

Figure 4.3.: Bulk characteristics for $In_{0.53}Ga_{0.47}As$: steady state for different applied electric fields

Temperature Dependency

It is possible to investigate the electrical transport characteristic for different temperatures, which is shown in figure 4.4. For lower temperatures the number of phonons is significantly lower following Bose-Einstein statistics and thus a decreased scattering rate is obtained. A drastically increased drift velocity over the entire electric field range is observed for low lattice temperatures. The simulations were performed for different field orientations in [100]- and [111]-direction but no significant differences were found, shown in figure 4.4. In general the anisotropic effects increase at lower temperatures because scattering is reduced and carriers are aligned more effective along the applied field. The drift velocity peak shifts to smaller electric fields which is observed in measurements of GaAs and InGaAs in [106] but contrary to observations made in [109]. A different behaviour can stem from different doping concentrations or the material quality.

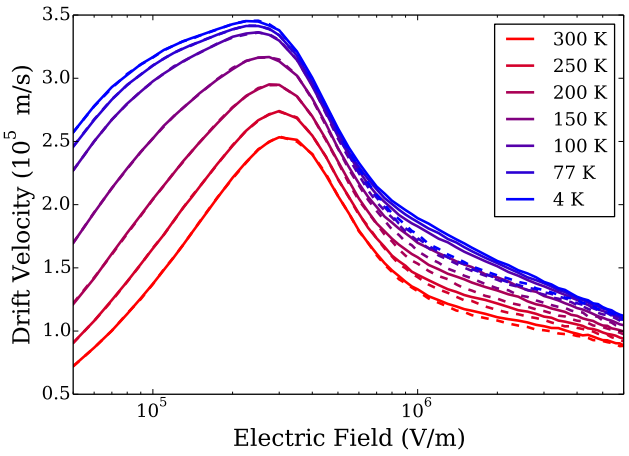

Figure 4.4.: Influence of the lattice temperature on electrical transport for different electric field strengths([100]: straight line, [111]: dashed line)

4.1.1.2. Composition Dependency: $\mathbf{In_xGa_{1-x}As}$

The maximum operating frequency of a FET is limited by the transit time [110] of electrons. For HEMTs the frequency of conventional operation can be pushed into the THz region by decreasing the gate length. Today, a gate length of 35 nm and below are reached [111, 112]. A different approach can be optimizing the channel mobility by increasing the indium content [113]. The MC simulator is able to derive the properties of InGaAs for different indium mole fractions, shown in figure 4.5. First, the mean drift velocity for different indium mole fractions

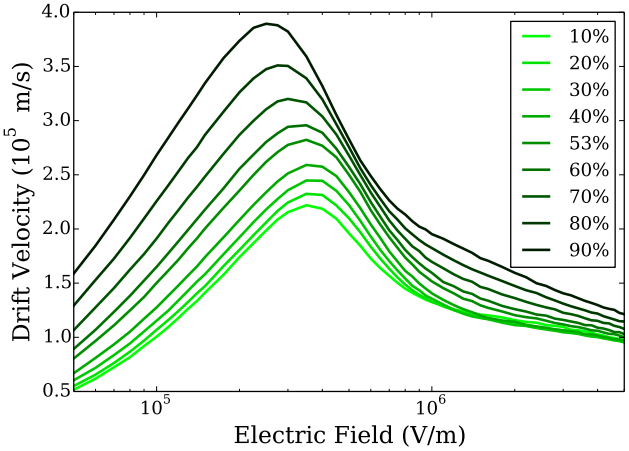

(a) Mean drift velocity for different indium mole fractions

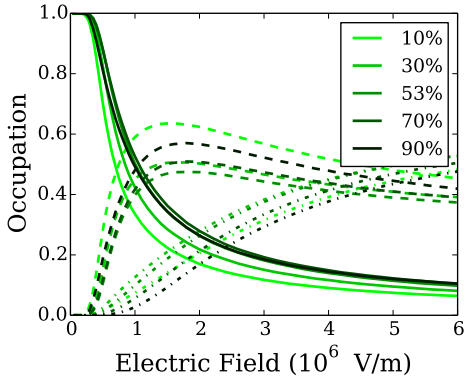

(b) Valley occupation

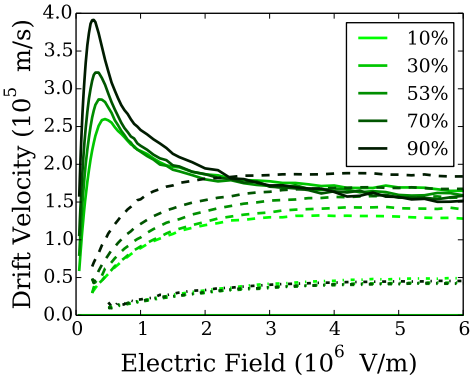

(c) Mean drift velocity for the three valleys

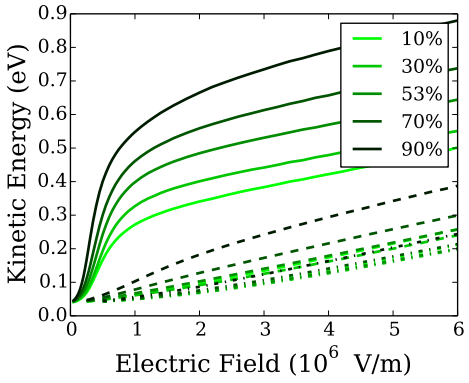

(d) Mean kinetic energy

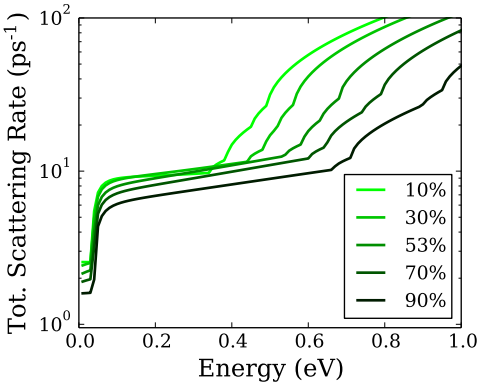

(e) Γ-valley total scattering rate

Figure 4.5.: Bulk characteristics for $In_xGa_{1-x}As$: different values for the mole fraction x are simulated and compared (Γ: straight line, L: dashed line, X: dash-dotted line)

are presented in figure 4.5(a). Almost for every electric field strength the drift velocity increases for higher indium mole fractions due to the smaller effective masses and reduced DOS given by the change in the bandstructure. This leads to a decreased scattering rate, exemplarily shown for the Γ-valley in figure 4.5(e). Furthermore, the intervalley separation increases for higher indium concentrations shifting the connected intervalley scattering rates to higher energies. The mean drift velocity can be evaluated separately for each valley, shown in figure 4.5(c). The significantly enhanced low field mobility stems from carriers in the Γ-valley. The drift velocity of carriers in the X-valley stays nearly constant. It is found that the peak velocity shifts to lower electric fields for higher indium mole fractions which is contrary to the fact that the onset of intervalley scattering starts at higher fields since more carriers stay in the Γ-valley (compare figure 4.5(b)). However, the small effective mass allows carriers gaining even at low electric fields large kinetic energies leading to the observed shift of the peak velocity which can be observed in figure 4.5(d).

4.1.2. InAlAs

InAlAs is a wide bandgap semiconductor material used in solar cells, photodiodes, bipolar and field effect transistors. The most interesting point of InAlAs is that it can be grown lattice matched to InP/$In_{0.53}Ga_{0.47}As$ for an indium mole fraction of 52 %. Together with its large bandgap it is used as a barrier materials for quantum wells. Its bulk and temperature dependent properties are given in this section.

4.1.2.1. $In_{0.52}Al_{0.48}As$

Due to its significance the bulk properties are reported for an indium mole fraction of 52 %, shown in figure 4.6. Unfortunately, Watanabe [79] gives no velocity-field calculations for comparison in their work. The only available data seems to be reported by Kim [89]. However, the presented data stems only from nonparabolic MC calculations for a doping concentration of $1 \times 10^{16}\,\mathrm{cm}^{-3}$.

The performed simulations show a bad overlap with [89] originating from the quite different parameter set, both shown in figure 4.6(a). Especially because the used models provide smaller effective masses and valley separations. Compared to $In_{0.53}Ga_{0.47}As$, $In_{0.52}Al_{0.48}As$ shows a smaller peak drift velocity due to the lower Γ-valley effective mass. However, the saturation velocity is larger which can be explained by the smaller transversal and nearly same longitudinal effective masses of the L- and X-valleys in $In_{0.53}Ga_{0.47}As$. Figure 4.6(b) and 4.6(c) give the resulting kinetic energy and the valley occupation. The kinetic energy reached by electrons is much smaller compared to $In_{0.53}Ga_{0.47}As$ resulting from the larger scattering rate and the fast onset of intervalley scattering. The

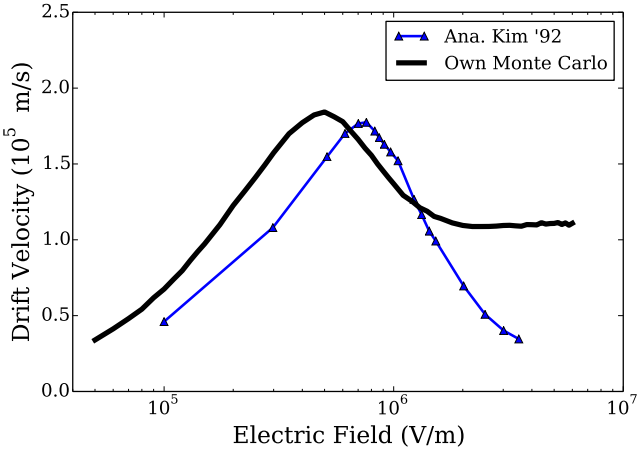

(a) Calculated drift velocity: MC simulation data taken from Kim [89] is plotted for comparison

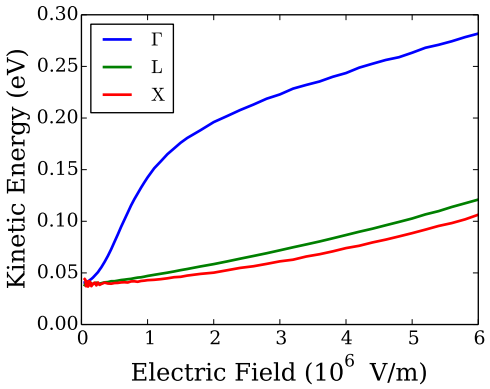

(b) Mean kinetic energy

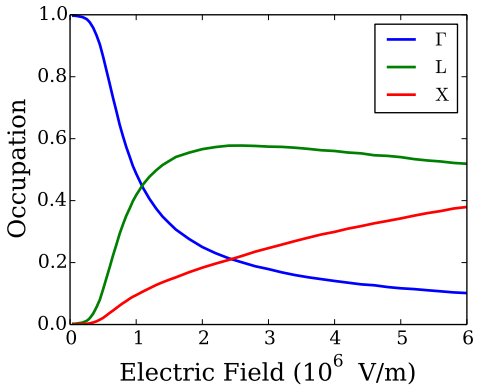

(c) Valley occupation

Figure 4.6.: Simulated bulk characteristics for $In_{0.52}Al_{0.48}As$ at 300 K

fraction of carriers in the X-valley is much smaller than in the InGaAs-case.

Temperature Dependency

Figure 4.7 shows the results for different lattice temperatures and compares them to the simulations of [89]. In contrast to $In_{0.53}Ga_{0.47}As$ the peak value stays at the same position. Below a lattice temperature of 100 K kinks appear in the velocity curves which are connected to the onset of optical phonon emission and the starting transfer to higher valleys. For InGaAs such behaviour is not observed because the optical phonon energy is lower and the valley seperation much larger. The MC simulator predicts a larger drift velocity at lower temperatures compared

to [89]. Even at 300 K the velocity-field curve shows a bad overlap. The reason lies in the already explained quite different parameter sets.

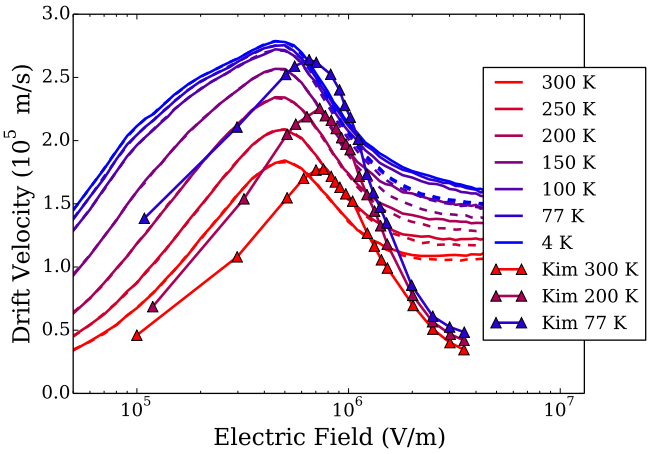

Figure 4.7.: Influence of the lattice temperature on electrical transport ([100]: straight line, [111]: dashed line)

4.2. Doped Materials

In the previous section the steady state behaviour of the InGaAs and InAlAs alloys were presented for doping concentration where considering PEP and impurity scattering is not necessary. However as outlined in section 3.8, the inclusion of Pauli blocking is mandatory. This sections shows the results for the two materials $In_{0.53}Ga_{0.47}As$ and $In_{0.52}Al_{0.48}As$ for different doping concentrations and clarifies the role of degeneracy.

Figures 4.8(a) and 4.8(b) show the obtained drift velocity vs. electric field curves for $In_{0.53}Ga_{0.47}As$ and $In_{0.52}Al_{0.48}As$, respectively. For simulations neglecting PEP, it is found that for doping concentrations exceeding $1 \times 10^{16}\,\mathrm{cm}^{-3}$ the mobility is drastically reduced. The velocity peak shifts in both cases to higher electric fields due to the higher scattering rate and the larger momentum randomization. No difference in the drift velocity for high electric fields and varying doping concentration is observed since ionized impurity scattering is not considered in these regions and is negligible.

When PEP is activated the drift velocity is increased over the entire electric field range for even small doping concentrations in $In_{0.53}Ga_{0.47}As$. For $In_{0.52}Al_{0.48}As$ only for concentrations exceeding $1 \times 10^{17}\,\mathrm{cm}^{-3}$ a difference in the drift velocity is observable. At high fields the drift velocity stays the same, with and without PEP for all doping levels. The threshold peak shift for $In_{0.53}Ga_{0.47}As$ to higher field strengths because the strong Pauli blocking seems to delay the onset of intervalley scattering. In $In_{0.52}Al_{0.48}As$ the opposite behaviour can be observed, the threshold field is reached for smaller electric fields, being consistent with the observations made in [114]. Due to PEP carriers are pushed faster to high energies and can scatter at lower fields to higher valleys. This is emphasized by figure 4.8(c) and 4.8(d) showing the total mean energy consisting of the kinetic energy of carriers and the intervalley energy offset as potential energy. For larger doping concentrations carriers have increased energy even for nearly vanishing fields.

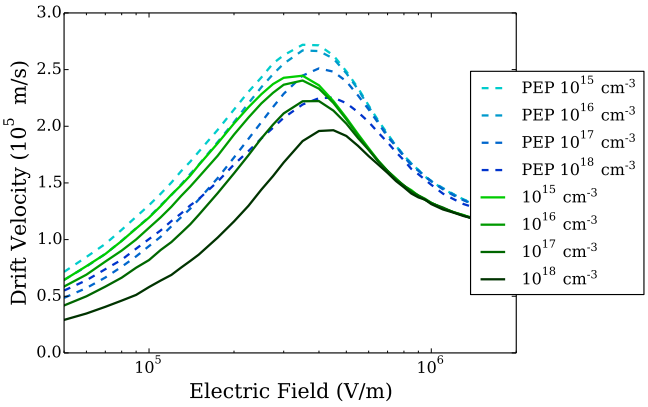

(a) Drift velocity of $In_{0.53}Ga_{0.47}As$ for different doping levels (green: without PEP, blue dashed: with PEP)

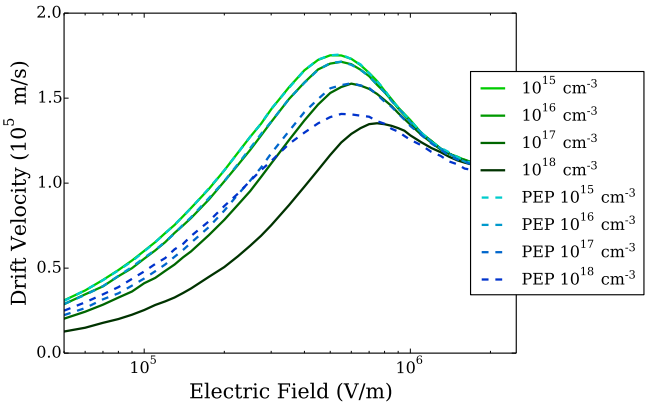

(b) Drift velocity of $In_{0.52}Al_{0.48}As$ for different doping levels (green: without PEP, blue dashed: with PEP)

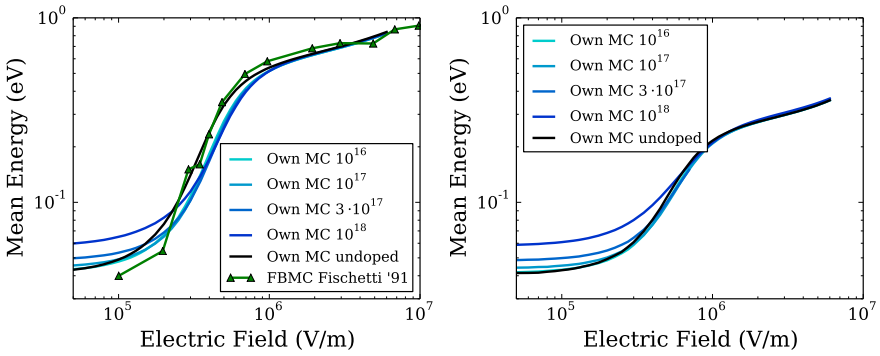

(c) Total mean energy for $In_{0.53}Ga_{0.47}As$ and different doping levels (black: own MC with PEP, blue: own MC without PEP, green: taken from [87])

(d) Total mean energy for $In_{0.52}Al_{0.48}As$ (black: own MC without PEP, blue: own MC with PEP)

Figure 4.8.: Drift velocity and total mean energy for different doping concentrations with and without Pauli blocking

Finally, these results are summarized in figure 4.9 where the low field mobility is plotted over the doping concentration. The low field mobility is averaged over the linear part of the drift velocity curve. In general, $In_{0.53}Ga_{0.47}As$ has an almost doubled mobility compared to $In_{0.52}Al_{0.48}As$ decreasing in both cases for higher doping concentrations. However, after reaching a minimum the mobility increases for even larger doping levels. This unphysical behaviour has observed in [104] and results from a relative simple screening function. Furthermore, heavy doping changes the bandstructure and leading itself to a heavier effective mass. Due to the bad knowledge of such properties this effect is neglected in the present work.

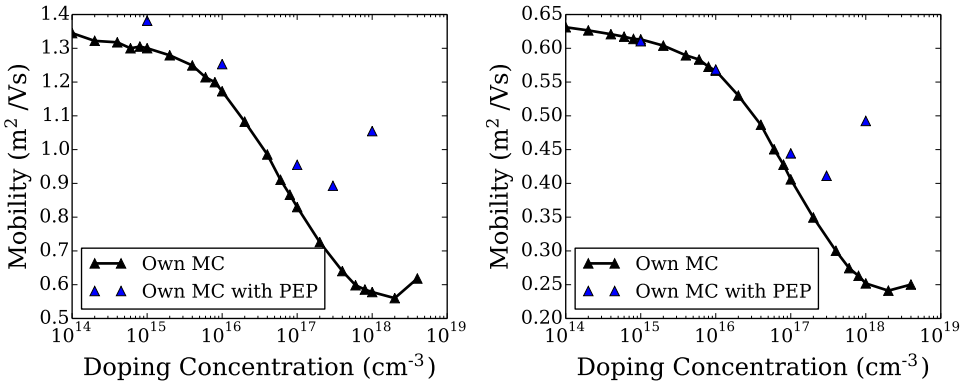

(a) $In_{0.53}Ga_{0.47}As$ (b) $In_{0.52}Al_{0.48}As$

Figure 4.9.: Low field mobility for different doping concentrations

4.3. Dynamic Response

This section covers the influence of the Pauli exclusion principle on the dynamic response of particles. Spatial and temporal velocity overshoots are a known non-local conduction phenomenon and important in short channel devices [110]. Carriers experiencing a sudden raise of the electric field strength overshoot their steady state drift velocity and need time to settle to their equilibrium values.

A carrier ensemble is simulated at zero electric field and after a settling time of 1 ps a suddenly increased electric field is applied. Figure 4.10 shows the results for the two investigated materials for low, intermediate and strong field strengths. To study the influence of Pauli blocking on the dynamics a doping concentration of $1 \times 10^{18}\,\mathrm{cm}^{-3}$ is assumed. For low electric fields ($1 \times 10^{5}\,\mathrm{V\,m}^{-1}$ no overshoot is visible and the drift velocity for the cases where PEP is considered is larger (compare section 4.2). With increasing field strength (5×10^{5} and

$1 \times 10^6\,\mathrm{V\,m^{-1}}$) overshoots can be observed, for considering and neglecting PEP respectively. However, in the PEP cases the overshoot is significantly larger since scattering mechanisms leading to equilibrium conditions are reduced. For even higher field strengths ($5 \times 10^6\,\mathrm{V\,m^{-1}}$) it is found that the influence of PEP is negligible, being consistent with the observations for the steady state mean drift velocity.

Following these observations, it is notable that degeneracy in the channel has not to be a necessary requirement for the proposed THz GUNN diodes by Mateos [41, 42]. The electric field strengths leading to the intervalley transfer in their devices is comparable to the high field case presented here ($5 \times 10^6\,\mathrm{V\,m^{-1}}$).

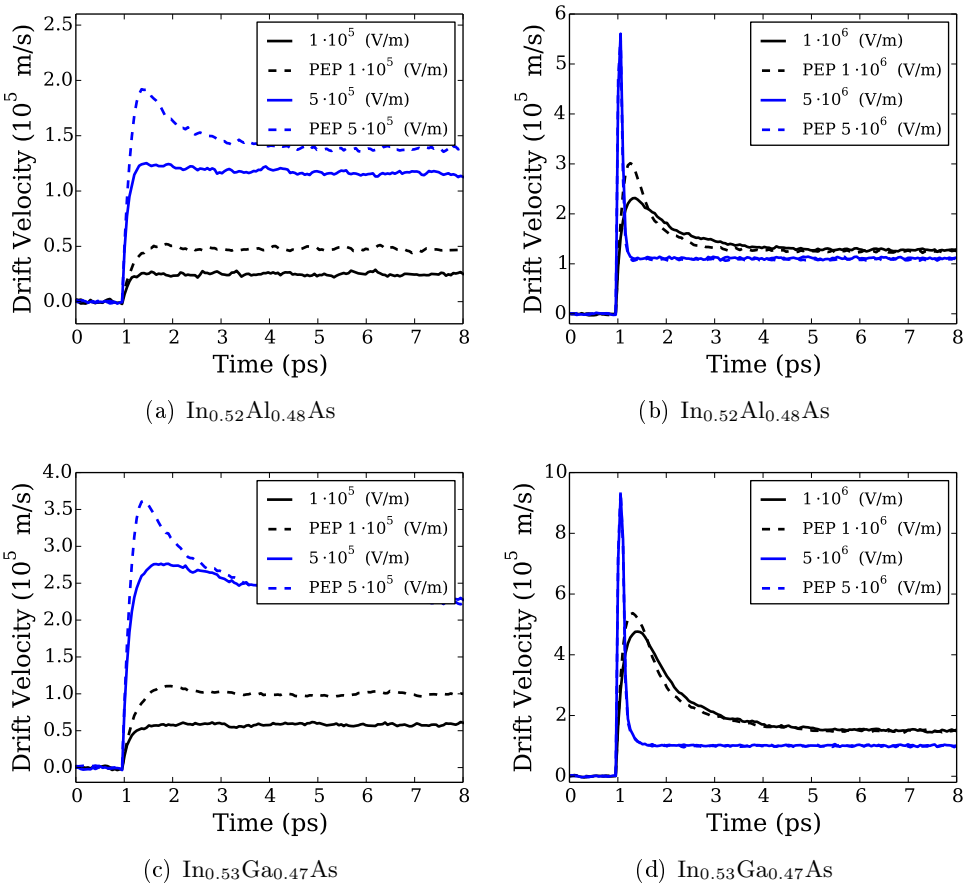

(a) $In_{0.52}Al_{0.48}As$ (b) $In_{0.52}Al_{0.48}As$

(c) $In_{0.53}Ga_{0.47}As$ (d) $In_{0.53}Ga_{0.47}As$

Figure 4.10.: Velocity overshoot for $In_{0.53}Ga_{0.47}As$ and $In_{0.52}Al_{0.48}As$ with a doping concentration of $1 \times 10^{18}\,\mathrm{cm^{-3}}$ for different applied electric fields

4.4. Device Simulation: Schottky Barrier Diode

In the previous sections the handling of material properties and their influence on the steady state and transient electrical properties has been presented. While the bulk code of the MC solver has been validated, this section presents results of the device simulation part.

A Schottky barrier diode is an ideally candidate validating calculated quantities like the electric potential, the resulting field and the conduction current. The device presented in [93] is under investigation and shown in figure 4.11. The Schottky contact, depending on its work function and the surface states of

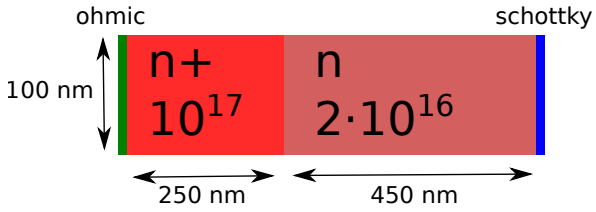

Figure 4.11.: Structure of the simulated Schottky diode

the semiconductor, forms when connected to a n-type semiconductor a depletion region. Under reverse bias the depletion region widens, making it harder for carriers to cross the contact. However, a forward bias leads to a lowering of the barrier and carriers can either overcome the barrier classically or tunnel through it. The latter is not considered in the MC simulations, nor in the analytical expression.

The current density J can be calculated analytically using the thermionic emission theory [110]:

$$J = A^* T^2 e^{-\frac{q\phi_\mathrm{B}}{k_\mathrm{B}T}} e^{\frac{qV}{k_\mathrm{B}T}} \tag{4.1}$$

$$A^* = \frac{q m^* k_\mathrm{B}^2}{2\pi^2 \hbar^3} \tag{4.2}$$

Where A^* denotes the effective Richardson constant for thermionic emission, ϕ_B gives the Schottky barrier height and V the applied voltage at the ohmic contact. The Schottky barrier height is set arbitrarily to 0.7 eV. The barrier lowering due to the presence of image charges is neglected since this is not included in the thermionic emission model.

The device is divided in mesh cells with the extension of 5 x 5 nm and the time steps were chosen to be 1 fs. After reaching a steady state distribution the calculated quantities are averaged over a duration of 5 ps. The current is evaluated by counting the particles crossing the junction. The results for the most important quantities are presented in figure 4.12.

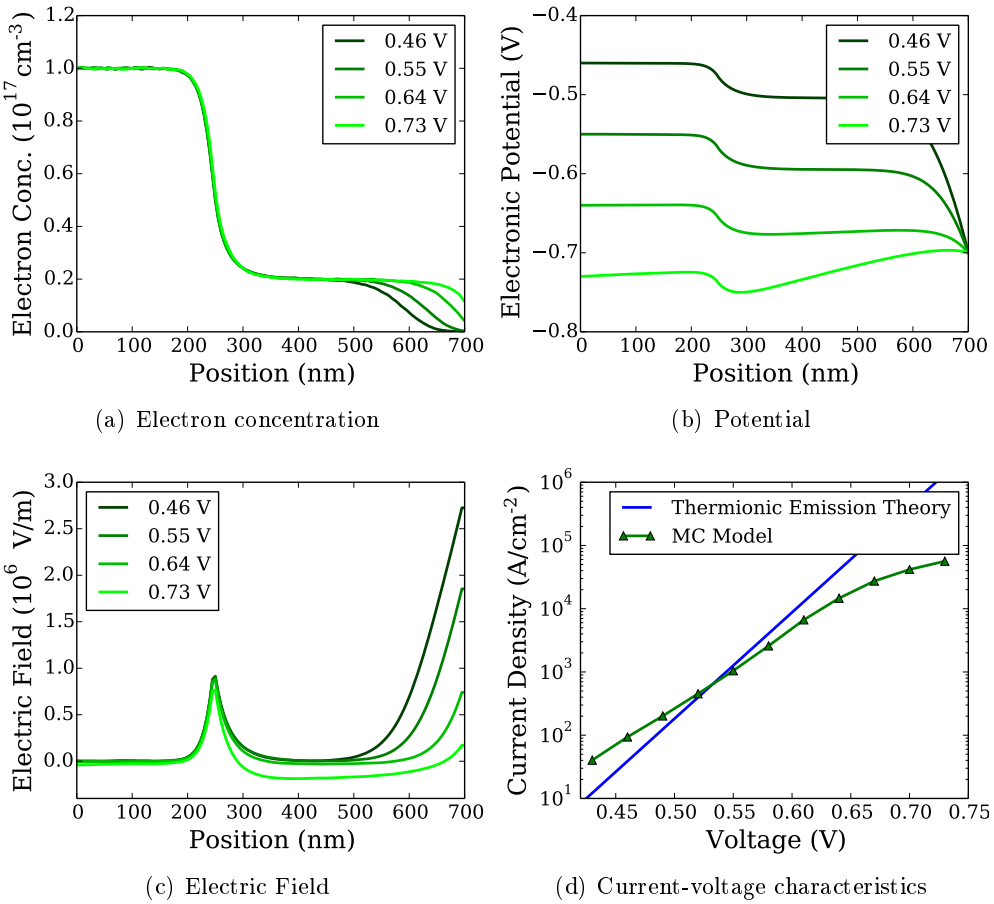

(a) Electron concentration

(b) Potential

(c) Electric Field

(d) Current-voltage characteristics

Figure 4.12.: Simulated steady state schottky barrier diode characteristics: the calculated carrier concenctration, the electric potential and the derived electric field and the IV-curve are shown

The derived electron density is shown in figure 4.12(a). Near the ohmic contact the electron concentration is kept constant at the doping level of $1 \times 10^{17}\,\mathrm{cm}^{-3}$ due to the proper injection of new carriers, leading to a zero electric field (figure 4.12(c)) and thus emphasizing the correctness of the employed model. At the schottky contact a depletion region is visible, depending on the applied bias. Elsewhere in the device the carrier concentration corresponds to the doping level. The electric potential (figure 4.12(b)) shows a decreasing barrier for anincreasing forward bias. For applied voltages larger than 0.7 V the barrier disappears. The current-voltage characteristics (figure 4.12(d) follows an exponential behaviour since the transport over the barrier is controlled via its height. However, for

vanishing barrier heights the transport across the junction is limited by the series resistance of the diode and the exponential diode characteristic changes to a linear one. The comparison with thermionic emission theory predicts a steeper current-voltage characteristics. However, the thermionic emission theory description is rather simple and the origin of the difference is unclear.

5. Plasma Oscillations in Semiconductor Devices

In chapter 3.3.1 the MC solver and included models describing material and device behaviour have been introduced. Special attention has been paid to achieve stable device simulation. The previous chapter has dealt with results obtained from bulk material simulation, giving insight into the steady state and dynamic response of the used semiconductors on applied electric fields.

This chapter starts with noise results covering the simulation of bulk material. The second part presents the dynamic behaviour of gated and ungated simplified FET-structures introduced within the analytic hydrodynamic models in section 2.2.2. The influence of different parameters like the device geometries and the strength of the plasma oscillation with respect to the lattice temperature and in presence of a current flow was studied in detail.

The dispersion of plasma waves in such simplified structures were studied for the ungated case in [115–117] and for the gated structure in [118]. The main differences between this work and these publications is discussed where appropriate. It has to be noted that in this work the term dispersion relation is referring to the connection of the plasma frequency to the geometry of the investigated devices.

In the following studies the power spectral density (PSD) of voltage and current oscillations were calculated using the autocorrelation function and the Wiener-Khinchin theorem, introduced in the next section. The simulations were performed, if not stated otherwise, at a lattice temperature of 15 K. As the noise level of the electron concentration and velocity depends critically on the number of simulated particles, typically 300 particles were present in each cell.

5.1. 3D Plasma Frequency

In doped semiconductors, or in more general terms systems with free charges, current oscillations can develop at the plasma frequency. For crystalline solid state systems like metals and semiconductors the plasma frequency is given by [119]:

$$f_p = \frac{1}{2\pi}\sqrt{\frac{e^2 n}{\epsilon m^*}} \tag{5.1}$$

With increasing electron concentration n a larger plasma frequency is observed. Equation 5.1 can be derived using the Drude model and the free electron model [67]. At the plasma frequency the dielectric function vanishes and oscillations can appear in the electron gas, even without an external excitation. For metals the plasma frequency is located in the optical or ultra-violet region, for doped semiconductors the plasma frequency can be found in the THz range. The plasma frequency can be observed experimentally for instance shown in [120] where a pin-diode has been illuminated with a fs-laser. Depending on the optically generated carrier density, THz-radiation was observed with a peak value at the plasma frequency. In MC simulations the plasma frequency appears as peaks in the noise spectra [121].

Before simulating complex device geometries the solver has been validated for the simple case of a semiconductor slab with a length of 1 µm and ohmic contacts at each side. A 1-dimensional simulation was performed with a mesh size of 5 nm and a time step of 5 fs. The simulations were carried out for doping concentrations of 1×10^{16}, 1×10^{17} and $1 \times 10^{18}\,\mathrm{cm}^{-3}$ and last for 100 ps. No electric excitation was applied, the contacts have the same electric potential.

For calculating the fluctuation spectrum this work uses the Wiener-Khinchin theorem which states that the power spectral density can be computed using the Fourier transform of the autocorrelation of the signal [122, 123]:

$$C_k = \sum_n \delta U_n \delta U_{n+k} \tag{5.2}$$

$$\delta U_n = U_n - \overline{U} \tag{5.3}$$

Where C_k gives the correlation value for the function U_n with itself at a time shift k. n denotes the length of the autocorrelation signal and the mean value $\overline{U}$ is subtracted from U_n. The autocorrelation function can be used to detect periodicity in noisy signals. The function has always its maximum at $k = 0$ since the multiplied functions are identical. When no periodic signal elements are encountered, the autocorrelation function shows a fast decaying behaviour. Otherwise the autocorrelation function shows an oscillatory behaviour. However, in this thesis the autocorrelation function is only used in the frame of the Wiener-Khinchin theorem for finding the power spectral density.

Figure 5.1 shows the electric potential at the center of the semiconductor slab for different doping concentrations and the corresponding autocorrelation function. Following equation (5.1) it is obvious that a higher doping concentration leads to oscillations at higher frequencies. Furthermore the fluctuation amplitude is larger for increased doping concentrations since larger electric fields are induced. The autocorrelation functions show basically the same behaviour.

By taking the Fourier transform of the autocorrelation function, shown in figure 5.1(b), the power spectral density of voltage fluctuation can be derived

and is presented in figure 5.2(a). It is emphasized that this thesis uses the units of the Fourier transform rather than the units of its discrete version. The spectral analysis shows peaks in the noise spectrum located around the analytical value of the plasma frequency which is shown for comparison in figure 5.2(b). The plasma frequency and its full width at half maximum (FWHM) presented by the errorbars are obtained by fitting a Gauss curve to the spectral density function. The electric fields being present in the structure range from 1×10^4 to $1 \times 10^6\,\mathrm{V\,m^{-1}}$ depending on the doping concentration. However, averaged over time the electric field has to converge to zero. In conclusion, the MC solver is able to resolve fluctuations in the steady state and the presented method will be used throughout this thesis.

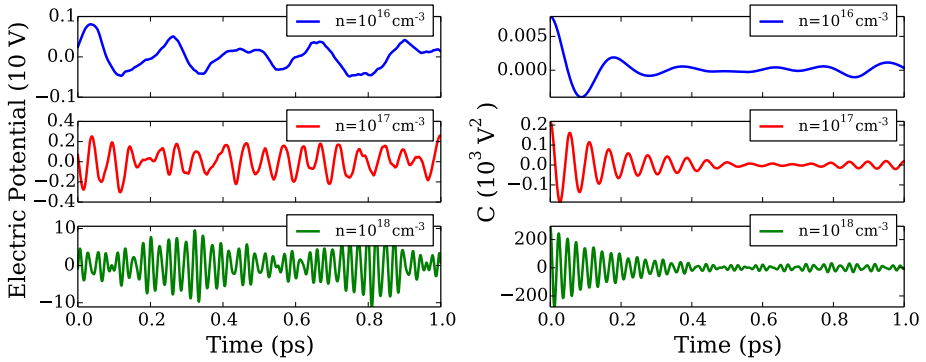

(a) Electric potential (b) Autocorrelation function

Figure 5.1.: Electric potential fluctuations and their autocorrelation function

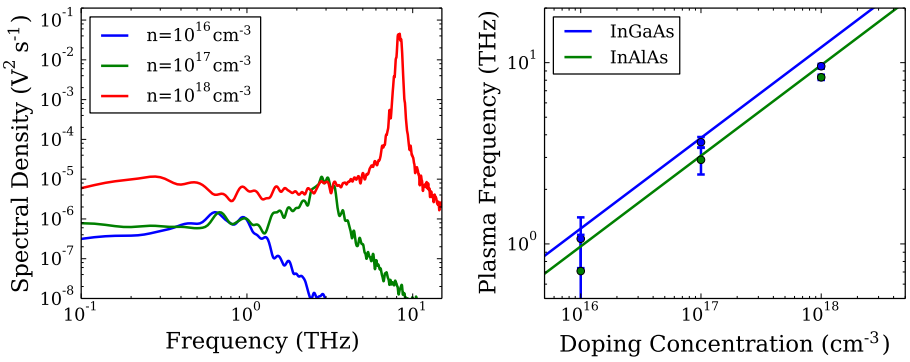

(a) Power spectral density (b) Comparison with equation 5.1

Figure 5.2.: Power spectral density and a comparison with analytical theory

5.2. Transition to a 2D Plasma Frequency

The last section has revealed that in semiconductor bulk material fluctuations appear at the plasma frequency in the power spectral density. By surrounding a bulk material with a dielectric, which can be an undoped semiconductor, and by shrinking the width of the resulting channel a transition to a 2-dimensional plasma frequency can be observed. Fixing the electric potential on the top side of the structure, a simplified gated FET is derived. These two structures correspond to the simplified models used in the hydrodynamic framework presented in section 2.2.2, namely the ungated and gated case (compare figure 5.4). This section shows the transition to a 2-dimensional plasma frequency and discusses numerical issues observed in MC simulations.

Figure 5.4 reports the simulation results for decreasing channel widths w for the ungated and gated structures. The source and drain potentials have been set to an equal potential $U_\mathrm{S} = U_\mathrm{D} = 0\,\mathrm{V}$. In the gated structure the depleting mechanism of the gate contact was not considered and set to $U_\mathrm{G} = 0\,\mathrm{V}$ as well. The simulations were performed for a channel length of 100 nm for both structures at a channel doping concentration of $1 \times 10^{18}\,\mathrm{cm}^{-3}$. The simulation for a concentration of $1 \times 10^{17}\,\mathrm{cm}^{-3}$ for the ungated case was performed for a slightly longer channel with 200 nm. These small values were chosen for a large variation of the plasma frequency. For all simulations the surrounding dielectric layer was formed by $In_{0.52}Al_{0.48}As$ and the channel by $In_{0.53}Ga_{0.47}As$. The 2-

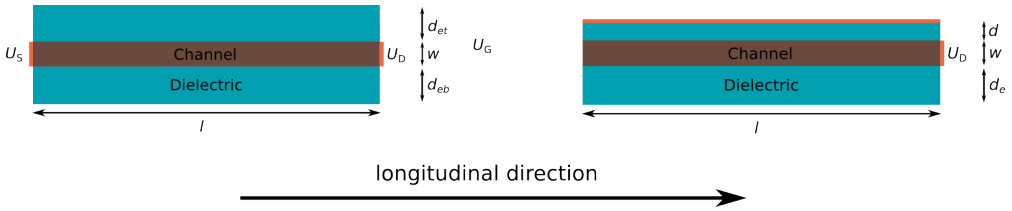

Figure 5.3.: Schematic of the simulated structures (left: ungated, right: gated channel)

dimensional electron concentration entering equation (2.7) and (2.8) was derived using $n_\mathrm{2D} = n_\mathrm{3D} w$. In all simulation no 2D plasma frequency values above the 3D plasma frequency were observed. For a thinner channel (a smaller 2D electron concentration), the plasma frequency decreases as expected. The wavevector entering the 2D dispersion relations was chosen as $k = \frac{\pi}{l}$, corresponding to a half-wavelength standing wave pattern. This consideration is justified later when the mode profiles are discussed in section 5.5.

Millithaler observed in MC simulations the same behaviour for ungated structures [117]. However, a more detailed analytical description is given by Marinchio in [124] for the gated case. The authors changed the gradual channel approx-

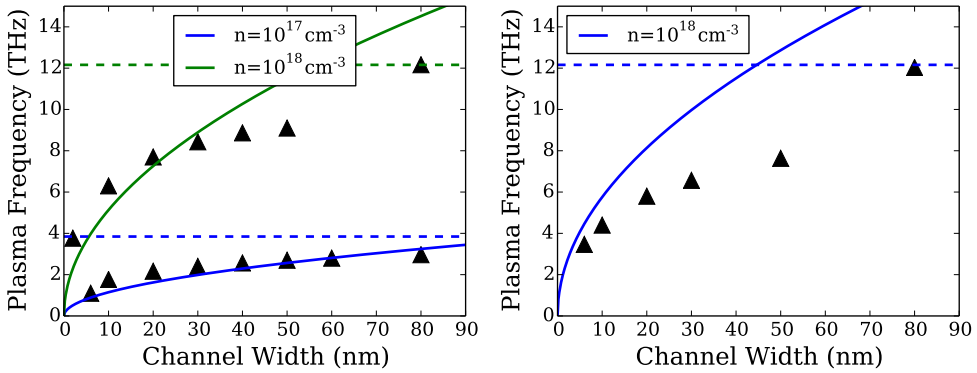

(a) Calculated plasma frequencies for different channel thicknesses in an ungated structure

(b) Calculated plasma frequencies for different channel thicknesses in a gated structure

Figure 5.4.: Monte Carlo simulation results (symbols) of the 2D plasma frequency: The width of the surrounding dielectric layer is varied. The 2D-value converges to the bulk value for thicker surrounding layers (solid line: 2D frequency using equation 2.7 and 2.8, dashed line: analytical 3D plasma frequency).

imation made in [29] with a solution of the Poisson equation, accounting for the longitudinal electric field variations neglected otherwise. They found that by considering the longitudinal and transversal fields, two limits can be distinguished: for a channel thickness which is small compared to the wavelength the real 2D case described in [29] is valid. In the opposite case, for a large channel the behaviour is equal to the 3D plasma frequency. However, in the intermediate regime the fundamental and higher modes are present. It has to be emphasized that the transition to the 2D case is only caused by shrinking the channel width, since no 2D effective masses are incorporated into the solver.

5.3. Numerical Issues: Influence of the Simulation Geometry

In modern semiconductor devices the substrate and a following buffer layer cover the most physical space. However, it is beneficial in terms of computational time to exclude these regions. Especially the solution of the Poisson equation is a tedious task and thus it is desirable to keep the simulation domain as small as possible. As the imposed boundary conditions alter the device operation [125] it is necessary to study different scenarios and the impact of the observed plasma frequency.

The study was performed for the ungated and gated structure for a fixed doping concentration of $1 \times 10^{18}\,\mathrm{cm}^{-3}$. First of all the simulation results for the ungated structure for different thicknesses of the surrounding dielectric layers ($d_{\mathrm{eb}} = d_{\mathrm{et}}$) are shown in figure 5.5(a) and 5.5(b). Both investigated channel widths (5 and 20 nm) show the same development of the plasma frequency: an increasing thickness of the dielectric layer leads to a lower plasma frequency until a saturation can be observed. Shorter channels seem to reach this saturation for thinner barriers. It is notable that only for a thick enough surrounding layers a clear dispersion is visible. For vanishing dielectric layers the dispersion disappears, confirming that the dispersion of the plasma frequencies is a two-dimensional effect.

Additionally, simulations were performed for a fixed thickness of the bottom dielectric layer $d_{\mathrm{eb}} = 160\,\mathrm{nm}$ and a varying thickness of the upper layer d_{et}. The results for this asymmetrical case, shown in figure 5.5(c), are leading to the assumption that only one dielectric layer needs to be thick enough and the second layer is not influencing the dielectric function. At last simulations were carried out for a gated structure for a fixed gate to channel distance of $d = 20\,\mathrm{nm}$, shown in figure 5.5(d). The simulations show that the plasma resonance does not shift for different thicknesses of the dielectric layer. A fixed potential by the Schottky gate contact seems to dominate the system's response and suppresses the influence of dielectric layer boundary (electric field is set to zero). This follows the previous case where one boundary seems to be sufficient.

In conclusion for further device simulation, especially when ungated and gated regions are combinated as in real structures, it follows that the simulation geometry is given by the ungated part of the transistor. The lower dielectric barrier should be thick enough, the top layer and the geometry of the gated part are not influencing the resonant plasma frequency.

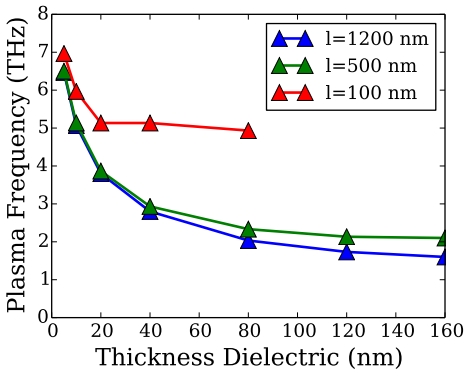

(a) Ungated channel: The thickness of the lower and upper layer ($d_{\mathrm{eb}} = d_{\mathrm{et}}$) was varied in the same manner for a channel width of $w = 5\,\mathrm{nm}$

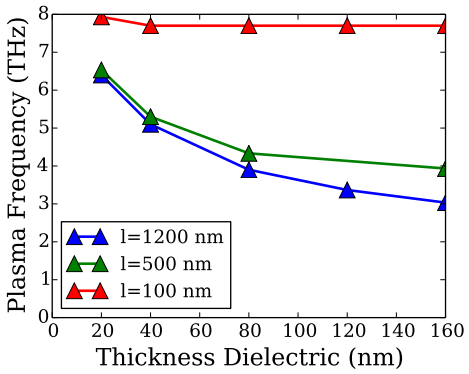

(b) Ungated channel: Sames as left figure but for a thicker channel ($w = 20\,\mathrm{nm}$)

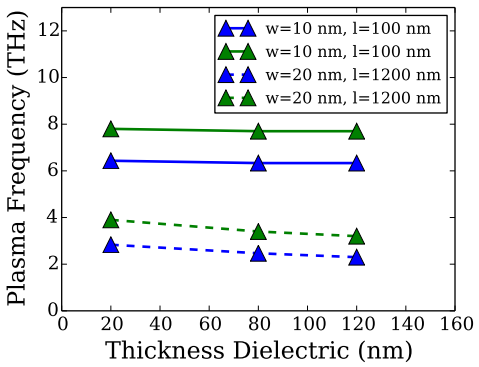

(c) Ungated channel: The thickness of the lower dielectric layer was chosen not to influence the results (varying d_{et})

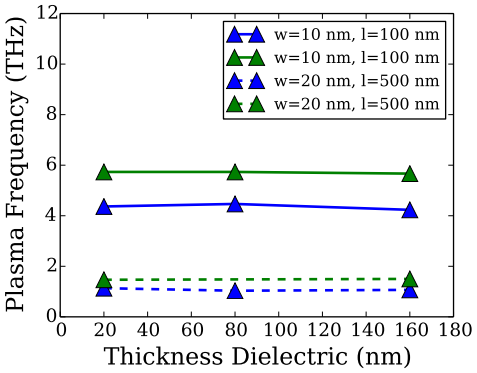

(d) Gated channel: Varying d_{e}

Figure 5.5.: Monte Carlo simulation results (symbols) of the 2D plasma frequency: The width of the surrounding dielectric layer is varied. The 2D-value saturates for thicker surrounding layers.

5.4. Dispersion in Ungated and Gated Structures

The previous section has covered the influence of the simulation geometry on the plasma peak. In this section the dispersive properties of the structure will be investigated. The wave vector in equation 2.7 and 2.8 is given by the channel length. Thus, the plasma frequency should change with the channel length.

The simulation results for the ungated and gated structure are shown in figure 5.6, 5.7(a) and 5.7(b) for different doping concentrations, respectively. The bulk plasma frequency is plotted in dashed lines and the analytical formulation in solid lines for comparison. For all carrier concentrations an increasing plasma frequency for decreasing channel lengths is observed, following the expectation of the dispersion relation. For thicker channels a larger 2D carrier concentration results and hence higher plasma resonances are reached. However, the analytical expressions predict higher plasma frequencies than observed in the MC simulations. Equation (2.7) and (2.8) are relying on *real* 2D concentrations which is not implementable in devices or numerical simulations. Additionally, the gate to channel distance of the gated structure can be varied as shown in figure 5.7(c). A larger seperation leads to an increased frequency, following the prediction of equation (2.8).

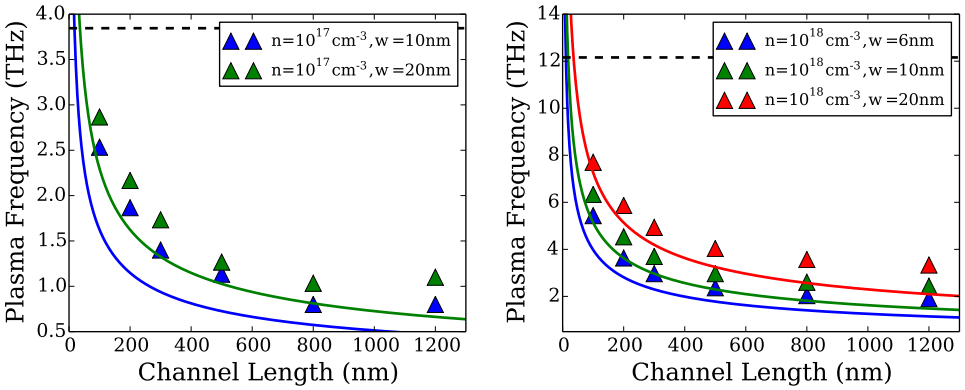

(a) Ungated channel for a doping concentration of $1 \times 10^{17}\,\mathrm{cm}^{-3}$

(b) Ungated channel for a doping concentration of $1 \times 10^{18}\,\mathrm{cm}^{-3}$

Figure 5.6.: Extracted plasma frequencies using MC simulations for the ungated channel having different lengths (symbols: MC results, solid lines: analytical 2D values)

The tuneability of the plasma frequency is often seen as an advantage of the gated structure over the ungated one. For larger gate voltages the electrons are depleted in the channel leading to a lower plasma frequency, presented in figure 5.7(d).

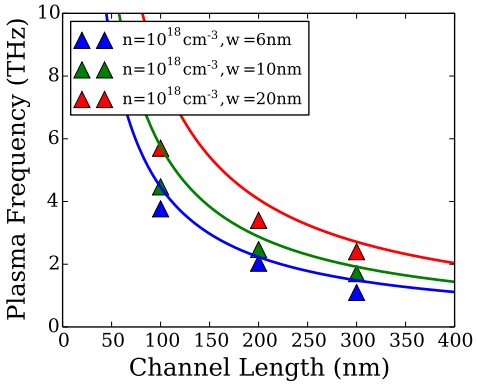

(a) Plasma frequency of the gated structure for a doping concentration of $1 \times 10^{18}\,\mathrm{cm}^{-3}$

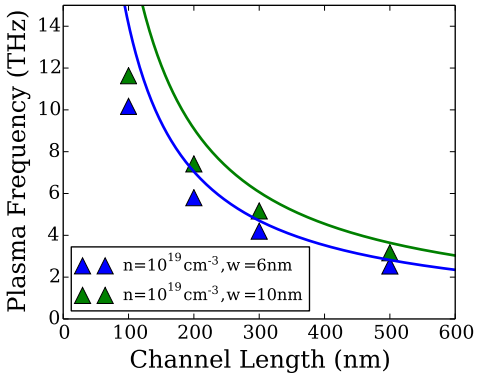

(b) Plasma frequency of the gated structure for a doping concentration of $1 \times 10^{19}\,\mathrm{cm}^{-3}$

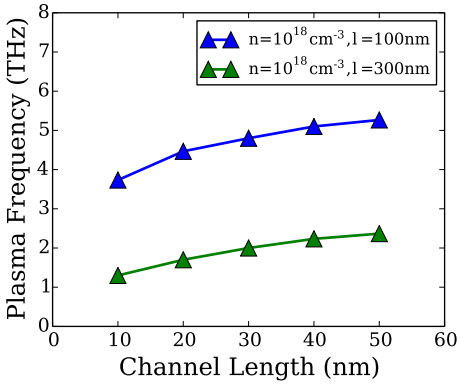

(c) Varying gate to channel distance d for two different channel lengths

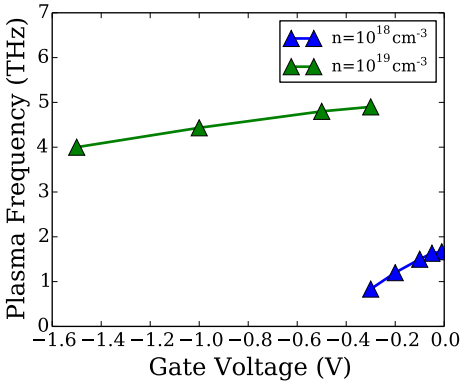

(d) Plasma frequency as a function of the gate voltage: Applied bias depletes the electron concentration and lowers the plasma frequency

Figure 5.7.: Dispersion relation for the gated channel for different channel lengths, doping concentrations and gate voltages: Symbols are referring to simulation results and solid lines to analytical values.

The two simplified structures have been examined for different channel concentrations and lengths. It was found that the plasma frequency dispersion follows the expectations of the analytical expressions.

5.5. Mode Profiles in the Channel

The dispersion of plasma waves in the conducting channel was discussed in the previous section. In comparisons with the analytical theory a wave vector corresponding to a $\lambda/2$ standing wave pattern for the fundamental mode was assumed. This assumption will be justified in this section by investigating the longitudinal mode profiles in the channel.

The two different structures are investigated for different channel lengths and thicknesses. At every position along the channel the electric potential fluctuations were investigated by applying the Wiener-Khinchin theorem. The calculated noise spectra can be plotted and the longitudinal mode pattern analyzed. For a better visualization of the higher modes, the electric potential mode profiles are plotted logarithmically.

First, simulations were performed for a fixed channel width of $w = 10\,\mathrm{nm}$ and different channel lengths with a doping concentration of $1 \times 10^{18}\,\mathrm{cm}^{-3}$ for the ungated and gated case, respectively. The results are shown in figure 5.8. For all cases the fundamental mode is the dominant mode and shows the highest amplitude, forming a $\lambda/2$ standing wave due to the imposed boundary conditions (fixed potential at the contacts). A decreasing channel length leads to a lower plasma frequency, which was already discussed in the last section. Furthermore, the number of longitudinal modes increases for larger channel lengths accompanied by a smaller mode spacing. The standing wave pattern of plasma modes seems to be comparable to the situation in a Fabry-Perot cavity. The oscillation strength of the higher modes decreases rapidly. As stated in [124], no plasma wave excitation is found above the bulk plasma frequency. Thus, only a limited number of modes can be excited, given by the mode spacing and the frequency of the fundamental mode.

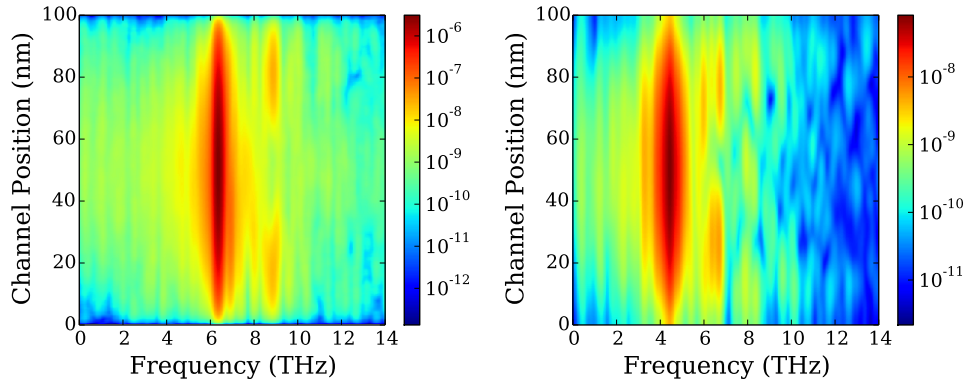

(a) Ungated channel: $l = 100\,\mathrm{nm}$ (b) Gated channel: $l = 100\,\mathrm{nm}$

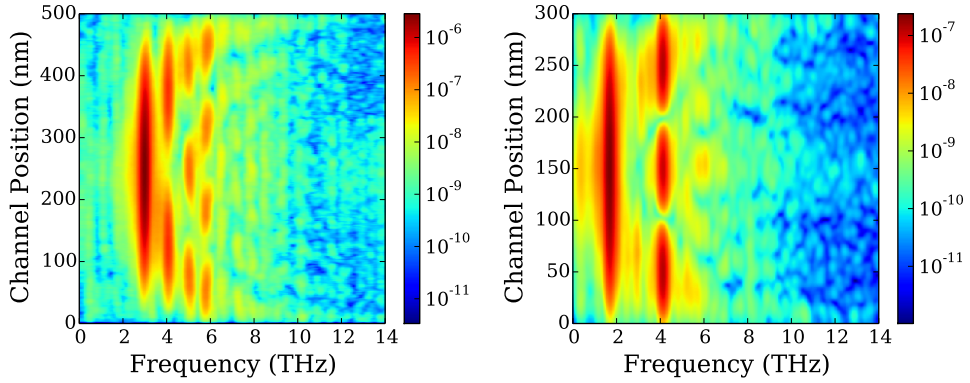

(c) Ungated channel: $l = 500\,\mathrm{nm}$ (d) Gated channel: $l = 300\,\mathrm{nm}$

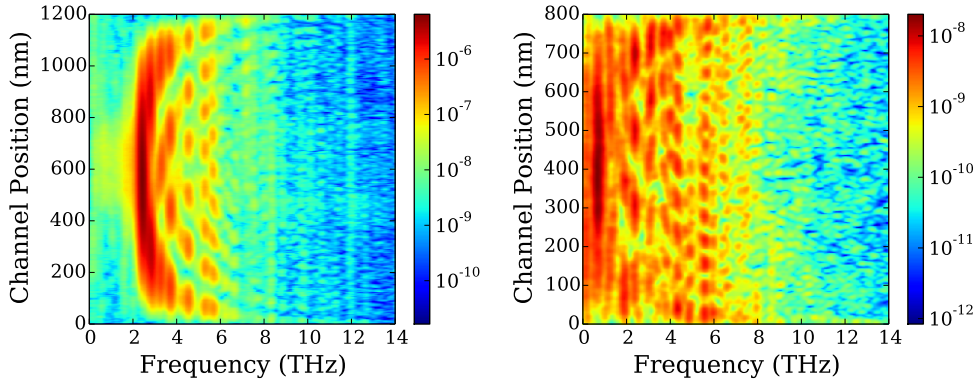

(e) Ungated channel: $l = 1200\,\mathrm{nm}$ (f) Gated channel: $l = 800\,\mathrm{nm}$

Figure 5.8.: Voltage fluctuation amplitude (red: high amplitudes, blue: low amplitudes) along the channel for ungated and gated structures at different channel lengths l for a channel thickness of $w = 10\,\mathrm{nm}$ and a doping concentration of $1 \times 10^{18}\,\mathrm{cm}^{-3}$

Marinchio predicted in [124] that for the gated case with asymmetrical boundary conditions a broader channel would lead to excitations of higher modes until the resonance converges to the bulk mode. Figures 5.4(a) and 5.4(b) already show that a broader channel leads to higher plasma frequencies, given by the increasing 2D carrier concentration. Additionally, the connected mode patterns are shown in figure 5.9. For a moderate channel thickness of 30 nm the excitation of numerous higher modes compared to the 10 nm-case in figure 5.8 is visible, following the predictions in [124] and the observations made in this study for different channel lengths. However, a further increment of the channel thickness does not lead to the excitation of more plasma modes. Obviously, the higher order modes seem to gain more significance by suppressing the lower ones.

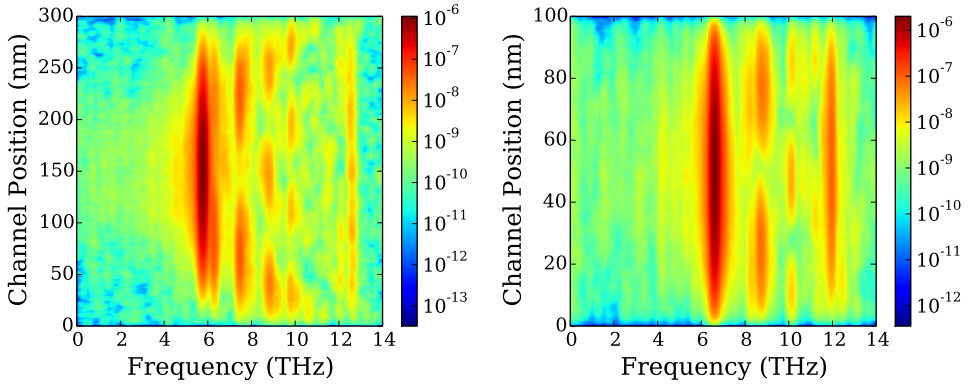

(a) Ungated: $l = 300\,\text{nm}$, $w = 30\,\text{nm}$

(b) Gated: $l = 100\,\text{nm}$, $w = 30\,\text{nm}$

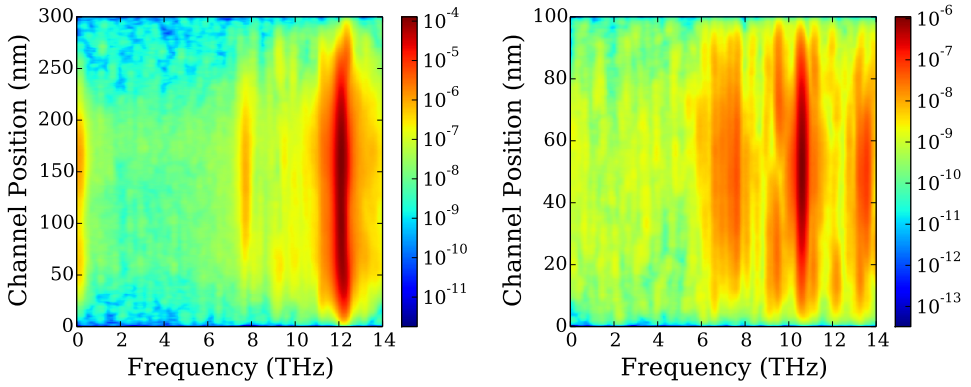

(c) Ungated: $l = 300\,\text{nm}$, $w = 80\,\text{nm}$

(d) Gated: $l = 100\,\text{nm}$, $w = 50\,\text{nm}$

Figure 5.9.: Voltage fluctuation amplitude (red: high amplitudes, blue: low amplitudes) along the longitudinal channel direction for ungated and gated structures at different channel thicknesses.

Millithaler is arguing in [117] that the crossover between 2D and 3D plasma frequencies is at the Debye wavelength. No similar significant observations could be made. Furthermore, [118] shows for the gated case always a peak at the 3D plasma frequency. It is noted that this peak is only observed in our simulations for time steps exceeding the stability criteria between the solutions of the Poisson equation. At smaller time steps this peak vanishes or its amplitude is located several orders of magnitude below the 2D peaks.

The fluctuations of the electric potential drive the electric field and produce a current in the channel. Figures 5.10 and 5.11 show the simulated mode profiles for the current density fluctuations for an ungated and a gated structure with a channel length of $l = 500\,\mathrm{nm}$ and $l = 300\,\mathrm{nm}$, respectively. At frequencies in the THz range, the displacement current $\frac{\partial \mathbf{D}}{\partial t}$ is significantly contributing to the overall current density and has to be evaluated. It is found, that in the ungated and gated structures the current mode profile is equal for the conduction and displacement current. The current density oscillation amplitudes are in the same order of magnitude for both current types.

In the investigated structures the current modes are visible at the resonant frequencies. For the ungated case the current density forms nodes at the device borders and shows for the fundamental mode two oscillation maxima, four maxima for the second mode and $2m$ for the mth mode.

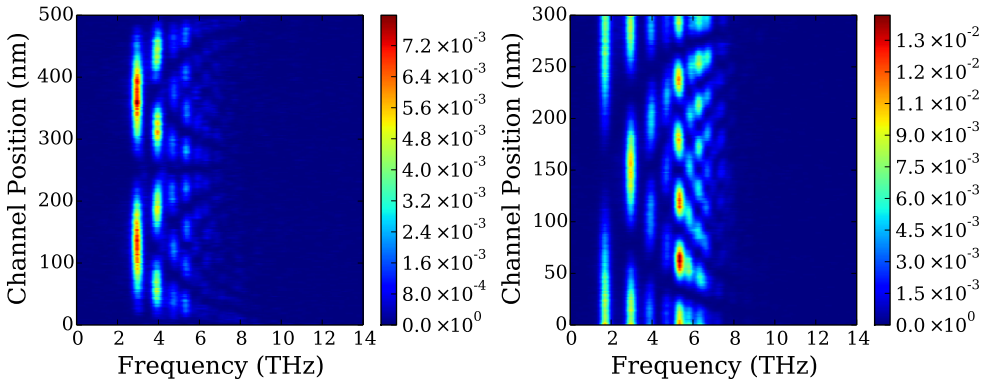

(a) Ungated channel having a length of $l = 500\,\mathrm{nm}$

(b) Gated channel having a length of $l = 300\,\mathrm{nm}$

Figure 5.10.: Calculated conduction current (red: high current, blue: low current) for an ungated and a gated structure: The simulations have been performed at a lattice temperature of 15 K.

In contrast to the current density in the ungated structure and the electric potential profiles where the fluctuation amplitude drops to zero, the current density in the gated structure shows quite a different behaviour. At the channel contacts

the current density forms peaks for the fundamental mode and decreases into the channel. Basically the higher modes show a similar profile with an increasing number of appearing maxima. Marinchio presented in [126] a comprehensive analytical study about THz plasma waves in a gated semiconductor slab of arbitrary thickness. It is noted that for the case of symmetric boundary conditions the presented mode profiles coincide with the profiles in Marinchio's analytical study.

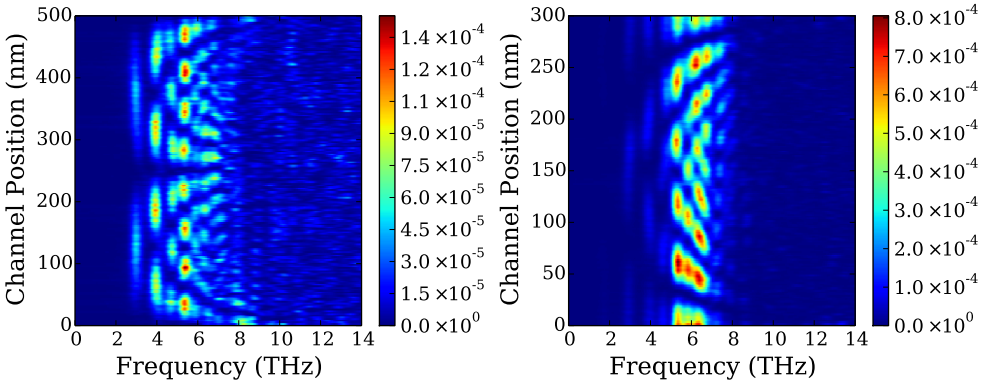

(a) Ungated channel with a length of $l = 500\,\mathrm{nm}$

(b) Gated channel with a length of $l = 500\,\mathrm{nm}$

Figure 5.11.: Calculated displacement current (red: high current, blue: low current) for an ungated and a gated structure: The simulations have been carried out at a lattice temperature of 15 K.

This section has summarized the investigations of the current density and electric potential mode profiles for different geometries. Different channel lengths and thicknesses have been investigated, showing the presence of higher plasma modes. As the channel thickness increases, the 2D modes converge to the 3D bulk frequency. Both quantities are forming standing wave patterns in the channel.

5.6. Oscillation Strength

While the modal profiles were studied in the previous section, this section covers the voltage and current density oscillation amplitudes. In contrast to analytical studies [29, 45, 126] the MC method is able to incorporate real scattering mechanisms beyond the relaxation time approximation and study more complex geometries. This section discusses the influence of geometric variations, the lattice temperature and the impact of a steady state current. Additionally, the influence of the Pauli exclusion principle is studied. In this section the PSD is given as a spatial average along the channel.

5.6.1. Variation of the Channel Length

This section covers the influence of the channel length on the oscillation strengths of the fluctuations. Ungated and gated structures are investigated, the first for two different doping concentrations.

The results for the voltage fluctuations are shown in figure 5.12. The PSD of the electric potential fluctuations for the ungated structure is computed for two different doping concentrations, shown in figure 5.12(a) and 5.12(b) and three different channel lengths, respectively. The results for the gated case and a doping concentration of $1 \times 10^{18}\,\mathrm{cm}^{-3}$ is given in figure 5.12(c). In all cases the frequency of the plasma resonances is increasing for shorter channel lengths, which was already discussed in section 5.4 concerning the dispersion relations.

Furthermore, the oscillation amplitude is decreasing for shorter channels as the influence of the fixed boundary conditions ($U_\mathrm{S} = U_\mathrm{D} = 0\,\mathrm{V}$) is weaker. The oscillation strength increases for higher carrier concentrations as well, as the associate forces for larger concentrations are stronger. The same behaviour was found for plasma oscillations in bulk material, presented in section 5.2.

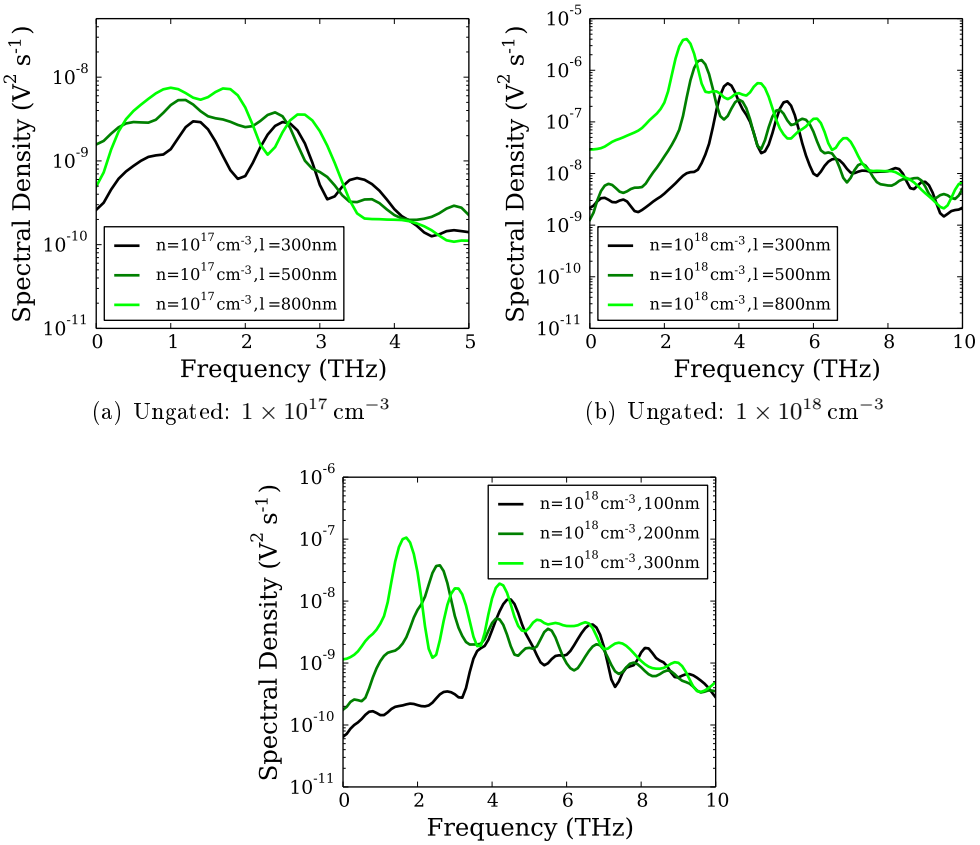

(a) Ungated: $1 \times 10^{17}\,\mathrm{cm}^{-3}$

(b) Ungated: $1 \times 10^{18}\,\mathrm{cm}^{-3}$

(c) Gated: $1 \times 10^{18}\,\mathrm{cm}^{-3}$

Figure 5.12.: PSD of voltage fluctuations in the ungated and gated channel for different channel lengths and doping concentrations: Longer channels lead to stronger oscillations.

5.6.2. Variation of the Lattice Temperature

Plasma waves in the THz region are strongly damped by scattering processes, since the scattering rates are in the same order of magnitude. In order to investigate the influence of the scattering rates, simulations were performed for different lattice temperature. At cryogenic temperatures phonon scattering is strongly reduced since fewer phonons are available. Especially scattering with optical phonons, which is usually the dominant scattering mechanism, is suppressed.

Simulations were carried out for an ungated and a gated structure with channel lengths of 500 and 300 nm, respectively. The computed PSD of the voltage and current fluctuations is presented for the ungated (figure 5.13) and gated (figure 5.14) case at different lattice temperatures, reaching from cryogenic temperatures to room temperature.

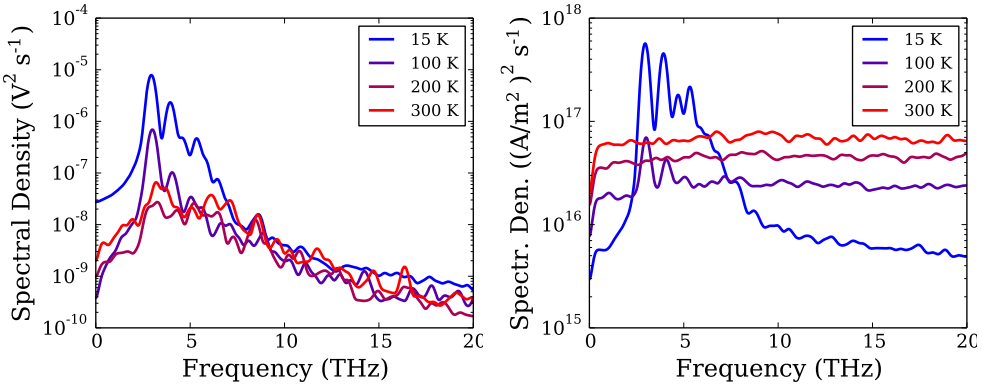

(a) Spectral density of voltage fluctuations

(b) Density of the total current oscillations (conduction current + displacement current)

Figure 5.13.: Calculated voltage and current spectral densities at different lattice temperatures for the ungated structure at a doping concentration of $1 \times 10^{18}\,\mathrm{cm}^{-3}$ and a channel length of $l = 500\,\mathrm{nm}$

Both simulation series show the same behaviour. At 15 K, several modes are visible in the voltage and current oscillation spectra. However, the scattering rates increase for higher temperatures and oscillations are more effectively damped. At a lattice temperature of 100 K oscillations are still visible but vanish for higher temperatures. There are no oscillations visible at room temperature. For higher lattice temperatures the general noise level of current oscillations increase, which can be attributed to the additional thermal energy of carriers and increased scattering rate.

Since this study plots the PSD, the square-root has to be taken to derive

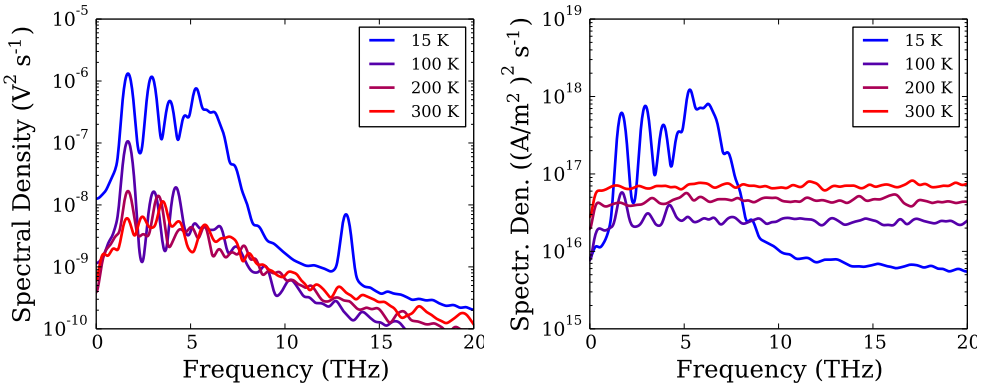

(a) Spectral density of voltage fluctuations

(b) Density of the total current oscillations (conduction current + displacement current)

Figure 5.14.: Calculated voltage and current spectral densities at different lattice temperatures for the gated structure at a doping concentration of $1 \times 10^{18}\,\mathrm{cm}^{-3}$ and a channel length of $l = 300\,\mathrm{nm}$

the amplitude spectra. It has to be noted that the amplitude values given by Marinchio [126] are in the range of $1 \times 10^{9}\,\mathrm{A\,m}^{-2}$ at room temperature, which coincide well with the current densities derived in this study at cryogenic temperatures. The difference is attributed to the more realistic incorporation of scattering processes used in the MC method compared to the used velocity relaxation time in the analytical approach. A weaker emission of THz radiation for higher temperatures was found in experiments [60] as well.

5.6.3. Bias Dependency

Up to this section the devices have been simulated under equilibrium conditions with no applied electric field. In experiments [60, 62] the onset of THz-emission was observed at applied drain biases, especially when the transistor is driven into the saturation regime. This section covers simulation results of an ungated and gated structure at different applied source-drain voltages and discusses its current density spectra.

Figures 5.15(a) and 5.15(b) show the PSD-spectra for the ungated and gated case. The insets give the corresponding IV-curves. Both simulated structures show a current saturation at small applied voltages, which can be explained by the short channels and large involved electric fields. Additionally, there are no doped contact regions where a voltage drop occurs when compared to real FETs. It can be observed that for larger currents the plasma peaks are washed out and no oscillations sustain. No observation for an amplification or enhanced oscil-

lation strength of plasma waves can be observed. Under larger electric fields carriers are significantly heated (compare with section 4.1.1.1) and thus scatter more often, destroying the plasma oscillation. As for increased lattice temperatures the general noise level raise, underlining this conclusion.

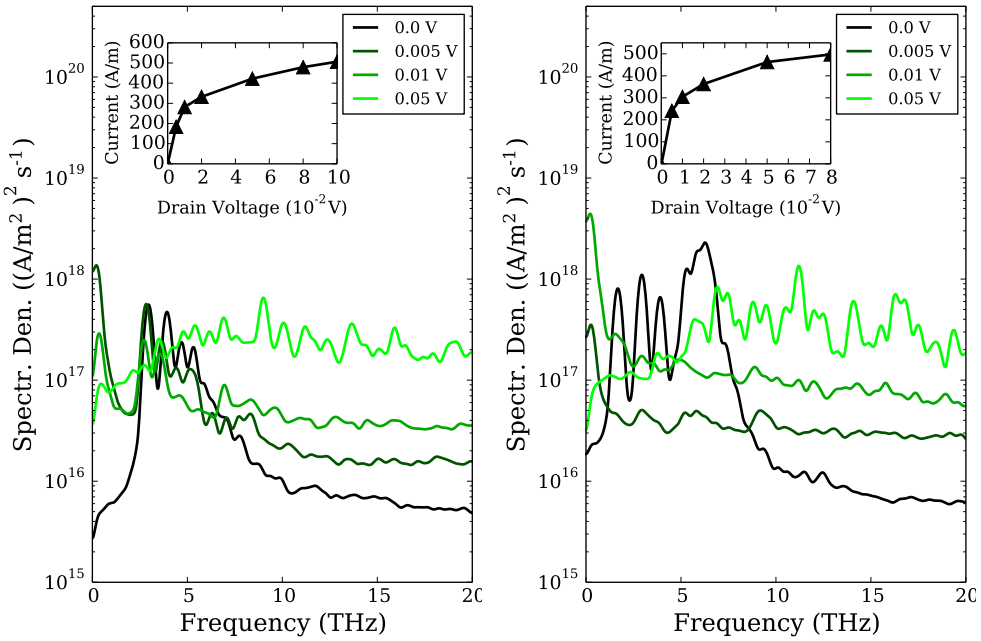

(a) Ungated: $l = 500\,\mathrm{nm}$ (b) Gated: $l = 300\,\mathrm{nm}$

Figure 5.15.: Current density PSD for different applied biases at a lattice temperature of 15 K: for larger currents the plasma peaks are suppressed.

5.6.4. Influence of the Pauli Exclusion Principle

In section 3.8 the Pauli exclusion principle in MC simulation was introduced. It was found, that for higher electron concentrations the carriers are pushed towards the high energy tail of the distribution function. Later, in the calibration section of doped materials 4.2, the impact on the electron drift velocity in steady state and dynamic scenarios were investigated. In general an increased doping concentration leads to a lower mobility due to the increased scattering with impurities. However, for doping levels where PEP gets important and needs to be considered some of the "lost" mobility can be regained due to the increasing blocking of scattering processes.

The influence of the Pauli principle was investigated by comparing simulations

at different lattice temperatures to simulations where PEP has been neglected. Figure 5.16 summarizes the results: for both structures it is found that the oscillations are stronger when PEP is considered. Especially for the ungated structure it is found that the oscillation are visible at higher lattice temperatures. However, there are still no current oscillations observable at room temperature.

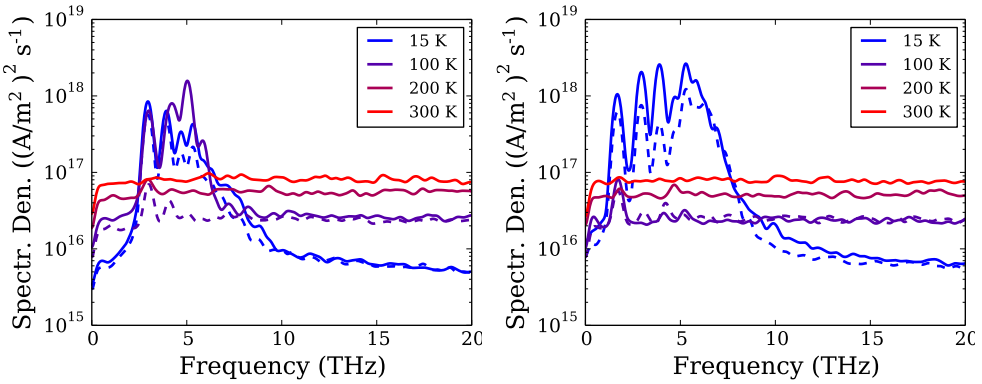

(a) Ungated: $l = 500\,\mathrm{nm}$ (b) Gated: $l = 300\,\mathrm{nm}$

Figure 5.16.: Current density PSD as a function of temperature and activated PEP-module. The dashed lines refer to simulations without Pauli blocking: with activated PEP the oscillations are stronger and sustain up to higher temperatures.

The analytical hydrodynamic theory used by Dyakonov [29] or Marinchio [126] excludes quantum effects like the Pauli exclusion principle. In the presented simulation results it was found that the frequency of the plasma peaks is not shifting. Only the oscillation strength increases.

6. THz Plasma Waves in FETs

The most important properties of THz plasma waves in simple ungated and gated channels were discussed in the last chapter. It was shown that the computed plasma frequencies follow loosely the proposed dispersion relations given by Dyakonov. However, a real FET consists usually not of a single gated region more by a combination of both ungated and gated parts. This section discusses the plasma frequencies and mode patterns for such devices which should be more comparable to experiments.

6.1. Combination of Ungated and Gated Regions

The first simulations were carried out for a combined ungated and gated device section, shown in figure 6.1(a). First, the ungated part of the device was fixed to a constant value of $u = 50\,\mathrm{nm}$ and the length of gated part g was varied between 50 and 250 nm. The results are summarized in figure 6.1(b). In figure 6.1(c) the gated part was fixed and the length of the ungated regions changes. Markers refer to standalone simulations such as performed in the last chapter. The fundamental plasma mode for each simulation geometry is plotted as a straight simple line since no explicit channel length can be given for meaningful comparisons with the standalone devices.

By fixing the length of the ungated part and increasing the gated region the plasma frequency approaches for increasing gate length the value given by the standalone gated device. Furthermore, it is observable that the plasma frequency converges to the value of the gated dispersion relation for the total channel length. The ungated part loses influence while the gated region with its fixed gate potential dominates. The second study shown in figure 6.1(c) reveals a quite different behaviour. Fixing the gate length and increasing the length of the ungated part leads only to a slight shift of the plasma frequency. However, the plasma peak is not approaching the ungated value as observed in figure 6.1(b). The plasma peak is even falling below the dispersion relation for the ungated region.

It has been noted by Mateos in [127] that for the peaks appearing in the noise spectra observed during rectification in the detection process the resonant frequency is given by geometric parameters: the resulting frequency for a combination of ungated and gated regions should be given by a combination of the

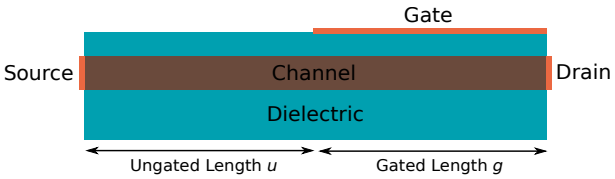

(a) Schematic of the simulated structure consisting of an ungated and gated part.

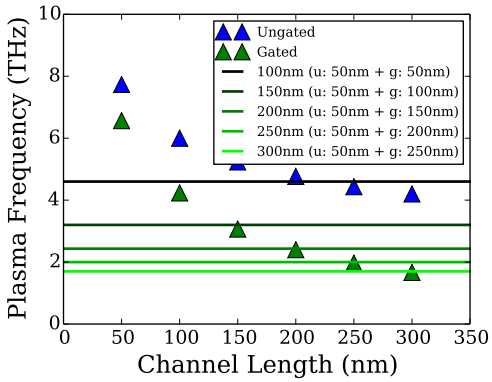

(b) Structure where the ungated region has been fixed to a length of $u = 50\,\text{nm}$ and the length of the gated region g varies

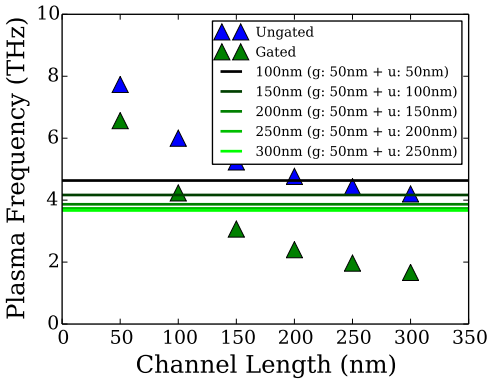

(c) Structure where the gated region has been fixed to $g = 50\,\text{nm}$ and u varies

Figure 6.1.: MC simulation results (represented by solid lines, since no channel length is associated) of the plasma frequency for structures consisting of an ungated and gated channel. The symbols represent the expected plasma frequencies when the ungated and gated part is considered alone.

standalone plasma frequencies weighted by their structural influence. In the presented simulations no such behaviour was observed. The plasma frequency for $u = g = 50\,\text{nm}$ is located at $l = 100\,\text{nm}$ with a slight shift towards the gated value. According to their theory the frequency should lay between the two values at $l = 50\,\text{nm}$.

Next, simulations were performed for ungated-gated-ungated devices which resemble more realistic devices. Two studies were carried out: first, the length of the ungated parts of the channel were fixed to $u = 150\,\text{nm}$ and the gated region was varied in length. For the second test case the gated part was fixed to $g = 50\,\text{nm}$ and the influence of the length of the ungated region was studied. Both simulation series show a decreasing plasma frequency either by increasing the ungated or gated channel region. Only a small change of the resulting frequency is visible for longer devices, thus making a comparison with experi-

ments quite difficult because a smaller frequency dispersion is visible, compared to the standalone ungated and gated devices. Following the previous simulation of ungated-gated structures the resulting frequency can not deduced from the simple ungated and gated devices. Exemplarily, this can be clearly observed for the 150-50-150 nm structure where the plasma frequency lies below the ungated and gated plasma frequency.

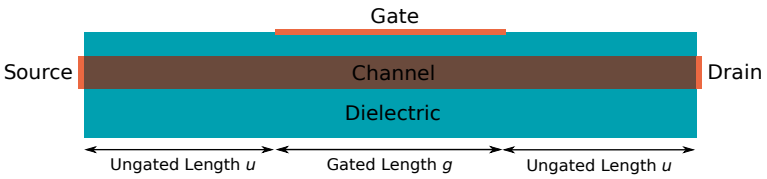

(a) Schematic of the simulated structure consisting of an ungated and gated part.

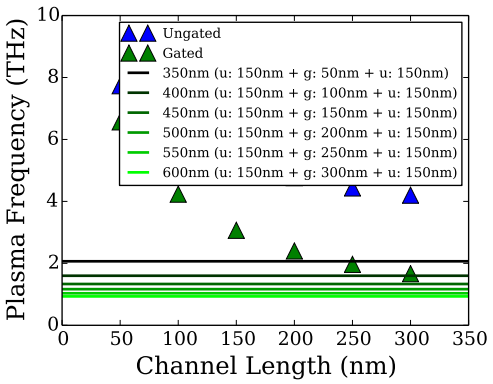

(b) Structure where the length of the ungated region has been fixed to $u = 150\,\text{nm}$ and the ungated region g varies

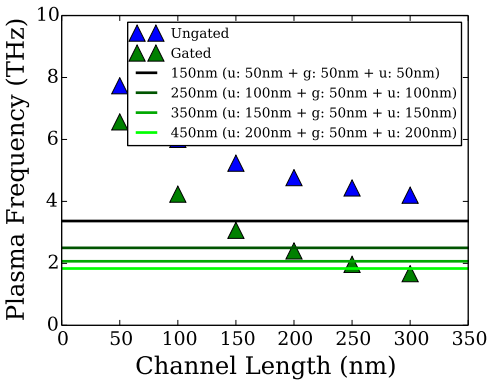

(c) Structure where the gated region has been fixed to a length of $g = 50\,\text{nm}$ and the ungated region u varies

Figure 6.2.: Calculated plasma frequencies for devices consisting of combined ungated and gated regions. Markers refer to standalone simulations and solid lines mark one combination of an ungated-gated-ungated devices.

6.2. Mode Profiles for Combinated Devices

The mode profile of the electric potential and the current density were discussed in chapter 5.5. Simulations showed that standing wave patterns are formed in the channel. For both devices the electric potential formed nodes at the contacts, since the potential was fixed by the boundary conditions. The current density fluctuations formed nodes for the ungated channel at the channel contacts while it showed peaks for the gated device. This section summarizes the results for combinated structures.

Figure 6.3 shows the mode profiles of the electric potential for an ungated-gated and ungated-gated-ungated device (every part of the device has a length of 50 nm. Being consistent with previous calculations, nodes are formed at the channel contacts. Higher order modes can be observed at higher frequencies. Additionally, it has to be noted that the oscillations under the gate are weaker compared to the ungated region - the gate fixes the potential and damps evolving oscillations.

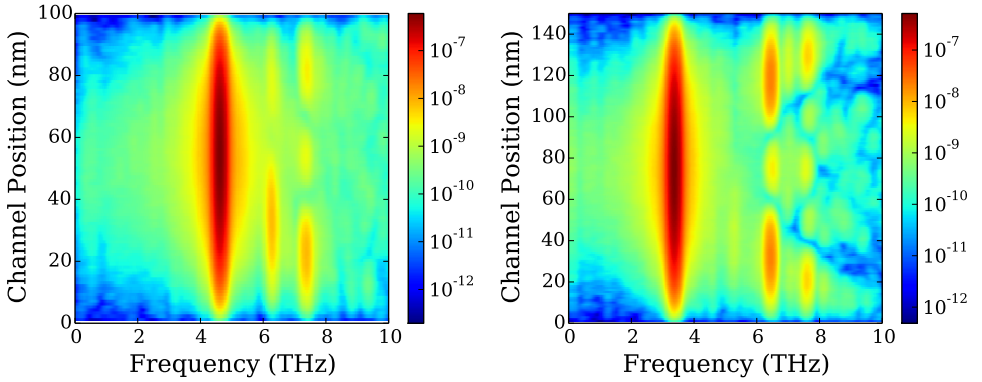

(a) Ungated-gated devices: gate covers the channel between 50 and 100 nm

(b) Ungated-gated-ungated: every section is 50 nm long

Figure 6.3.: Mode profiles for the electric potential for a ungated-gated and ungated-gated-ungated device. As for the standalone devices the electric potential forms standing waves.

Furthermore, the mode profiles for the conduction current can be evaluated. For all investigated devices it was found that the number of current peaks for each mode is equal to the standalone devices (e.g. two for the fundamental mode). The modal current profile for the ungated-gated device is given by whether the region is covered by a gate or not. In the ungated part the current tends to zero at the contact while it shows a peak at the contact under the gate. This resembles basically the findings of the previos chapter. The situation is more complicated

for the ungated-gated-ungated device: the current profile are neither given by the ungated parts, nor by the gated part of the channel. However, the current profile can be seen as an hybrid profile, given by the combination of ungated and gated regions.

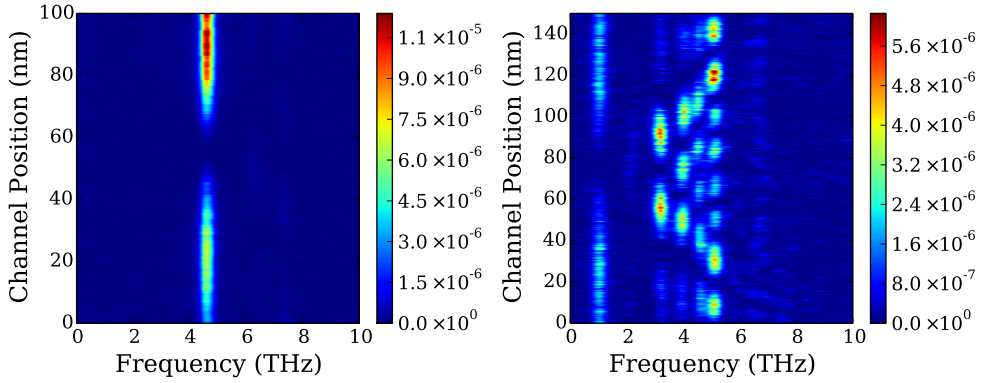

(a) Ungated-gated devices: gate covers the channel between 50 and 100 nm

(b) Ungated-gated-ungated: every section is 50 nm long

Figure 6.4.: Conduction current fluctuations for an ungated-gated and ungated-gated-ungated device.

In conclusion, these simulations indicate that the plasma peak observed in experiments can not be calculated following the dispersion relation for the single gated channel as it is mostly done in available experiments [59, 62]. The oscillating current ranges over the whole device and is not only restricted to gated regions as usually assumed.

7. Conclusion

Sensing with THz waves has become a large field which is interesting for many scientific and industrial applications. However, there is still a lack for small and robust solid-state devices acting as sources. The goal of this work was to investigate the device properties for plasma wave excitation and compare to present experimental work. The results should lead to a deeper insight and lead to new devices.

A Monte Carlo device simulator was developed as an investigative tool during this work. One of the major achievements was to include sophisticated material parameters relying on a variety of measurements or ab initio calculations, rather using most of these parameters as fitting values. A simple three valley band-structure model was used which is able to reproduce steady-state drift-velocity curves known from literature. Scattering rates for various processes were computed using efficient formulations. The device simulator employs models for heterojunctions and tunneling probabilities. Ohmic and Schottky contacts are included serving as boundary conditions for the solution of the Poisson equation. A fast solution for the electric potential and field is realized by using a parallized solver for the linear system of equations. Results, showing the importance of the Pauli exclusion principle, are presented to demonstrate its influence on transport characteristics.

The second part of this work describes the presence of plasma waves in simplified FET-like structures. Simulations showing the influence of the channel width and length were carried out. It was found that the results are in good agreement with previously developed hydrodynamic models of different authors. The plasma frequency increases for shorter channels and the number of modes grows with the channel thickness. Furthermore, basic properties with focus on an application as possible emitters were investigated:

- Standing wave patterns are formed in the channel
- Current oscillations are overdamped at lattice temperatures above 100 K
- A steady-state current flow through the channel heats carriers and destroys oscillations
- The Pauli exclusion principle does not affect the plasma frequency
- The plasma frequency in a common FET (ungated-gated-ungated device) does not follow the dispersion relation of a single gated region

- Ungated regions at contacts can not be used for diode-like two terminal devices since the current density fluctuations tend to zero

In conclusion, the performed simulations suggest that the excitation of plasma is possible in FET-like devices but is restricted to very limited use. The operating temperature and low current densities involved make it impracticable for an application as a real THz source. The experimentally observed broad emission spectra could be based on thermal emission of the heated electron gas like stated by Shalygin [128]. However, further experiments would certainly be helpful to finally clarify the emission of THz radiation.

A. Material Parameters

This section summarizes the values for the models of the semiconductor's band-structure and the used material parameters needed for computating the scattering rates.

A.1. General Parameter

	GaAs	InAs	AlAs	$In_{0.53}Ga_{0.47}As$	$In_{0.52}Al_{0.48}As$
a (nm)	0.5653	0.6058	0.5661	0.5868	0.5868
ρ ($kg\,cm^{-3}$)	5317	5680	3730	5509	4744
s_l ($m\,s^{-1}$)	5400	4410	6480	4875	5404
ϵ_S (ϵ_0)	12.90	15.15	9.46	14.09	12.42
ϵ_∞ (ϵ_0)	10.90	12.25	8.15	11.62	10.28

Table A.1.: Basic Parameters

	GaAs	InAs	AlAs	$In_{0.53}Ga_{0.47}As$	$In_{0.52}Al_{0.48}As$
m^* (m_0)					
Γ	0.067	0.026	0.150	0.043	0.073
L	0.075/1.90	0.050/0.64	0.150/1.32	0.062/1.23	0.098/0.96
X	0.23/1.30	0.160/1.13	0.220/0.97	0.192/1.21	0.188/1.05
E_G (eV)					
Γ	1.52	0.42	3.09	0.82	1.53
L	1.81	1.13	2.46	1.37	1.77
X	1.98	1.43	2.24	1.48	1.82
α (eV^{-1})					
Γ	0.573			1.180	0.561
L	0.510			0.588	0.204
X	0.580			0.649	0.204

Table A.2.: Bandstructure Parameters at 0 K

A.2. Phonon Energies and Deformation Potentials

The formulation of the various scattering rates include mostly a deformation potential, describing the strength of the scattering. Furthermore, they involve a phonon energy used for the energy exchange during the process. These parameters are summarized here.

	$In_{0.53}Ga_{0.47}As$			$In_{0.52}Al_{0.48}As$		
$\hbar\omega_{\mathrm{op}}$ (meV)	32.7			41.0		
$\hbar\omega_{\mathrm{iv}}$ (meV)						
	Γ	L	X	Γ	L	X
Γ		22.76	23.84		29.0	29.0
L	22.76	26.96	23.12	29.0	29.0	29.0
X	23.84	23.12	22.76	29.0	29.0	29.0

Table A.3.: Phonon Energies

	$In_{0.53}Ga_{0.47}As$			$In_{0.52}Al_{0.48}As$		
U_{alloy} (eV)	0.53			0.47		
D_{ac} (eV)	9.2			8.0		
D_{nonp} ($\mathrm{eV\,nm^{-1}}$)	30.0			30.0		
D_{iv} ($\mathrm{eV\,nm^{-1}}$)						
	Γ	L	X	Γ	L	X
Γ		70.0	70.0		100.0	100.0
L	70.0	70.0	50.0	100.0	100.0	100.0
X	70.0	50.0	58.0	100.0	100.0	100.0

Table A.4.: Deformation Potentials

Bibliography

[1] D. Mittleman. *Sensing with terahertz radiation*. Vol. 337. Springer Berlin, 2003.

[2] R. Ulbricht, E. Hendry, J. Shan, T. F. Heinz, and M. Bonn. "Carrier dynamics in semiconductors studied with time-resolved terahertz spectroscopy". In: *Rev. Mod. Phys.* 83 (2 June 2011), pp. 543–586.

[3] S. Wietzke, C. Jansen, M. Reuter, T. Jung, D. Kraft, S. Chatterjee, B.M. Fischer, and M. Koch. "Terahertz spectroscopy on polymers: A review of morphological studies". In: *Journal of Molecular Structure* 1006.1–3 (2011), pp. 41–51.

[4] T. Kawano, I. Katayama, J. Ohara, M. Ashida, and J. Takeda. "Intermolecular THz vibrations relevant to optically and thermally induced magnetic phase transitions in the strongly correlated organic radical TTTA". In: *Journal of the Physical Society of Japan* 83.1 (2014), p. 014713.

[5] C. Wolpert, K. Sumida, F. Blanchard, and K. Tanaka. "Probing hydration dynamics of metal-organic frameworks by broadband THz pulses". In: *CLEO: 2014*. Optical Society of America, 2014, SF1F.1.

[6] E. P. J. Parrott, B. M. Fischer, L. F. Gladden, J. A. Zeitler, and P. U. Jepsen. "Terahertz spectroscopy of crystalline and non-crystalline solids". In: *Terahertz Spectroscopy and Imaging*. Ed. by Kai-Erik Peiponen, Axel Zeitler, and Makoto Kuwata-Gonokami. Vol. 171. Springer Series in Optical Sciences. Springer Berlin Heidelberg, 2013, pp. 191–227.

[7] B. M. Fischer, S. Wietzke, M. Reuter, O. Peters, R. Gente, C. Jansen, N. Vieweg, and M. Koch. "Investigating material characteristics and morphology of polymers using terahertz technologies". In: *Terahertz Science and Technology, IEEE Transactions on* 3.3 (May 2013), pp. 259–268.

[8] Z. D. Taylor, R. S. Singh, D. B. Bennett, P. Tewari, C. P. Kealey, N. Bajwa, M. O. Culjat, A. Stojadinovic, H. Lee, J. Hubschman, E. R. Brown, and W. S. Grundfest. "THz medical imaging: in vivo hydration sensing". In: *Terahertz Science and Technology, IEEE Transactions on* 1.1 (Sept. 2011), pp. 201–219.

[9] K. I. Zaytsev, K. G. Kudrin, S. A. Koroleva, I. N. Fokina, S. I. Volodarskaya, E. V. Novitskaya, A. N. Perov, V. E. Karasik, and S. O. Yurchenko. "Medical diagnostics using terahertz pulsed spectroscopy". In: *Journal of Physics: Conference Series* 486.1 (2014), p. 012014.

[10] L. S. von Chrzanowski, J. Beckmann, B. Marchetti, U. Ewert, and U. Schade. "Terahertz time domain spectroscopy for non-destructive testing of hazardous liquids". In: *Materials Testing* 54.6 (June 2012), pp. 444–450.

[11] L. Pierno, A. M. Fiorello, S. Scafe, J. Cunningham, A. D. Burnett, E. H. Linfield, and A. G. Davies. "THz-TDS analysis of hidden explosives for homeland security scenarios". In: *Millimeter Waves and THz Technology Workshop (UCMMT), 2013 6th UK, Europe, China*. Sept. 2013, pp. 1–2.

[12] G. Zieger, D. Born, S. Anders, E. Heinz, K. Peiselt, A. Bromel, V. Zakosarenko, T. May, and H.-G. Meyer. "A passive submillimeter video camera for security applications". In: *Infrared, Millimeter, and Terahertz Waves (IRMMW-THz), 2013 38th International Conference on*. Sept. 2013, pp. 1–2.

[13] S. Hadjiloucas, L. S. Karatzas, and J. W. Bowen. "Measurements of leaf water content using terahertz radiation". In: *Microwave Theory and Techniques, IEEE Transactions on* 47.2 (Feb. 1999), pp. 142–149.

[14] M. Kawase. "Application of Terahertz Waves to Food Science". In: *Food Science and Technology Research* 18.5 (2012), pp. 601–609.

[15] C. Jansen, S. Wietzke, and M. Koch. "Terahertz spectroscopy of polymers". English. In: *Terahertz Spectroscopy and Imaging*. Ed. by Kai-Erik Peiponen, Axel Zeitler, and Makoto Kuwata-Gonokami. Vol. 171. Springer Series in Optical Sciences. Springer Berlin Heidelberg, 2013, pp. 327–353.

[16] D. Grischkowsky, S. Keiding, M. van Exter, and C. Fattinger. "Far-infrared time-domain spectroscopy with terahertz beams of dielectrics and semiconductors". In: *J. Opt. Soc. Am. B* 7.10 (Oct. 1990), pp. 2006–2015.

[17] G. Klatt, F. Hilser, W. Qiao, M. Beck, R. Gebs, A. Bartels, K. Huska, U. Lemmer, G. Bastian, M.B. Johnston, M. Fischer, J. Faist, and T. Dekorsy. "Terahertz emission from lateral photo-Dember currents". In: *Opt. Express* 18.5 (Mar. 2010), pp. 4939–4947.

[18] Y.-S. Lee, T. Meade, V. Perlin, H. Winful, T. B. Norris, and A. Galvanauskas. "Generation of narrow-band terahertz radiation via optical rectification of femtosecond pulses in periodically poled lithium niobate". In: *Applied Physics Letters* 76.18 (2000), pp. 2505–2507.

[19] M. D. Thomson, V. Blank, and H. G. Roskos. "Terahertz white-light pulses from an air plasma photo-induced by incommensurate two-color opticalfields". In: *Opt. Express* 18.22 (Oct. 2010), pp. 23173–23182.

[20] M. Scheller, J. M. Yarborough, J. V. Moloney, M. Fallahi, M. Koch, and S. W. Koch. "Room temperature continuous wave milliwatt terahertz source". In: *Opt. Express* 18.26 (Dec. 2010), pp. 27112–27117.

[21] E. R. Brown, K. A. McIntosh, K. B. Nichols, and C. L. Dennis. "Photomixing up to 3.8 THz in low-temperature-grown GaAs". In: *Applied Physics Letters* 66.3 (1995), pp. 285–287.

[22] J. Ward, E. Schlecht, G. Chattopadhyay, A. Maestrini, J. Gill, F. Maiwald, H. Javadi, and I. Mehdi. "Capability of THz sources based on Schottky diode frequency multiplier chains". In: *Microwave Symposium Digest, 2004 IEEE MTT-S International*. Vol. 3. June 2004, 1587–1590 Vol.3.

[23] J. V. Siles, G. Chattopadhyay, E. Schlecht, C. Lee, R. Lin, J. Gill, J. Ward, C. Jung, I. Mehdi, P. Siegel, and A. Maestrini. "Next generation solid-state broadband frequency-multiplied terahertz sources". In: *Antennas and Propagation Society International Symposium (APSURSI), 2012 IEEE*. July 2012, pp. 1–2.

[24] A. Khalid, C. Li, V. Papageogiou, G. M. Dunn, M. J. Steer, I. G. Thayne, M. Kuball, C. H. Oxley, M. Montes Bajo, A. Stephen, J. Glover, and D. R. S. Cumming. "$In_{0.53}Ga_{0.47}As$ Planar Gunn Diodes Operating at a Fundamental Frequency of 164 GHz". In: *Electron Device Letters, IEEE* 34.1 (Jan. 2013), pp. 39–41.

[25] M. Tschernitz and J. Freyer. "140 GHz GaAs double-Read IMPATT diodes". English. In: *Electronics Letters* 31 (7 Mar. 1995), 582–583(1).

[26] M. Feiginov, C. Sydlo, O. Cojocari, and P. Meissner. "Resonant-tunnelling-diode operating at frequencies above 1.1 THz". In: *Applied Physics Letters* 99.23, 233506 (2011).

[27] L. A. Samoska. "An overview of solid-state integrated circuit amplifiers in the submillimeter-wave and THz regime". In: *Terahertz Science and Technology, IEEE Transactions on* 1.1 (Sept. 2011), pp. 9–24.

[28] D. C. Tsui, E. Gornik, and R. A. Logan. "Far infrared emission from plasma oscillations of Si inversion layers". In: *Solid State Communications* 35.11 (1980), pp. 875–877.

[29] M. Dyakonov and M. Shur. "Shallow water analogy for a ballistic field effect transistor: New mechanism of plasma wave generation by dc current". In: *Phys. Rev. Lett.* 71 (15 Oct. 1993), pp. 2465–2468.

[30] M. Razeghi, S. Slivken, Y. Bai, B. Gokden, and S. R. Darvish. "High power quantum cascade lasers". In: *New Journal of Physics* 11.12 (2009), p. 125017.

[31] B. S. Williams. "Terahertz quantum-cascade lasers". In: *Nature photonics* 1.9 (2007), pp. 517–525.

[32] S. Kumar. "Recent Progress in Terahertz Quantum Cascade Lasers". In: *Selected Topics in Quantum Electronics, IEEE Journal of* 17.1 (Jan. 2011), pp. 38–47.

[33] S. Kumar, Q. Hu, and J. L. Reno. "186 K operation of terahertz quantum-cascade lasers based on a diagonal design". In: *Applied Physics Letters* 94.13, 131105 (2009), pages.

[34] M. A. Belkin, F. Capasso, F. Xie, A. Belyanin, M. Fischer, A. Wittmann, and J. Faist. "Room temperature terahertz quantum cascade laser source based on intracavity difference-frequency generation". In: *Applied Physics Letters* 92.20, 201101 (2008), pages.

[35] K. Vijayraghavan, R. W. Adams, A. Vizbaras, M. Jang, C. Grasse, G. Boehm, M. C. Amann, and M. A. Belkin. "Terahertz sources based on Čerenkov difference-frequency generation in quantum cascade lasers". In: *Applied Physics Letters* 100.25, 251104 (2012), pages.

[36] Q. Y. Lu, N. Bandyopadhyay, S. Slivken, Y. Bai, and M. Razeghi. "Continuous operation of a monolithic semiconductor terahertz source at room temperature". In: *Applied Physics Letters* 104.22, 221105 (2014), pages.

[37] N. J. Pilgrim, A. Khalid, G. M. Dunn, and D. R. S. Cumming. "Gunn oscillations in planar heterostructure diodes". In: *Semiconductor Science and Technology* 23.7 (2008), p. 075013.

[38] A. Khalid, G. M. Dunn, N. Pilgrim, C. R. Stanley, I. G. Thayne, M. Holland, and D. R. S. Cumming. "Planar Gunn-type triode oscillator at 83 GHz". In: *Electronics Letters* 43.15 (July 2007), pp. 837–838.

[39] A. Khalid, N.J. Pilgrim, G.M. Dunn, M.C. Holland, C.R. Stanley, I.G. Thayne, and D.R.S. Cumming. "A Planar Gunn Diode Operating Above 100 GHz". In: *Electron Device Letters, IEEE* 28.10 (Oct. 2007), pp. 849–851.

[40] A. Khalid, G. M. Dunn, R. F. Macpherson, S. Thoms, D. Macintyre, C. Li, M. J. Steer, V. Papageorgiou, I. G. Thayne, M. Kuball, C. H. Oxley, M. Montes Bajo, A. Stephen, J. Glover, and D. R. S. Cumming. "Terahertz oscillations in an $In_{0.53}Ga_{0.47}As$ submicron planar Gunn diode". In: *Journal of Applied Physics* 115.11, 114502 (2014), pages.

[41] J. Mateos, S. Perez, D. Pardo, and T. Gonzalez. "Ultra fast Gunn effect at THz frequencies in HEMTs". In: *Indium Phosphide and Related Materials Conference Proceedings, 2006 International Conference on*. 2006, pp. 313–316.

[42] S. Pérez, T. González, D. Pardo, and J. Mateos. "Terahertz Gunn-like oscillations in InGaAs/InAlAs planar diodes". In: *Journal of Applied Physics* 103.9, 094516 (2008), pages.

[43] S. J. Allen, D. C. Tsui, and R. A. Logan. "Observation of the two-dimensional plasmon in silicon inversion layers". In: *Phys. Rev. Lett.* 38 (17 Apr. 1977), pp. 980–983.

[44] M. Nakayama. "Theory of surface waves coupled to surface carriers". In: *Journal of the Physical Society of Japan* 36.2 (1974), pp. 393–398.

[45] A. P. Dmitriev, A. S. Furman, and V. Yu. Kachorovskii. "Nonlinear theory of the current instability in a ballistic field-effect transistor". In: *Phys. Rev. B* 54 (19 Nov. 1996), pp. 14020–14025.

[46] A. P. Dmitriev, A. S. Furman, V. Yu. Kachorovskii, G. G. Samsonidze, and Ge. G. Samsonidze. "Numerical study of the current instability in a two-dimensional electron fluid". In: *Phys. Rev. B* 55 (16 Apr. 1997), pp. 10319–10325.

[47] M. Dyakonov and M. Shur. "Choking of electron flow: A mechanism of current saturation in field-effect transistors". In: *Phys. Rev. B* 51 (20 May 1995), pp. 14341–14345.

[48] M. Dyakonov and M. S. Shur. "Current instability and plasma waves generation in ungated two-dimensional electron layers". In: *Applied Physics Letters* 87.11, 111501 (2005), pages.

[49] M. Dyakonov and M. Shur. "Detection, mixing, and frequency multiplication of terahertz radiation by two-dimensional electronic fluid". In: *Electron Devices, IEEE Transactions on* 43.3 (Mar. 1996), pp. 380–387.

[50] A. Lisauskas, U. Pfeiffer, E. Öjefors, P. H. Bolìvar, D. Glaab, and H. G. Roskos. "Rational design of high-responsivity detectors of terahertz radiation based on distributed self-mixing in silicon field-effect transistors". In: *Journal of Applied Physics* 105.11, 114511 (2009), pages.

[51] J.-Q. Lu, M. Shur, J. L. Hesler, S. Liangquan, and R. Weikle. "Terahertz detector utilizing two-dimensional electronic fluid". In: *Electron Device Letters, IEEE* 19.10 (Oct. 1998), pp. 373–375.

[52] W. Knap, Y. Deng, S. Rumyantsev, J.-Q. Lü, M. S. Shur, C. A. Saylor, and L. C. Brunel. "Resonant detection of subterahertz radiation by plasma waves in a submicron field-effect transistor". In: *Applied Physics Letters* 80.18 (2002), pp. 3433–3435.

[53] W. Knap, Y. Deng, S. Rumyantsev, and M. S. Shur. "Resonant detection of subterahertz and terahertz radiation by plasma waves in submicron field-effect transistors". In: *Applied Physics Letters* 81.24 (2002), pp. 4637–4639.

[54] F. Teppe, W. Knap, D. Veksler, M. S. Shur, A. P. Dmitriev, V. Yu. Kachorovskii, and S. Rumyantsev. "Room-temperature plasma waves resonant detection of sub-terahertz radiation by nanometer field-effect transistor". In: *Applied Physics Letters* 87.5, 052107 (2005), pages.

[55] J.-Q. Lu and M. Shur. "Terahertz detection by high-electron-mobility transistor: Enhancement by drain bias". In: *Applied Physics Letters* 78.17 (2001), pp. 2587–2588.

[56] R. Al Hadi, H. Sherry, J. Grzyb, Y. Zhao, W. Förster, H.M. Keller, A. Cathelin, A. Kaiser, and U.R. Pfeiffer. "A 1 k-Pixel video camera for 0.7–1.1 Terahertz imaging applications in 65-nm CMOS". In: *IEEE Journal of Solid-State Circuits* 47.12 (2012), pp. 2999–3012.

[57] H. Sherry, J. Grzyb, Y. Zhao, R. Al Hadi, A. Cathelin, A. Kaiser, and U. Pfeiffer. "A 1k-Pixel CMOS Camera Chip for 25fps Real-Time Terahertz Imaging Applications". In: *Proc. IEEE Int. Solid-State Circuits Conf.* 2012, pp. 252–254.

[58] Y. Deng, R. Kersting, J. Xu, R. Ascazubi, X.-C. Zhang, M. Shur, R. Gaska, G. S. Simin, M. A. Khan, and V. Ryzhii. "Millimeter wave emission from GaN high electron mobility transistor". In: *Applied Physics Letters* 84.1 (2004), pp. 70–72.

[59] W. Knap, J. Lusakowski, T. Parenty, S. Bollaert, A. Cappy, V. V. Popov, and M. Shur. "Terahertz emission by plasma waves in 60 nm gate high electron mobility transistors". In: *Applied Physics Letters* 84.13 (2004), pp. 2331–2333.

[60] N. Dyakonova, A. El Fatimy, J. Łusakowski, W. Knap, M. I. Dyakonov, M.-A. Poisson, E. Morvan, S. Bollaert, A. Shchepetov, Y. Roelens, Ch. Gaquiere, D. Theron, and A. Cappy. "Room-temperature terahertz emission from nanometer field-effect transistors". In: *Applied Physics Letters* 88.14, 141906 (2006), pages.

[61] S. Boubanga-Tombet, F. Teppe, J. Torres, A. El Moutaouakil, D. Coquillat, N. Dyakonova, C. Consejo, P. Arcade, P. Nouvel, H. Marinchio, T. Laurent, C. Palermo, A. Penarier, T. Otsuji, L. Varani, and W. Knap. "Room temperature coherent and voltage tunable terahertz emission from nanometer-sized field effect transistors". In: *Applied Physics Letters* 97.26, 262108 (2010), pages.

[62] A. El Fatimy, N. Dyakonova, Y. Meziani, T. Otsuji, W. Knap, S. Vandenbrouk, K. Madjour, D. Théron, C. Gaquiere, M. A. Poisson, S. Delage, P. Prystawko, and C. Skierbiszewski. "AlGaN/GaN high electron mobility transistors as a voltage-tunable room temperature terahertz sources". In: *Journal of Applied Physics* 107.2, 024504 (2010), pages.

[63] T. Otsuji, Y. M. Meziani, M. Hanabe, T. Nishimura, and E. Sano. "Emission of terahertz radiation from InGaP/InGaAs/GaAs grating-bicoupled plasmon-resonant emitter". In: *Solid-State Electronics* 51.10 (2007), pp. 1319–1327.

[64] T. Otsuji, Y. M. Meziani, T. Nishimura, T. Suemitsu, W. Knap, E. Sano, T. Asano, and V. V. Popov. "Emission of terahertz radiation from dual grating gate plasmon-resonant emitters fabricated with InGaP/InGaAs/GaAs material systems". In: *Journal of Physics: Condensed Matter* 20.38 (2008), p. 384206.

[65] T. Otsuji, T. Watanabe, A. El Moutaouakil, H. Karasawa, T. Komori, A. Satou, T. Suemitsu, M. Suemitsu, E. Sano, W. Knap, and V. Ryzhii. "Emission of terahertz radiation from two-dimensional electron systems in semiconductor nano- and hetero-structures". English. In: *Journal of Infrared, Millimeter, and Terahertz Waves* 32.5 (2011), pp. 629–645.

[66] T. Onishi, T. Tanigawa, and S. Takigawa. "High power terahertz emission from a single gate AlGaN/GaN field effect transistor with periodic Ohmic contacts for plasmon coupling". In: *Applied Physics Letters* 97.9, 092117 (2010), pages.

[67] J. Sólyom. *Fundamentals of the Physics of Solids: Electronic Properties*. Springer-Verlag Berlin Heidelberg, 2009.

[68] C. Jungemann and B. Meinerzhagen. *Hierarchical Device Simulation: the Monte Carlo Perspective*. Springer-Verlag Wien, 2003.

[69] J. Gaidamour and P. Henon. "A Parallel Direct/Iterative Solver Based on a Schur Complement Approach". In: *Computational Science and Engineering, 2008. CSE '08. 11th IEEE International Conference on*. July 2008, pp. 98–105.

[70] C. Jacoboni and L. Reggiani. "The Monte Carlo method for the solution of charge transport in semiconductors with applications to covalent materials". In: *Review of Modern Physics* 55 (3 July 1983), pp. 645–705.

[71] D. Dolgos. *Full-band Monte Carlo simulation of single photon avalanche diodes*. ETH, 2011.

[72] F.M. Bufler, A. Schenk, and W. Fichtner. "Proof of a simple time-step propagation scheme for Monte Carlo simulation". In: *Mathematics and Computers in Simulation* 62.3–6 (2003). 3rd {IMACS} Seminar on Monte Carlo Methods, pp. 323–326.

[73] C. Jacoboni. *Survey of Classical Physics*. Vol. 165. Springer Series in Solid-State Sciences. Springer Berlin Heidelberg, 2010.

[74] C. Herring and E. Vogt. "Transport and Deformation-Potential Theory for Many-Valley Semiconductors with Anisotropic Scattering". In: *Phys. Rev.* 101 (3 1956), pp. 944–961.

[75] S. Smirnov. *Physical Modeling of Electron Transport in Strained Silicon and Silicon-Germanium*. TU Wien, 2003.

[76] I. Vurgaftman, J. R. Meyer, and L. R. Ram-Mohan. "Band parameters for III–V compound semiconductors and their alloys". In: *Journal of Applied Physics* 89.11 (2001), pp. 5815–5875.

[77] S. Adachi, ed. *GaAs and Related Materials: Bulk Semiconducting and Superlattice Properties*. World Scientific Publishing Company, 1994.

[78] M. Hass and B. W. Henvis. "Infrared lattice reflection spectra of III–V compound semiconductors". In: *Journal of Physics and Chemistry of Solids* 23.8 (1962), pp. 1099–1104.

[79] I. Watanabe, T. Torikai, and K. Taguchi. "Monte Carlo simulation of impact ionization rates in InAlAs-InGaAs square and graded barrier superlattice". In: *Quantum Electronics, IEEE Journal of* 31.10 (1995), pp. 1826–1834.

[80] M. A. Littlejohn, K. W. Kim, and H. Tian. "High-field transport in InGaAs and related heterostructures". In: *Properties of Lattice-Mathed and Strained Indium Gallium Arsenide* (1993). Ed. by P. Bhattacharya, pp. 107–116.

[81] K. F. Brennan and D. H. Park. "Theoretical comparison of electron real-space transfer in classical and quantum two-dimensional heterostructure systems". In: *Journal of Applied Physics* 65.3 (1989), pp. 1156–1163.

[82] M. A. Littlejohn, J. R. Hauser, T. H. Glisson, D. K. Ferry, and J. W. Harrison. "Alloy scattering and high field transport in ternary and quaternary III–V semiconductors". In: *Solid-State Electronics* 21.1 (1978), pp. 107–114.

[83] C. Jacoboni and P. Lugli. *The Monte Carlo method for Semiconductor Device Simulation*. Springer Verlag, 1989.

[84] C. Jacoboni, F. Nava, C. Canali, and G. Ottaviani. "Electron drift velocity and diffusivity in germanium". In: *Phys. Rev. B* 24 (2 July 1981), pp. 1014–1026.

[85] W. Fawcett, A. D. Boardman, and S. Swain. "Monte Carlo determination of electron transport properties in gallium arsenide". In: *Journal of Physics and Chemistry of Solids* 31.9 (1970), pp. 1963–1990.

[86] B. K. Ridley. *Quantum processes in semiconductors*. Vol. 2nd edition. Clarendon Press (Oxford and New York), 1988.

[87] M. V. Fischetti. "Monte Carlo simulation of transport in technologically significant semiconductors of the diamond and zinc-blende structures. I. Homogeneous transport". In: *IEEE Transactions on Electron Devices* 38.3 (1991), pp. 634–649.

[88] J. R. Hauser, M. A. Littlejohn, and T. H. Glisson. "Velocity-field relationship of InAs-InP alloys including the effects of alloy scattering". In: *Applied Physics Letters* 28.8 (1976), pp. 458–461.

[89] H. S. Kim, H. Tian, K. W. Kim, and M. A. Littlejohn. "Electron velocity-field characteristics of $In_{0.52}Al_{0.48}As$". In: *Applied Physics Letters* 61.10 (1992), pp. 1202–1204.

[90] B K Ridley. "Reconciliation of the Conwell-Weisskopf and Brooks-Herring formulae for charged-impurity scattering in semiconductors: Third-body interference". In: *Journal of Physics C: Solid State Physics* 10.10 (1977), p. 1589.

[91] K. Kim and K. Hess. "Ensemble Monte Carlo simulation of semiclassical nonlinear electron transport across heterojunction band discontinuities". In: *Solid-State Electronics* 31.5 (1988), pp. 877–885.

[92] T. H. Glisson, J. R. Hauser, M. A. Littlejohn, K. Hess, B. G. Streetman, and H. Shichijo. "Monte Carlo simulation of real-space electron transfer in GaAs-AlGaAs heterostructures". In: *Journal of Applied Physics* 51.10 (1980), pp. 5445–5449.

[93] T. González and D. Pardo. "Physical models of ohmic contact for Monte Carlo device simulation". In: *Solid-State Electronics* 39.4 (1996), pp. 555–562.

[94] P. Palestri, N. Barin, D. Esseni, and C. Fiegna. "Stability of self-consistent Monte Carlo Simulations: effects of the grid size and of the coupling scheme". In: *Electron Devices, IEEE Transactions on* 53.6 (June 2006), pp. 1433–1442.

[95] A. Ghetti, X. Wang, F. Venturi, and F. A. Leon. "Stability Issues in Self-Consistent Monte Carlo-Poisson Simulations". English. In: *Simulation of Semiconductor Devices and Processes*. Springer Vienna, 1995, pp. 388–391.

[96] M. V. Fischetti and S. E. Laux. "Monte Carlo analysis of electron transport in small semiconductor devices including band-structure and space-charge effects". In: *Phys. Rev. B* 38 (14 Nov. 1988), pp. 9721–9745.

[97] P. W. Rambo and J. Denavit. "Time stability of Monte Carlo device simulation". In: *Computer-Aided Design of Integrated Circuits and Systems, IEEE Transactions on* 12.11 (Nov. 1993), pp. 1734–1741.

[98] P. Palestri, N. Barin, D. Esseni, and C. Fiegna. "Revised stability analysis of the nonlinear Poisson scheme in self-consistent Monte Carlo device simulations". In: *Electron Devices, IEEE Transactions on* 53.6 (June 2006), pp. 1443–1451.

[99] P. Degond and F. Guyot-Delaurens. "Particle simulations of the semiconductor boltzmann equation for one-dimensional inhomogeneous structures". In: *Journal of Computational Physics* 90.1 (1990), pp. 65–97.

[100] C. J. Wordelman and U. Ravaioli. "Integration of a particle-particle-particle-mesh algorithm with the ensemble Monte Carlo method for the simulation of ultra-small semiconductor devices". In: *Electron Devices, IEEE Transactions on* 47.2 (Feb. 2000), pp. 410–416.

[101] S. Bosi and C. Jacoboni. "Monte Carlo high-field transport in degenerate GaAs". In: *Journal of Physics C: Solid State Physics* 9.2 (1976), p. 315.

[102] P. Lugli and D. K. Ferry. "Degeneracy in the ensemble Monte Carlo method for high-field transport in semiconductors". In: *Electron Devices, IEEE Transactions on* 32.11 (Nov. 1985), pp. 2431–2437.

[103] M. Zebarjadi, C. Bulutay, K. Esfarjani, and A. Shakouri. "Monte Carlo simulation of electron transport in degenerate and inhomogeneous semiconductors". In: *Applied Physics Letters* 90.9, 092111 (2007), pages.

[104] A. Islam and K. Kalna. "Monte Carlo simulations of mobility in doped GaAs using self-consistent Fermi-Dirac statistics". In: *Semiconductor Science and Technology* 26.5 (2011), p. 055007.

[105] P. Tadyszak, F. Danneville, A. Cappy, L. Reggiani, L. Varani, and L. Rota. "Monte Carlo calculations of hot-carrier noise under degenerate conditions". In: *Applied Physics Letters* 69.10 (1996), pp. 1450–1452.

[106] M. A. Haase, V. M. Robbins, N. Tabatabaie, and G. E. Stillman. "Subthreshold electron velocity-field characteristics in GaAs and $In_{0.53}Ga_{0.47}As$". In: *Journal of Applied Physics* 57.6 (1985), pp. 2295–2298.

[107] T. H. Windhorn, L. W. Cook, and G. E. Stillman. "The electron velocity-field characteristic for n – $In_{0.53}Ga_{0.47}As$ at 300 K". In: *IEEE Electron Device Letters* 3.1 (Jan. 1982), pp. 18–20.

[108] N. Shigekawa, T. Furuta, and K. Arai. "Time-of-flight measurements of electron velocity in an $In_{0.52}Al_{0.48}As/In_{0.53}Al_{0.47}As/In_{0.52}Al_{0.48}As$ double heterostructure". In: *Applied Physics Letters* 57.1 (1990), pp. 67–69.

[109] J. G. Ruch and G. S. Kino. "Transport Properties of GaAs". In: *Phys. Rev.* 174 (3 Oct. 1968), pp. 921–931.

[110] S. M. Sze and K. K. Ng. *Physics of Semiconductor Devices*. John Wiley & Sons, Inc., 2006.

[111] A. Tessmann, A. Leuther, H. Massler, and M. Seelmann-Eggebert. "A High Gain 600 GHz Amplifier TMIC Using 35 nm Metamorphic HEMT Technology". In: *Compound Semiconductor Integrated Circuit Symposium (CSICS), 2012 IEEE*. Oct. 2012, pp. 1–4.

[112] A. Tessmann, A. Leuther, H. Massler, V. Hurm, M. Kuri, M. Zink, M. Riessle, H.P. Stulz, M. Schlechtweg, and O. Ambacher. "A 600 GHz low-noise amplifier module". In: *Microwave Symposium (IMS), 2014 IEEE MTT-S International*. June 2014, pp. 1–3.

[113] D. S. Romanovskiy, S. A. Tarasov, G. B. Galiev, and S. S. Pushkarev. "Investigation of In 0.7 Ga 0.3 As/In 0.7 Al 0.3 As metamorphic HEMT- heterostructures by photoluminescence spectroscopy". In: *Journal of Physics: Conference Series* 541.1 (2014), p. 012080.

[114] Nabil S. Mansour, Karim Diff, and Kevin F. Brennan. "Ensemble Monte Carlo study of electron transport in degenerate bulk GaAs". In: *Journal of Applied Physics* 70.11 (1991), pp. 6854–6859.

[115] J. F. Millithaler, L. Reggiani, J. Pousset, L. Varani, C. Palermo, W. Knap, J. Mateos, T. González, S. Perez, and D. Pardo. "Monte Carlo investigation of terahertz plasma oscillations in ultrathin layers of n-type $In_{0.53}Ga_{0.47}As$". In: *Applied Physics Letters* 92.4, 042113 (2008).

[116] J. F. Millithaler, L Reggiani, J Pousset, G Sabatini, L Varani, C Palermo, J Mateos, T Gonz?lez, S Perez, and D Pardo. "Terahertz oscillations in ultra-thin n-$In_{0.53}Ga_{0.47}As$ ungated channels". In: *Journal of Physics: Condensed Matter* 20.38 (2008), p. 384210.

[117] J. F. Millithaler, L. Varani, C. Palermo, J. Pousset, W. Knap, J. Mateos, T. González, S. Perez, D. Pardo, and L. Reggiani. "Monte Carlo simulation of plasma oscillations in ultra-thin layers". In: *physica status solidi (c)* 5.1 (2008), pp. 249–252.

[118] J. F. Millithaler, J. Pousset, L. Reggiani, P. Ziade, H. Marinchio, L. Varani, C. Palermo, J. Mateos, T. González, S. Perez, and D. Pardo. "Monte Carlo investigation of terahertz plasma oscillations in gated ultrathin channel of n-InGaAs". In: *Applied Physics Letters* 95.15, 152102 (2009), pages.

[119] S. Hunklinger. *Festkörperphysik*. Oldenbourg, 2009.

[120] R. Kersting, K. Unterrainer, G. Strasser, H. F. Kauffmann, and E. Gornik. "Few-cycle THz emission from cold plasma oscillations". In: *Phys. Rev. Lett.* 79 (16 Oct. 1997), pp. 3038–3041.

[121] E. Starikov, P. Shiktorov, V. Gružinskis, L. Varani, J. C. Vaissiere, J. P. Nougier, and L. Reggiani. "Monte Carlo calculation of noise and small-signal impedance spectra in submicrometer GaAs n+nn+ diodes". In: *Journal of Applied Physics* 79.1 (1996), pp. 242–252.

[122] R. Brunetti and C. Jacoboni. "Analysis of the stationary and transient autocorrelation function in semiconductors". In: *Phys. Rev. B* 29 (10 1984), pp. 5739–5748.

[123] T. Kuhn, L. Reggiani, L. Varani, and V. Mitin. "Monte Carlo method for the simulation of electronic noise in semiconductors". In: *Phys. Rev. B* 42 (9 1990), pp. 5702–5713.

[124] H. Marinchio, J.-F. Millithaler, C. Palermo, L. Varani, L. Reggiani, P. Shiktorov, E. Starikov, and V. Gružinskis. "Plasma resonances in a gated semiconductor slab of arbitrary thickness". In: *Applied Physics Letters* 98.20, 203504 (2011), pages.

[125] R. Akis, J. S. Ayubi-Moak, D. K. Ferry, S. M. Goodnick, N. Faralli, and M. Saraniti. "Full-band cellular Monte Carlo simulations of terahertz high electron mobility transistors". In: *Journal of Physics: Condensed Matter* 20.38 (2008), p. 384201.

[126] H. Marinchio, C. Palermo, A. Mahi, L. Varani, and V. Korotyeyev. "External excitation of hybrid plasma resonances in a gated semiconductor slab: An analytical study". In: *Journal of Applied Physics* 116.1, 013707 (2014), pages.

[127] J. Mateos and T. Gonzalez. "Plasma Enhanced Terahertz Rectification and Noise in InGaAs HEMTs". In: *Terahertz Science and Technology, IEEE Transactions on* 2.5 (Sept. 2012), pp. 562–569.

[128] V. A. Shalygin, L. E. Vorobjev, D. A. Firsov, A. N. Sofronov, G. A. Melentyev, W. V. Lundin, A. E. Nikolaev, A. V. Sakharov, and A. F. Tsatsulnikov. "Blackbody-like emission of terahertz radiation from AlGaN/GaN heterostructure under electron heating in lateral electric field". In: *Journal of Applied Physics* 109.7, 073108 (2011), pages.

List of Publications

Published Papers

- R. J. B. Dietz, R. Wilk, B. Globisch, H. Roehle, D. Stanze, S. Ullrich, S. Schumann, N. Born, M. Koch, B. Sartorius, and M. Schell, "Low Temperature Grown Be-doped InGaAs/InAlAs Photoconductive Antennas Excited at 1030 nm," Journal of Infrared, Millimeter, and Terahertz Waves, vol. 34, no. 3–4, pp. 231–237, 2013.
- M. Wichmann, A. S. Mondol, N. Kocic, S. Lippert, T. Probst, M. Schwerdtfeger, S. Schumann, T. Hochrein, P. Heidemeyer, M. Bastian, G. Bastian, and M. Koch, "Terahertz Plastic Compound Lenses," Applied Optics, 2013.
- S. Schumann, C. Jansen, M. Schwerdtfeger, S. Busch, O. Peters, M. Scheller, and M. Koch, "Spectrum to space transformed fast terahertz imaging," Optics Express, vol. 20, no. 17, p. 19200, 2012.
- S. F. Busch, S. Schumann, C. Jansen, M. Scheller, M. Koch, and B. M. Fischer, "Optically gated tunable terahertz filters," Applied Physics Letters, vol. 100, no. 26, p. 261109, 2012.
- B. Scherger, N. Born, C. Jansen, S. Schumann, M. Koch, and K. Wiesauer, "Compression Molded Terahertz Transmission Blaze-Grating," IEEE Transactions on Terahertz Science and Technology, vol. 2, no. 5, pp. 556–561, 2012.
- M. Wichmann, B. Scherger, S. Schumann, S. Lippert, M. Scheller, S. F. Busch, C. Jansen, and M. Koch, "Terahertz Brewster lenses.," Optics Express, vol. 19, no. 25, pp. 25151–60, 2011.

Conferences & Workshops

- S. Schumann, B. M. Fischer, "Monte Carlo Simulations of THz-Plasma-Waves in FETs," MTT 2015 Convergence of Electronics & Photonics for THz Applications: Dream or Reality?, 2015.
- S. Schumann, B. M. Fischer, "Monte Carlo Simulations THz-Oszillations in Semiconductor Devices," 2nd Workshop of the Institute-Cooperation of the Goethe University and the Center for Physical Sciences Vilnius, 2014.

- S. Schumann, Y. Demarty, D. Simicic, K. J. Kaltenecker, H. Scharf, M. Schneider, B. M. Fischer, "Investigation of pharmaceutical counterfeits and falsifications using terahertz technology," 7th Terahertz Days and GDR-I Meeting, 2013.
- S. Schumann, S. Busch, M. Schwerdtferger, B. Ewers, M. Scheller, C. Jansen, B. M. Fischer, and M. Koch, "Spectrum to Space Computed THz-Tomography (invited)," in 37th International Conference on Infrared, Millimeter, and Terahertz Waves, 2012, pp. 5–6.
- R. J. B. Dietz, R. Wilk, B. Globisch, H. Roehle, D. Stanze, S. Ullrich, S. Schumann, N. Born, N. Voss, M. Stecher, M. Koch, B. Sartorius, and M. Schell, "Pulsed THz emission from low temperature grown Be-doped InGaAs / InAlAs photoconductive switches at 1030 nm excitation (invited)," in 37th International Conference on Infrared, Millimeter, and Terahertz Waves, 2012, pp. 1–3.
- S. F. Busch, S. Schumann, B. Scherger, C. Jansen, M. Scheller, B. M. Fischer, and M. Koch, "Optically controlled Terahertz Filtering , Beam Steering , and Imaging," in 37th International Conference on Infrared, Millimeter, and Terahertz Waves, 2012, vol. 1, no. d, pp. 1–2.
- M. Wichmann, S. Busch, B. Scherger, S. Schumann, S. Lippert, C. Jansen, M. Scheller, and M. Koch, "Astigmatism-free Brewster lenses for terahertz applications," in 37th International Conference on Infrared, Millimeter, and Terahertz Waves, 2012, pp. 2–3.

Patent Applications

- C. Jansen, S. Schumann, M. Scheller and M. Koch, "Bildgebendes THz-Messverfahren und Vorrichtung", European Patent Application EP 11160647.1, 2011.

Danksagung

Diese Dissertation entstand im Rahmen der Zusammenarbeit zwischen der Arbeitsgruppe Experimentelle Halbleiterphysik von Prof. Dr. Martin Koch an der Universität Marburg und dem Deutsch-Französischen Forschungsinstitut in Saint-Louis. Die vorliegende Arbeit wäre ohne die Mithilfe zahlreicher Menschen nicht möglich gewesen. Nachfolgend möchte ich mich bei diesen für ihre fortwährende Unterstützung bedanken.

Zuallererst bin ich Prof. Dr. Hartmut Hillmer zu großem Dank verpflichtet. Ich möchte mich für das entgegengebrachte Vertrauen und das Ermöglichen einer externe Promotion am Institut für Nanostrukturtechnologie und Analytik bedanken.

Prof. Dr. Ubbo Ricklefs danke ich für die Übernahme des Zweitgutachtens. Er hat mich nach meinem Studium auf das Abenteuer Promotion gestoßen und mich damit maßgeblich mitgeprägt. Für seine langjährige Unterstützung möchte ich ihm herzlich danken.

Prof. Dr. Witzigmann danke ich für die Übernahme des Beisitzes in der Prüfungskommission.

Ein Großteil dieser Arbeit entstand an der Philipps-Universität Marburg in der AG von Prof. Dr. Martin Koch. Ich möchte mich für die von ihm erhaltene Freiheit bei der Wahl meines Dissertationssthema bedanken. Weiterhin danke ich ihm für die finanzielle Unterstützung und die Übernahme des Beisitzes in der Prüfungskommission.

Dr. Bernd M. Fischer möchte ich für die langjährige Betreuung meiner Doktorarbeit danken. Insbesondere für seine immerwährende Unterstützung in allen Lebensbereichen danke ich ihm von ganzem Herzen. Ohne ihn wäre diese Arbeit nicht möglich gewesen.

Weiterer Dank gebührt Prof. Dr. Alexander Klös, Franziska Hain und Michael Gräf die mich während meiner ersten Schritte in der Halbleiterbauelementesimulation begleitet haben.

Meine ehemaligen Bürokollegen Ole Peters, Michael Schwerdtfeger, Matthias Stecher, Martin Roch und Korbinian Kaltenecker danke ich für die wundervolle Arbeitsatmosphäre und das nicht immer nur fachliche Dinge Platz im Büro fanden.

Ich möchte weiterhin noch meinen Korrekturlesern ein großes Dankeschön aussprechen: Ole Peters, Sina Lippert, Christoph Möller, David Jahn und Bernd M. Fischer haben mich auf der letzten Etappe begleitet und unterstützt.

Den Sekretariaten in Marburg, Kassel und Saint-Louis danke ich für ihre freundliche und hilfsbereite Art bei administrativen Tätigkeiten. Zu nennen sind hier Maya Strobel, Anne Ehlers, Nina D'Agostino, Claudia Strott, Jasmin Tischer und Isabelle Metzger.

Meinen Eltern und meiner Schwester danke ich für den starken familiären Rückhalt und ihrer vorbehaltlosen Unterstützung.

Abschließend danke ich meiner Freundin Maira Morawietz für ihr Verständnis und liebevolle Unterstützung während dieser nicht immer einfachen Zeit.